FABRICATION AND CHARACTERISATION OF COMPLEX SHAPED Si-Al-O-N CERAMIC COMPONENTS VIA ADDITIVELY MANUFACTURED MOULDS

By

SAI PRIYA SVML MUNAGALA

Thesis Submitted for the Degree of

DOCTOR OF PHILOSOPHY

Department of Mechanical Engineering
School of Engineering
College of Engineering and Physical Sciences
The University of Birmingham
July 2020

UNIVERSITY OF BIRMINGHAM

University of Birmingham Research Archive

e-theses repository

ABSTRACT

This research programme was aimed at manufacturing complex-shaped components, such as gears and turbocharger rotors from SiAlON for use in engineering applications. SiAlONs are alloys of Si_3N_4 ceramics and offer the combination of good mechanical strength and chemical inertness together with the ability to perform at temperatures up to ~1400°C. Although a lot of progress has been made for the fabrication of dense Si_3N_4 (and its alloys) components, research is still being conducted to find fabrication processes that are economical in terms of money and time and that yield high quality components.

The manufacturing route evaluated in the current study was based on the use of complex-shaped additively manufactured polymeric moulds that could then be used during the green forming of the ceramic components, followed by their densification by sintering. The goal was to reduce (ideally eliminate) the need for any machining, leading to faster and lower cost production of complex-shaped ceramic components. The heart of the project was thus the additive manufacturing machine (Solidscape, UK & Ireland). Although intended for use in jewellery making, its ability to 3D-print fine details using high-grade synthetic polymer was exploited. Once each batch of moulds was designed and produced, the process involved mixing the precursor SiAlON powder with additives, pressing the powder into the moulds and subsequent mould removal, debinding and then sintering at 1750°C.

Dense (up to 99% of theoretical density) SiAlON ceramics were obtained. Components were characterised at every step of the process via visual inspection and physical and chemical analysis, including powder flowability, scanning electron microscopy, X-ray micro-computer tomography, X-ray diffraction, etc, for qualitative and quantitative analysis. Parameters affecting the resultant green and sintered body in terms of mechanical stability and surface

finish were investigated. The study also included oxidation behaviour of the ceramic at temperatures from 1250 to 1450°C.

An organic binder was chosen from a select few based on its adhesion property and flowability when mixed with the ceramic powders. The moulds' examination revealed irregular surfaces leading to non uniform surface profiles on the sintered parts. An interfacial surface on the moulds was introduced to improve the surface finish of the green body. Phase analysis coupled with microscopic examination of the sintered ceramic revealed the presence of two phases namely α – SiAlON and β - SiAlON. The Vickers hardness was measured to be HV_{10} = 2545 and the flexural strength was measured to be 87 MPa. Oxidation study revealed the onset of degradation of the ceramic from 1100°C. With an increase in the oxidising time and temperature, an increase in the prominence of cristobalite, grain growth and phase separation was observed.

Limitations of indirect additive manufacturing in the current study are identified. These include the part size limitation, the inefficiency of the printing unit to print uniform moulds without the presence of any debris, the strength of the moulds under stresses, failure in assessing the residual stresses in the sintered compacts and disadvantages of the powder compaction are discussed. The study concludes by suggesting future work to improve the fabrication process including the use of stronger mould material, pressureless green forming technique of consolidation such as gelcasting, development of simulations to predict the behaviour of the ceramic and its residual stresses.

.

ACKNOWLEDGEMENT

I want to thank Prof. Jon Binner profoundly for his supervision, advice and support throughout the research programme. It would have been impossible to complete my work without him, for which I am ever grateful.

I would like to offer my special thanks to the research committee of the School of Engineering at the University of Birmingham who was extremely supportive in my difficult time. I would also like to thank Prof. Kyle Jiang for his support during my time at the university.

I am particularly grateful to all the technicians in the Mechanical department who helped me despite their busy schedule. I offer my deep gratitude to colleagues at the Metallurgy and Materials department for their time, advice and encouragement.

Finally, I am hugely indebted to my brother, Saiprasad without whose motivation and support, this journey wouldn't have existed. I want to personally thank all my family and friends who have always rooted for me.

'Nothing in life is to be feared, it is only to be understood. Now is the time to understand more, so that we may fear less.'

– Marie Curie

Table of Contents

CHAPTER 4 Results and Discussion 102

NOTE

The current thesis will use the following spacial orientation to denote directions and planes throughout:
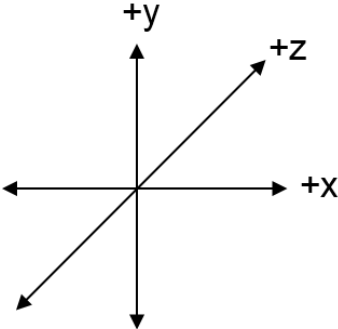
CHAPTER 1

INTRODUCTION

SiAlON is an alloy of silicon nitride, Si_3N_4, that contains additions of alumina, Al_2O_3, and aluminium nitride, AlN, and is an advanced ceramic that is known to have the capability to withstand demanding conditions. Specifically, it is known for its fracture toughness, resistance to oxidation, hardness and resistance to wear, chemical inertness and the ability to be used at temperatures >1000°C[1–5]. It is isostructural with Si_3N_4, existing in two crystallographic forms as for the parent material. Table 1.1 shows a comparison of the properties of SiAlON with Si_3N_4 (hot pressed and reaction bonded) along with other ceramics whilst fig. 1.1 shows some of the components manufactured by International Syalons, UK, out of SiAlON. Its applications include use in the chemical industry, e.g. to contain molten metals or hot oils; aerospace, e.g. as rocket nozzles, milling media, cutting tools, turbocharger rotors, etc.[3,6–10]

Table 1.1: Overview of properties of SiAlON compared with other ceramics[1]

Property	SiAlON, low polytype	Si_3N_4, hot pressed	Si_3N_4, reaction bonded	SiC	Al_2O_3
Mod. rupture / MPa	945	896	241	483	380
Weibull Modulus	11	10 - 15	10 - 15	10	10
Tensile strength, MPa	450	580	145	299	210
Compressive strength / MPa	3500	3500	1000	2000	2750
Young's modulus $*10^5$ / MPa	3.0	3.1	2.0	4.1	3.6
Hardness, $HV_{0.5}$	2000	2200	950	2500	1600
K_{1c} / MPam$^{-0.5}$	7.7	5	1.87	3.0	1.75
Density / gcc^{-1}	3.25	3.20	2.50	3.1	3.98

Fig. 1.1: A range of SiAlON components produced by International Syalons, UK[*]

The SiAlON ceramics were discovered, independently, in Japan and the UK in the 1970s; researchers were attempting to overcome the challenges involved in producing dense Si_3N_4. The latter is conventionally made by either sintering or reaction bonding. Since Si_3N_4 does not sinter readily, and the use of very high temperatures causes degradation into SiO_2 and N_2[3,11], it is usual to add glass forming additives to achieve liquid phase sintering. The latter typically reduce the properties of the final ceramic however[3]. To partially mitigate this, the number of additives can be reduced by using hot pressing or hot isostatic pressing where the combination of high temperature and pressure increases the driving forces for densification[4,12]. Reaction bonding is an alternative approach in which powdered silicon is heated in a nitrogen atmosphere; however, it yields a porous material that requires additional processing steps if dense components are needed[9].

The introduction of Al_2O_3 and AlN to Si_3N_4 forms a eutectic that brings down the melting temperature and hence facilitates sintering at lower temperatures. The glassy phase that forms facilitates liquid phase sintering that enhances the movement of the grains and binds

---

[*] https://www.syalons.com/

them together resulting in better density. The addition of rare earth elements such as Y, Yb, Nd, Sm, Gd, La[13–16] can increase the refractory nature of the glassy phase and hence assist with the high temperature performance of the ceramic. MgO and/or CaO can also be added as sintering aids in trace amounts.

Although there are well-established processes available for making simple-shaped components out of SiAlON, it still challenging to fabricate more complex-shaped components. Common processing methods consist of consolidation of either the dry powder or a slurry to achieve the required green shape followed by sintering as outlined above. Techniques such as injection moulding[17], slip[18,19] or gel casting[20–23] can be used to achieve homogenous green parts. The former is only applicable for the production of large quantities of components since the moulds are very expensive and requires very long debinding times to remove the organic binder[23], whilst slip casting is fundamentally slow and requires the removal of relatively large amounts of moisture during drying[24]. Although gelcasting utilises reusable metallic or polymeric moulds and has the capability to form green bodies with complex geometries, there are again issues with the removal of the binder in that it requires a slow process if cracking of the part is to be avoided[25]. As a result, gel casting has not really started to be used in the industry yet. Currently, therefore, most industrial parts are made by producing simple green blocks and then machining them into complex shapes[26,27], a process known as subtractive manufacturing.

Additive manufacturing (AM) is the opposite process of producing objects by initially creating computer-generated, 3 dimensional (3D) digital images and then using the latter to lay down thin layers of material to build up the part[28,29]. It is an umbrella term for digital manufacturing and includes terms such as 3D printing, rapid prototype manufacturing, direct digital

manufacturing, etc. The approach has been gaining in popularity for over two decades now since it overcomes many of the challenges faced by conventional manufacturing and reduces material waste and is now being translated into the industry for both polymeric and metallic components. Polymers lend themselves readily to AM since they have low melting temperatures and are easy to mould[30], whilst 3D printing of metals and alloys include materials such as aluminium, stainless steel, Inconel, titanium alloys, cobalt chrome, copper, gold and silver[28,31,32]. Some examples of industries now starting to make parts or prototype parts using AM include automotive, aerospace, electronic circuits, arts and crafts including jewellery, and medical applications including custom-made prostheses, drug delivery systems, medical device prototypes and dental fixtures. Applications are also found in the entertainment industry, clothing (particularly shoes), toys, kitchenware, etc[33].

The same cannot yet be said for ceramic components, however. Whilst there is considerable research underway for materials such as Al_2O_3, ZrO_2, Si_3N_4, SiC and SiO_2[34–37], as far as is known no commercial parts are as yet being manufactured using AM techniques. This is largely due to factors such as the critical need to avoid cracks, residual stresses, anisotropic properties and expensive starting materials. Fig. 1.2 shows some ceramic AM products.
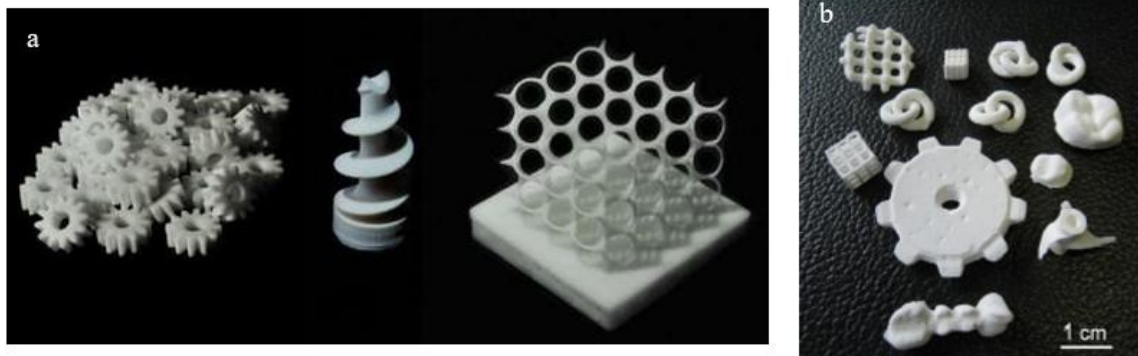
Fig. 1.2: Additively manufactured ceramic components, a. Alumina components from Lithoz, Austria[†]; b. Zirconia components from KU Leuven, Belgium[36]

Therefore, given the challenges of fabricating complex-shaped SiAlON components, this research programme has attempted to assess the potential of a new process based on indirect AM, i.e., the use of AM to make moulds that are then used to make the components[38,39]. This process is inspired by the investment casting technique and hence is also referred to as the "investment approach"[40]. The research programme had the following scope:

a. To investigate if the indirect AM method is a viable process for making complex-shaped components from ceramic powders and to compare the advantages and disadvantages with those of other processes in terms of quality, time and costs.

b. To assess if the process has the ability to cut down the amount of post-processing required for components, e.g. grinding, polishing and machining.

[†] www.lithoz.com/en

c. Whilst the bulk of the work was focused on fabricating SiAlON ceramics, the scope also included assessment of the technique to manufacture components from other ceramic materials.

The main aim was to fabricate complex-shaped green bodies of SiAlON utilising additively manufactured moulds made up of high-grade meltable polymer followed by sintering the samples at a temperature of 1750°C. The bodies were subsequently fully analysed via physical, mechanical and chemical characterisation. Some of the parameters influencing the shaping of the green body were identified and attempts were made to optimise them. The following steps involved in the research:

a. Computer-aided design (CAD) of the example complex geometries, including engineering gears, sprocket gears and turbocharger rotors.

b. AM of the moulds using a high grade, rigid, meltable polymer using a Solidscape 3Z Pro printer.

c. Finding a compatible binder to be used to bind the ceramic powder so that the complex shape could be produced without risking damage to its structural integrity.

d. Designing a heat treatment program for the debinding of the green body, followed by a program for the sintering to obtain a crack-free and a dense component.

e. Characterisation of the components in terms of visual, physical, chemical and mechanical properties to yield qualitative data.

f. Comparison of the qualitative data with the data of the components fabricated via conventional routes.

The resulting work is divided into four further chapters. Chapter 2 presents an extensive literature review on SiAlON, its properties and fabrication, and the information is compared and contrasted with its parent ceramic, Si_3N_4. This chapter also includes the challenges involved in obtaining dense components, which is followed by an outline of the development of additive manufacturing for ceramics. Chapter 3 deals exclusively with the experimental research performed leading to the fabrication of SiAlON complex geometries along with an outline of the characterisation techniques employed for a qualitative and quantitative analysis of the components. Chapter 4 is dedicated to the results and discussion of the experiments conducted and is aimed at developing a deeper understanding of the parameters influencing the entire process. Finally, chapter 5 concludes the work and highlights the advantages and limitations of the process. This chapter also identifies the potential future work that could be undertaken to improve the process further.

CHAPTER 2

LITERATURE SURVEY

The following literature survey consists of four parts, reviewing the literature on:

Part A: Structural ceramics, their fabrication and densification in general

Part B: Structure, properties and fabrication of silicon nitride ceramics

Part C: Structure, properties, fabrication and oxidation behaviour of SiAlON ceramics

Part D: Definition of additive manufacturing and its evolution in materials to date

Many of the fabrication techniques for SiAlON have evolved from those of silicon nitride since SiAlON is a silicon nitride alloy. Therefore, this literature survey mainly consists of existing fabrication techniques and properties of Si_3N_4 and SiAlON.

The literature survey also focuses extensively on additive manufacturing, to understand its importance and potential for manufacturing structural ceramics.

Part A: Structural Ceramics

2.0 Advanced structural ceramics

Ceramics are solid compounds comprising of at least two elements – one of which is almost always a metal whilst the other is a non-metal[41]. These compounds are often formed on the application of heat alone or with pressure at the same time. They are almost insoluble in

water, generally receive their ceramic properties above 800°C, and typically possess at least 30% crystallinity.

The earliest forms of ceramics came into existence with the invention of pottery, where clay was moulded and heat-treated to obtain solid, rigid objects, though they were known to be brittle. In today's world, different types of ceramics have been developed for various applications. Kitchenware, sanitaryware, do it yourself (DIY) crafts, artificial jewellery, automobile, aerospace, bio-implants, sensors, stealth technology, thermal insulators, heat exchangers, gas turbines, power generation, body armours, tooling, etc. are some of the examples where ceramics are involved in the manufacturing process. An extensive list of examples are listed here[42–46]:

Ceramics can be broadly classified into the following:

a. Oxides (Examples: naturally occurring clays, kaolinite, Al_2O_3, MgO, ZrO_2, etc)

b. Nitrides (Examples: Si_3N_4, BN, TiN, AlN, etc.)

c. Carbides (Examples: SiC, B_4C, TiC, etc.)

d. Silicides (Example: $MoSi_2$, etc.)

e. Sulphides (Example: CdS, etc.)

f. Halides (Examples: NaCl, CaF_2, etc.)

g. Borides (Examples: HfB_2, ZrB_2, TiB_2, etc)

Structural ceramics have been reviewed from a microstructural point of view by many researchers. For ceramics, the microstructure is made up of small crystals called grains. In general, the smaller the grain size, the stronger and denser is the ceramic material[47]. The geometric variations encountered in microstructures include size, shape, the preferred orientation of constituent grains, amount of phases, and the distribution of phases among each other[48]. Ceramics exhibit a strong structure-property correlation, making it easy to tailor

the material according to the requirement. They are brittle in nature, have high impact resistance, high chemical inertness, high resistance to oxidation at high temperatures, high young's modulus, high fracture strength, high hardness, etc. All the chemical, mechanical, optical properties of the ceramics can be altered on a microstructural[47–49] level. Comparison studies were also conducted on the strength levels between polycrystalline and single crystalline material, which concluded that the ductility of polycrystalline materials is dependent on their slip systems[49]. Similarly, other research studies have proved strong microstructure- property correlation[21,50–53].

2.1 Fabrication of advanced structural ceramics

Ceramics are fabricated in several ways, all of which include many stages[54]. Different techniques of fabrication help to process different trait ceramics. Fig. 2.1 illustrates the different stages in a general flow of the process.
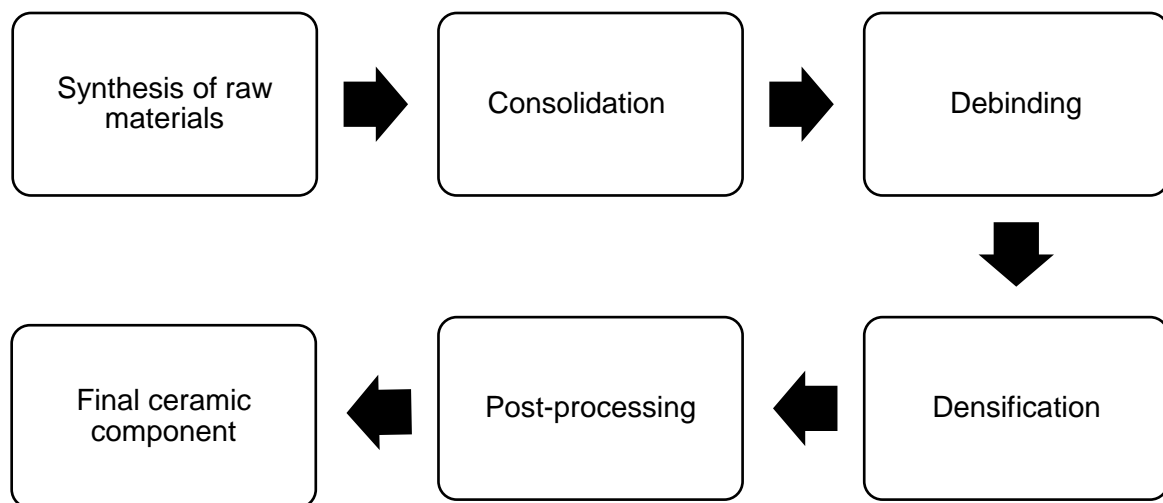
Fig. 2.1: Schematic of stages of fabrication of a ceramic

Stage 1: Synthesis of the raw material for the fabrication process

This stage consists of fabrication of the raw materials for further ceramic processing. It is a critical step in initiating the microstructural-property relationship desired at the end of the fabrication process. The main fabrication process depends on the way how the raw materials were fabricated. To facilitate smooth fabrication of the ceramic, raw materials need to be:

- Pure and devoid of contamination leading to better composition and properties of the end ceramic

- Uniformly shaped and sized particles to have finer and uniform microstructures leading to good properties

More than 95% of the processes are based on the powders as the raw materials. However, different ceramics need different processed powders. Several factors such as charge neutrality, density, particle shape and size affect the final ceramic in terms of its properties[49]. For example, irregularly shaped particles can not be compacted to obtain a ceramic with near net shape and full density, or a pressing grade powder can not be used to slip cast the green body and vice versa. In addition to the technical advantages of various processes, advantageous production costs also influence process selection[55]. Therefore, several methods of powder processing are used to produce various grades of powder to be used for the next stage of processing i.e., consolidation. Although new techniques are always in progress, some of the powder processing techniques are shown in table 2.1[41,54,55].

Table 2.1: Various powder processing techniques

Solid phase reactions	Liquid phase reactions	Gas phase reactions	Other routes
Solid state reactant	Precipitation	Evaporative condensation	Solvent removal
Thermal decomposition of solids	Hydrothermal synthesis	Gas phase reaction with a solid	Sol-gel
Oxidation or reduction of solids			Melt solidification

All the processes lead to powders having a different shape, size and surface area. Powders obtained at the end of this stage usually undergo further processing such as milling and sieving. These steps overcome challenges such as agglomeration and non-uniform sizes. High shear mixing can replace the dry processes for further wet forming routes. More detailed information on the raw material processing and the factors affecting this stage can be found here[20,56–68].

Stage 2: Consolidation/shaping of the ceramic powders

This is a critical step in the ceramic fabrication process as the final dimensional accuracy and finish is controlled here. Slip casting, tape casting, gel casting, injection moulding, extrusion, etc. are some of the examples for consolidation/shaping of the components. Before the shaping process, suitable organic additives are added mainly to help bind the powders, increase lubricity among them, maintain charge neutrality of the whole mixture and many other reasons depending on the process. An overview of the processes is helpful to understand the production of many technical ceramics in different shapes and sizes. Some of the processes are described briefly here.

Slip casting[69] involves pouring of a solvent-based stable ceramic suspension into a microporous mould. The solvent is absorbed, thereby helping the ceramic to consolidate.

Tape casting[63,70,71] is similar to slip casting, but instead of microporous moulds of different shaped geometries, the suspension is poured onto long and flat surfaces. The thickness of the suspension can be controlled here. This method is especially helpful to produce layered ceramics for capacitors and dielectrics.

Gel casting[22,25,72] is another modern method where a single monomer binder (25-30 wt.%) is added to the precursor and a stable suspension is made. The monomer creates a 3D gel network on polymerisation and helps to bind the slurry particles. Complex shapes such as turbine blades can be fabricated via gelcasting. Gelcasting makes the fabrication easier as any shaped moulds can be used.

Extrusion[73] is used when long components such as ingots and bars are required. A ceramic paste is made from the precursor material and the additives. This paste is extruded through a die with a uniform dimensional opening. Furnace tubes and pipes can be fabricated through extrusion.

Injection moulding involves injecting the ceramic paste into the die with suitable pressure. Sometimes a degree of elevated temperature is applied to maintain the flow of the ceramic paste. Small complex shaped components can be fabricated using injection moulding. Some of the successful studies on the achievement of dense ceramic components shaped via injection moulding are listed here[74–78].

Pressing[53,79,80] has been the single most popular technique among the industries because it is fast and cheap to produce simple shaped green bodies. Pressure can be applied either uniaxially or isostatically. Uniaxial pressing is done by placing the ceramic powders within a

die and applying pressure uniaxially (usually practiced in the vertical axis of the component). Isostatic pressure pressing consists of enclosing the ceramic powders in a flexible mould of the desired shape and placing the mould within a liquid/gas container. Pressure is then applied on the part by compressing the liquid/gas, causing pressure in all different directions on the mould. This results in the elimination of pores and the consolidation of the ceramic component. When this process is performed at ambient temperature, it is referred to as Cold Isostatic Pressing (CIP)[81]. CIP results in more homogenous pressing when compared to the uniaxial pressing. When isostatic pressing is performed at high temperatures, it is known as Hot Isostatic Pressing (HIP)[82]. HIP combines the pressing and sintering of materials at the same time or as a presintering process.

Several parameters influence the consolidation step such as the friction between the particles of the ceramic powder, the flowability of the slurry or the powders, friction between the slurry/powders and the mould/die walls, lubricity (among the particles), etc. Lubricants can also be chosen for easy ejection of the green body from the dies/moulds. The components obtained in this consolidation stage are referred to as green bodies. They are usually around 50-60% of the theoretical density[83].

From the overview of the different consolidation processes, it can be concluded that the selection of a shaping method is affected by the following:

- Route of raw materials' processing
- The shape of the final ceramic
- Speed of the process
- Productions costs

Stage 3: Debinding

The green bodies are then subjected to the debinding process. Debinding eliminates all organic content that was added before the consolidation stage. Debinding can be performed in two ways depending on the nature of the organics[84,85]. The components can be subjected to debinding either thermally (usually up to 600°C) or chemically. They are extremely fragile and porous. Besides the consolidation step, debinding is a critical step since the induction of cracks in highly likely.

Stage 4: Densification

The main densification of the particles in the ceramic occurs in this stage, most commonly through a high temperature process called 'sintering'[69,86] in which the individual powder particles bond together. Sintering is usually intended to lead to a density that is greater than 98% of the theoretical value, though there are also times when sintering is used to provide strength to a deliberately porous body, e.g. when making ceramic foams. The sintering process depends on several parameters such as the heating rate, sintering atmosphere, temperature employed, the dwelling time, etc, and optimisation of these parameters can lead to achieving a higher density whilst minimising a competing factor known as grain growth, which consumes the same driving force for densification but without yielding any. Section 2.2 describes the mechanics of sintering in detail and hence nothing further will be described here.

Stage 5: Post-processing

The densified ceramic components then often undergo finishing processes such as machining, coating, infiltration and annealing before they can be used in the final application. Many studies are being conducted on fabrication methods that can cut down the finishing

processes. Cutting down on the finishing processes could mean a reduction in the total number of steps, the total time for production and in the production costs.

2.2 Sintering

Sintering[69] is the process of densifying particles (in the context of powders) by applying heat and pressure, causing them to coalesce, typically via diffusion-based processes, but without causing them to melt.

Sintering is one of the vital processes for densifying hard materials which are otherwise difficult candidates for other densification processes. The main driving force behind sintering is the reduction in surface area which leads to a reduction in surface energy[87,88]. Sintering can sometimes be performed with the help of applying external pressure and high temperature simultaneously, as in HIP. The two types of mass transport mechanisms that happen during sintering are solid-state sintering and liquid phase sintering[86]. Fig. 2.2 illustrates the different types of sintering based on two different techniques - pressured gas sintering and pressureless gas sintering.
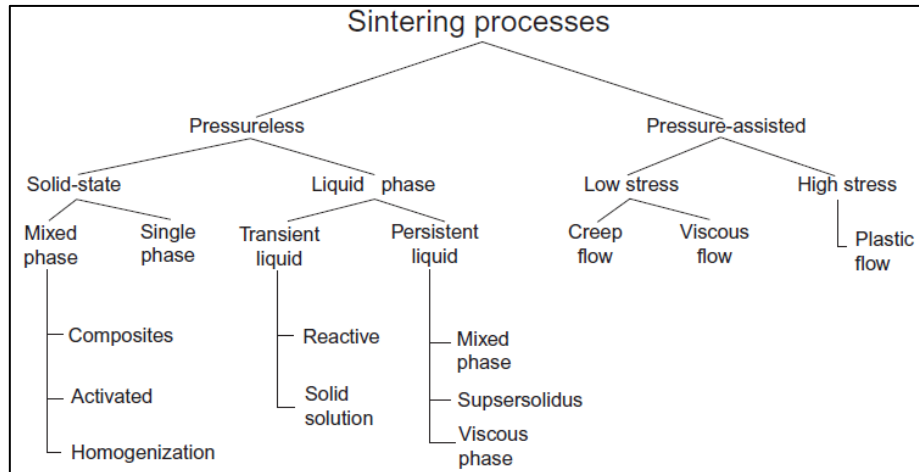
Fig. 2.2: Branching under the sintering processes based on pressureless and pressure-assisted processes[86]

The transport mechanisms differ significantly between solid-state and liquid-state sintering. However, the four main stages of sintering are broadly classified as follows and fig. 2.3 illustrates the sintering process schematically:

a. Contact formation: The contact happens when the particles come together and start touching the surrounding particles.

b. Neck growth: The contact continues to the agglomeration process which results in the formation of several necks among the particles.

c. Pore rounding: Before the agglomeration starts, the pores are mostly angular. After the neck formation, smaller pores start to diminish, and the bigger pores start becoming spherical. Finally, the concavity changes to a neutral or flat structure.

d. Pore closure: This is the final stage of sintering where the smaller and open pores get eliminated, resulting in maximum density.
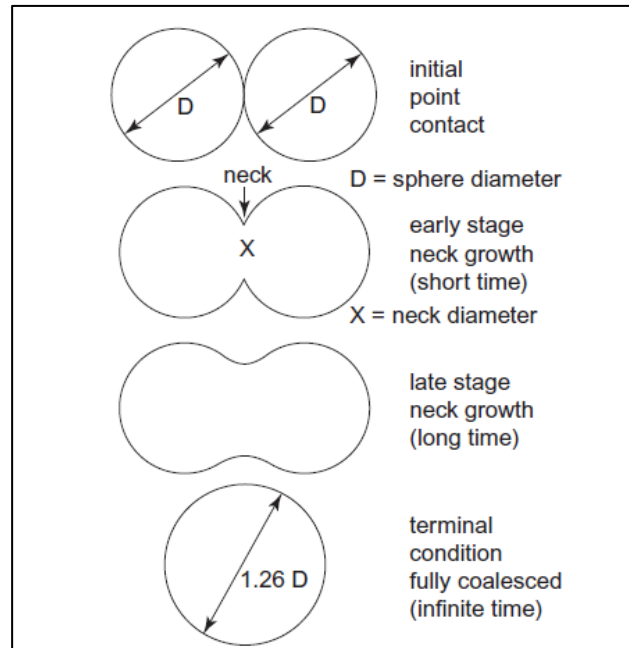
Fig. 2.3: Schematic of two particles being sintered through different stages[89]

Sintering in a material can affect many parameters of the final component. An example is shown in Fig. 2.4, where a correlation between the green density and the sintering shrinkage can be seen. The evolution of the microstructure depends on the neck formation, which in turn changes the grain boundary area. The atomic diffusion occurs in the solid state giving rise to crystallites. Grains evolve when some of the crystallites arrange themselves in an orientation. The number of grains increases based on the dwell time, and this is accelerated as the full density is achieved. Mass exchange happens through diffusion across grain boundaries. This results in pore elimination, accompanied by more grain-boundary and interface area[89].
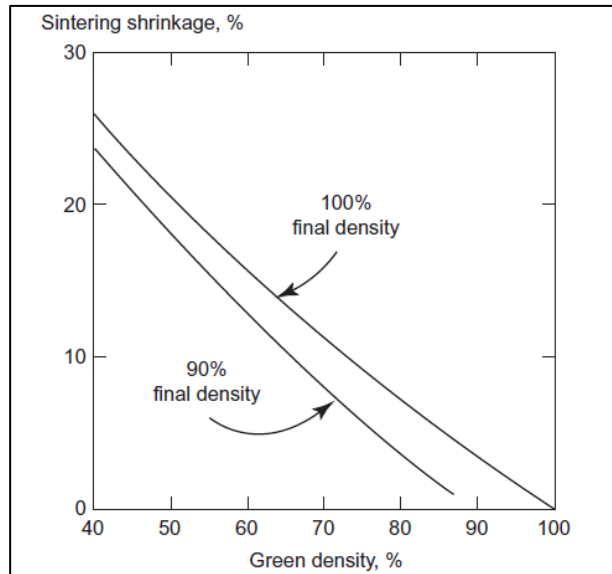
Fig. 2.4: Relation between the green and the sintered density and shrinkage[89]

The green density must be homogenous for efficient sintering to occur[90,91]. The number of pores decreases by the end of the sintering[86]. However, the mean pore size is resistant to change. Swelling and shrinking can be likely outcomes at the macrostructural level[86]. The overall surface area is reduced, leading to the highest possible density.

2.2.1 The thermodynamics and kinetics of sintering

a. Solid-state sintering (SSS)

SSS is one of the best-understood mechanisms in sintering. The main mechanism for densification is diffusion, which can happen via surface, volume, grain boundary, viscous flow, plastic flow or vapour transport[92]. German[93] concluded that surface mechanisms are responsible for mass reposition but do not alter the shrinkage. Instead, they help in reducing the curvature gradient of the pore. Densification happens only due to bulk transport mechanisms since they move mass from the solid on to the pore. Viscous flow happens only in amorphous materials. There is no distinction between the transition of stages that can be

differentiated geometrically or otherwise within the process. Often, different transport systems occur simultaneously, aiding to the densification. Fig 2.5 shows a schematic of the different transport mechanisms that happen during SSS[93]. Prominent researchers such as Kuczynski[94] and Coble[95,96] have designed the models for initial stages of sintering, which have been improved by several researchers such as German, Rene, Arzt and Ashby. They have successfully explained the complete SSS mechanism[97,98]. Moreover, advancements in simulation studies have helped several researchers study and develop numerical simulation, for predicting and developing microstructural changes[99–101].
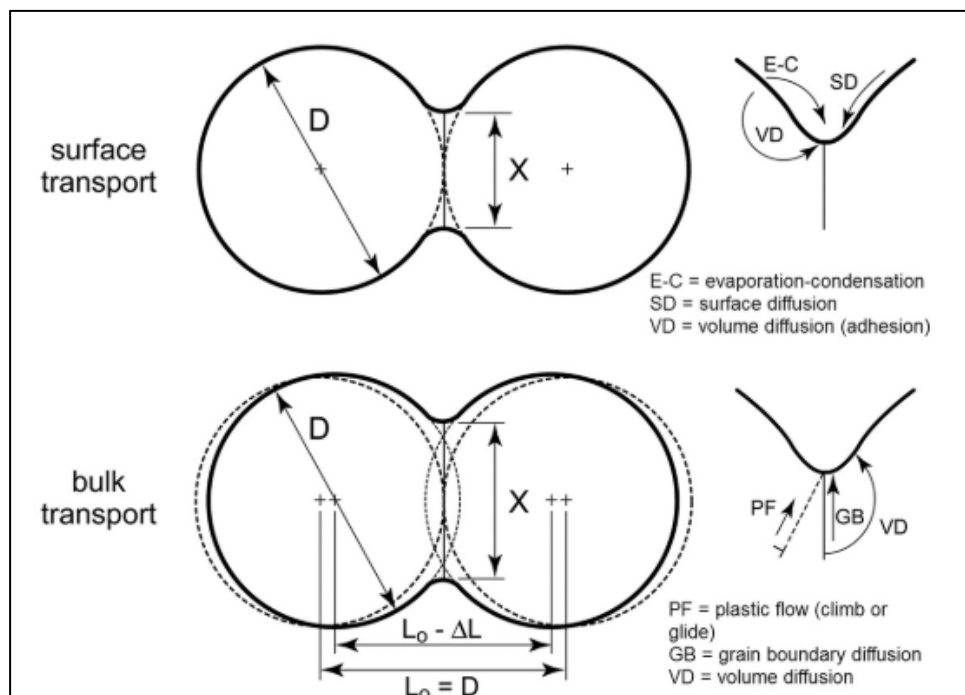
Fig. 2.5: Different mass transport mechanisms happening during the sintering process[89]

Fig. 2.5 illustrates the SSS mechanism driven by reduction in surface energy. This can be accomplished by atom diffusion processes that lead to either densification of the body (by transport matter from inside the grains into the pores) or coarsening of the microstructure (by rearrangement of matter between different parts of the pore surfaces without actually leading to a decrease in the pore volume)[69]. From the point of view of achieving high

densities during sintering, a major problem is that the coarsening process reduces the driving force for densification. This interaction is sometimes expressed by the statement that sintering involves a competition between densification and coarsening[69]. The domination of densifying diffusion processes will favour the production of a dense body. When coarsening processes dominate, the production of a highly porous body will be favoured.

Factors affecting the efficiency of SSS are the starting particle size, homogeneity and density of the green structure, heating rate employed, dwell time and the peak temperature attained.

b. Liquid phase sintering (LPS)

LPS is frequently used in the industry to densify hard materials which cannot be otherwise densified. LPS involves the formation of a liquid phase (from additives) in which the solid is soluble and is responsible for bonding the grains[102]. This is faster than the SSS process since diffusion in liquid occurs at a much faster rate.

The amount and type of additives responsible for the liquid phase formation are decided based on the composition and sintering temperature of the ceramic[102]. Phase diagrams can provide this information, see fig. 2.6. As the diffusion rate increases with the temperature, it governs the quantity of the liquid phase formed. However, the amount of liquid formed is vital, since excess amounts can result in distortion of the final shape of the ceramic. Ideally, an amount <15% of the volume fraction of the liquid is considered for good, structured sintering[102]. On the application of temperature, the solid bonds start dissolving in the liquid phase leading to the formation of a semisolid, viscous mixture of solid grains[102,103]. This mixture then starts flowing and acts as a wetting agent for the solid particles, leading to the rearrangement of the grains. The viscous liquid provides enough lubrication and capillary

attraction to pull the grains together. Next, the liquid starts flowing into the pores, due to the increase in the packing density. The isolated pores start filling. Due to the high surface area, the smaller pores get filled first. This results in macrostructural shrinkage of the component. The degree of the solid solubility in the liquid directly governs the diffusion, resulting in a faster sintering rate. Fig. 2.7 schematically illustrates the timeline of a LPS mechanism.
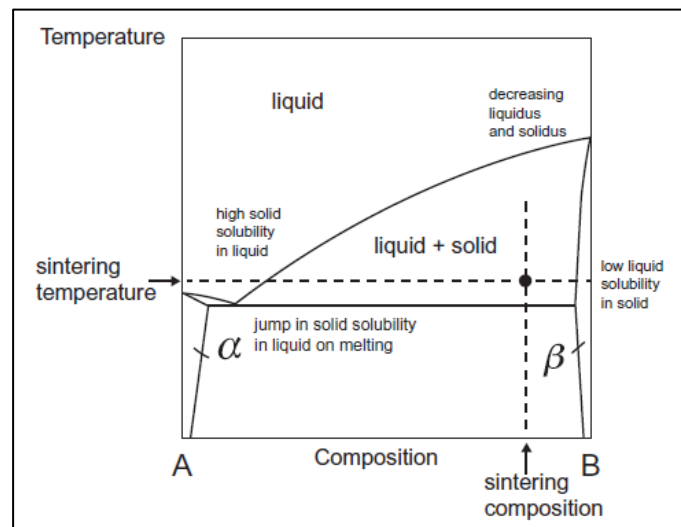
Fig. 2.6: Example of a binary composition phase diagram, helping to decide on the sintering temperature based on the solubility of phase A in phase B[102]
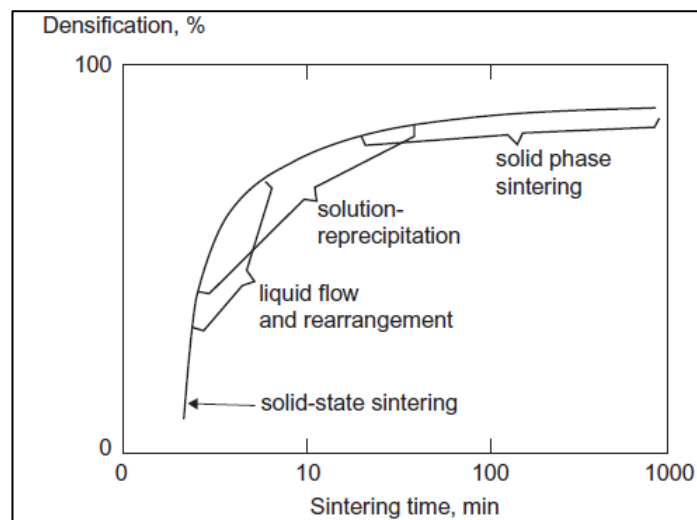
Fig. 2.7: Timeline of the stages in a pressured LPS process[102]

Solution-precipitation[104] is the most notable phenomenon that affects the overall change in the size and reshaping of the grain. At the onset of liquid precipitation, a solid skeleton gives rise to new solid bonds. The liquid fills in the gaps and improves the density. One of the common examples for the LPS among hard materials is the WC-Co system in which a eutectic is formed approx. at 1300°C, resulting in a liquid phase. Another example for LPS is the densification of Si_3N_4[3] with rare earth additions forming a eutectic at ~1340°C. More details on this example will be discussed in part C of this chapter.

The typical microstructure arises from the grains surrounded by the liquid[105]. The composition and the way of processing the ceramic material, are responsible for tailoring the final microstructure and properties of the ceramic. The final mean pore size in the ceramic increases, whilst the total porosity and the number of pores decrease. This results in closed porosity since the pore buoyancy causes the pores to migrate to the surface, thus eliminating the open porosity. In this process, there can be 'swelling' because of the number of big pores present. For highly efficient LPS, the ideal placement of the liquid is at the interface of the grains for better packing[105]. Coated powders are quite helpful to achieve this placement as the coating can form the liquid phase, facilitating easy movement of the same. LPS can be induced by adding additives, wetting agents, increasing diffusion or by hardening the material.

Kingery's model of LPS

Kingery et.al[103,106,107] have studied the LPS process extensively both under pressured and pressureless conditions. Kingery proposed a model for the LPS based on the timeline shown in fig. 2.7 which is as follows[12]

Stage 1 corresponds to the particle rearrangement. The rate of the rearrangement and shrinkage of the sample depends on the amount, viscosity and composition of the liquid phase formed.

Stage 2 is the occurrence of solution precipitation, where shrinkage is linearly proportional to $t^{1/n}$; t is the time and n is 3 or 5 depending on the sintering aid controlling the kinetics by solution-precipitation or by diffusion respectively.

Stage 3 is the elimination of the closed porosity and grain coarsening. A density >95% of the theoretical is achieved.

Some of the main conclusions on how the level of pressure makes a difference are described in table 2.2.

Table 2.2: Main differences between pressured and pressureless LPS in ceramics[107]

Stage	Pressured sintering	Pressureless sintering
Stage 1	Increased rate of particle rearrangement	A rearrangement of solid particles
Stage 2	Increased rate of the liquid reaching the particles	Solution precipitation; dissolution of the solid
Stage 3	Increased rate of the plastic flow among the particles	A coalescence of the particles

For naturally temperature resistant materials, external pressure-assisted sintering is done[108]. External pressure helps to increase the driving force of reduction in surface area. External pressure could be supplied via processes such as HIP and CIP. Si_3N_4, SiAlON and

related ceramics have been fabricated under both pressured[67] and pressureless[109] conditions. More details will be discussed in parts B and C of this chapter. Along with the LPS, SSS also occurs after the liquid starts to densify in few materials[110].

Part B: Silicon Nitride

2.3 Silicon nitride (Si_3N_4) ceramics

Silicon nitride ceramics have been one of the highly researched ceramics in the past few decades due to their excellent high-temperature properties[111]. They have been in demand from the 1970s when structurally strong and heat resistant ceramics were required for gas turbines. The applications have been extended into other fields such as tooling, heat exchangers, engines, power generation, etc[3,43]. For these applications, the ceramic must have a high stress per unit strain, i.e., high elasticity modulus. High modulus implies high bond strength to sustain higher temperatures and stresses associated with it without undergoing any chemical changes[3]. Ceramics such as Al_2O_3, AlN, BeO have low thermal shock resistance, high hydrolysis affinity and toxicity respectively. Thus, covalently bonded ceramics such as SiC and Si_3N_4 are most qualified as engineering ceramics in harsh conditions[12]. Table 2.4 illustrates the elastic modulus and the decomposition temperatures for few of the ceramics.

Table 2.3: Specific modulus of some materials[9]

Material	Elastic modulus / specific gravity / MPa	Decomposition temperature / °C
AlN	0.10	2450
Al_2O_3	0.11	2050
BeO	0.12	2530
SiC	0.17	2600
Si_3N_4	0.12	1900

The ceramic Si_3N_4 is covalently bonded and, hence, its self-diffusivity is extremely low. This makes its densification difficult just by firing. Lower densification implies high porosity which hampers the structural quality and properties of the ceramic. Fabrication processes for Si_3N_4 in the early 1970s were mainly either hot pressing or reaction bonding[3,7,9]. However, high density wasn't achieved via reaction bonding as it left around 25% of porosity. Hot pressing did achieve high density but was limited to simple shaped components[3]. Therefore, the desire to develop superior fabrication processes led to the addition of additives to Si_3N_4. This addition induced a liquid phase at a temperature lower than the decomposition temperature of Si_3N_4 and densification is then carried out with the help of the liquid bonding the solid particles together via LPS.

2.3.1 Structure of Si_3N_4

Silicon nitride is known to exist mainly in two forms α and β, both hexagonal[6,112], with the c parameter in α approximately twice as that in β. This structure is exactly same in SiAlON too. The covalent bonding leads to a tetrahedral structure with a Si in the centre bonded to three nitrogens, which are in turn shared by three other tetrahedra, as shown in fig. 2.8. These structures can be regarded as layers of Si and N atoms in the sequence of ABAB… or ABCDABCD… for the β and α phases respectively in fig 2.9.
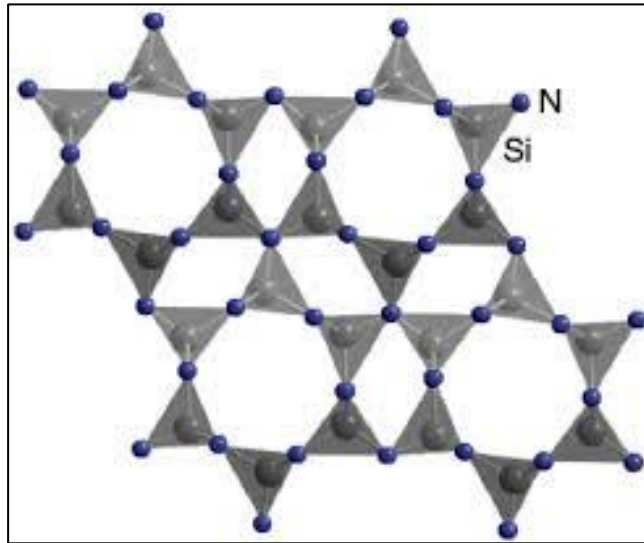
Fig. 2.8: Structure of silicon nitride[‡]

By forming a sheet of six eight-membered Si-N rings, the hexagonal β structure is obtained which belongs to the space group $P6_3/m^{3,9}$. The SiN_4 tetrahedra form in such a way that tunnels run along parallel to the c axis. This structure is relatively strain-free compared to α-Si_3N_4, which has significant lattice distortion ($P3_1c$ space group). This strain occurs due to the glide plane of layer AB rotating 180° along the c axis, thus creating inter interstitial holes instead of long tunnels. The α phase exists at low temperatures and is thermodynamically unstable at temperatures >1400°C and gets transformed to the β phase thereafter[9]. This transformation of α→β is accompanied by oxygen loss and the kinetics reveal that this transformation is largely impurity-controlled in the form of a liquid phase[13]. This phase is responsible for the eventual solution-precipitation that happens for the densification. The liquid phase can be introduced in the form of silicon, silicides or silicates made from the presence of oxygen and nitrogen in the process. More on the effects of alloying addition is discussed in section 2.3.2.

[‡] www.chemtube3d.com
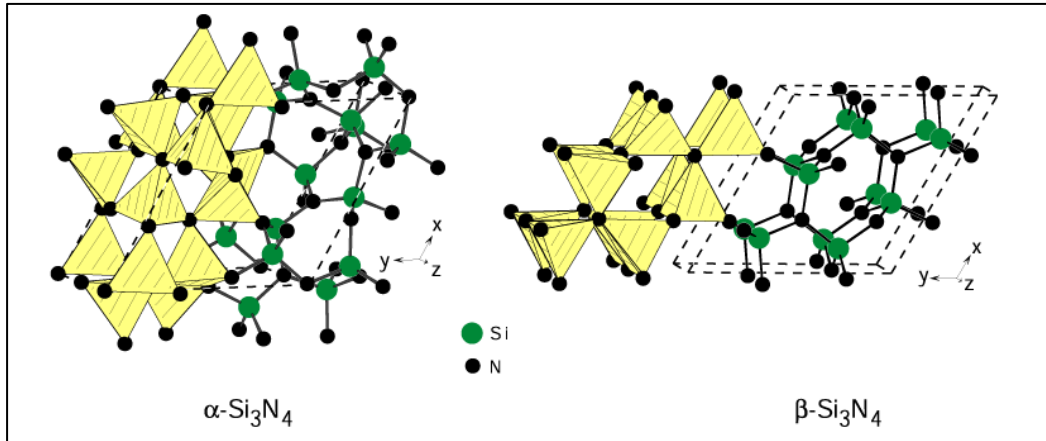
**Fig. 2.9:** Crystal structures of α-Si_3N_4 and β-Si_3N_4[113]

Jennings and Richman[114] have conducted extensive studies on the kinetics and parameters affecting the $\alpha \rightarrow \beta$ transformation via reaction bonding. The factors such as the heating rate, gas flow rate, time and temperature were observed to be responsible for the different morphologies of the α phase before it is transformed into the elongated, needle like β phase. Table 2.4 highlights some of the observations made on the microstructures of the phases affected by these parameters.

Table 2.4: Effects of different parameters on the morphology of the α and β phases[114]

Microconstituent	Time / h	Temperature / °C	Heating rate / °Ch⁻¹	Gas flow rate	Comments
α needle	<24	<1400	300	--	Observed in majority of samples Less pure
β blades	>24	>1450	--	--	Only observed when conditions are satisfied
α (fine) matte	--	<1450	Slow	No gas	Use pure and fine powder
β (coarse) matte	>5	>1450	Rapid	fast	
β spikes	--	>1450	Rapid	fast	Use less pure and coarser powder
Large pores	>24	>1450	Rapid	--	
Large unreacted grains	>24	<1450	300	--	
-- indicates that evidence collected thus far does not indicate variable is important					

From the same study, fig. 2.10 and fig. 2.11 further represent the ratios of α/β formed as a function of different heating rates and highest temperatures attained respectively.
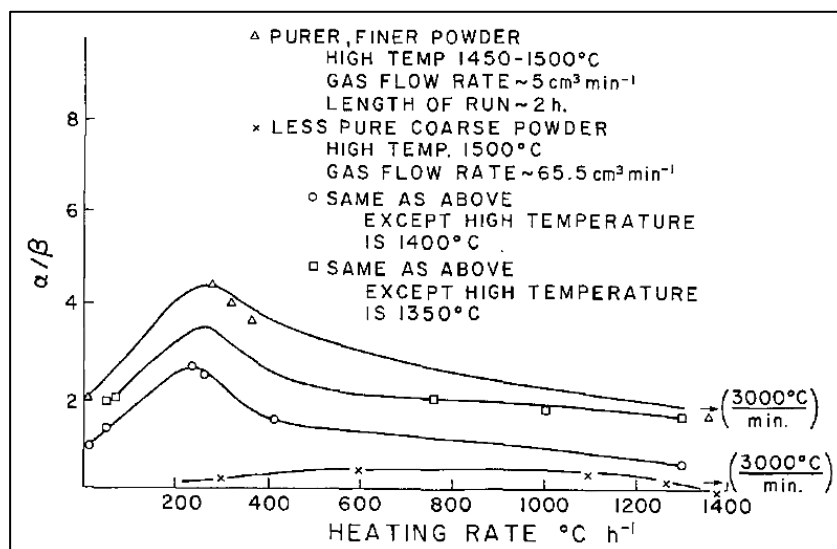
Fig. 2.10: Graph of the ratio of α/β vs. heating rate[114]
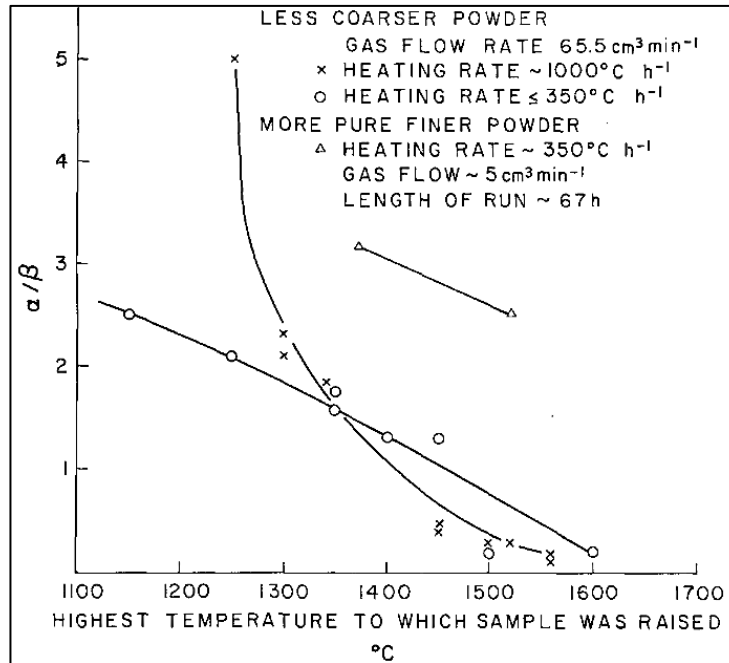
**Fig. 2.11:** Graph of the ratio of α/β vs highest temperature[114]

2.3.2 Addition of alloying elements to Si_3N_4

Additions of rare earths have yielded an improvement to many aspects of Si_3N_4. Initially, these modified compositions were considered to increase the self-diffusivity of Si_3N_4[3,115]. Later, the practice of modifying the compositions continued due to the enhanced properties achieved by the ceramic. Among the additives added, one breakthrough was the discovery of SiAlONs, which will be discussed exclusively under part C of this chapter. The addition of the sintering aids leads to the following equilibrium at high temperatures with a liquid glassy phase:

$$\alpha - Si_3N_4 \ + \ SiO_2 \ + \ M_xO_y \rightarrow \beta - Si_3N_4 \ + \ M - Si - O - N \ (glassy) \qquad \text{Eq. 2.1}$$
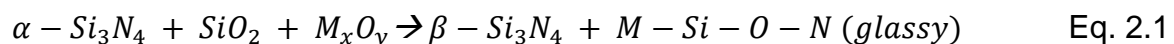
where M can be a mixed oxide additives or rare earth oxides[3].

The presence of the M-Si-O-N glassy phase is proven to improve the overall densification, mechanical and chemical properties of Si_3N_4[9,12,116]. Additionally, the commercially available

powder of Si_3N_4 is always surrounded by a layer of silica, which reacts with the impurities or the oxide additives to form the liquid glassy phase according to the equation[3] 2.1. Table 2.5 gives an overview of the additives that can be used as sintering aids and their effects on the end density, porosity and the flexural strength of Si_3N_4.

Table 2.5: The effects of additives on sintering of silicon nitride[117]

| Additive	Wt. / %	Pressing temp. / °C	Density / gcc^{-1}	Porosity / %	Flexural strength at 20°C / MPa
Cr_2N	5.0	1800	2.06	39.0	--
TiN	4.0	1850	2.10	33.7	--
$MoSi_2$	10	1800	2.45	25.7	135.8
$MoSi_2$ + Fe_2O_3	1.4				
$MoSi_2$ + Al_2O_3	1.9				
Cr_2N	15	1800	2.41	24.4	--
BN	7.5	1850	2.40	24.0	--
B	3		2.50	22.0	--
Cr_2O_3	4.4		2.40	22.0	--
ZnO	3.7		2.5	21.0	--
Fe_2O_3	4.3		2.50	19.7	203.4
CaO	4.2		2.60	17.3	--
Fe_2O_3	8.6		2.70	14.4	331.0
ZrO_2	4.5		2.70	14.1	--
Al_2O_3	5.7		2.90	6.7	314.0
Fe_2O_3	4.3		3.00	5.1	221.3
Fe_2O_3 + Al_2O_3	5.7				
BeO	8.2		3.15	0.97	--
Mg_3N_2	3.3		3.21	0.36	724.0
Mg_3N_2	5		3.18	0.2	662.0
Al_2O_3	11.4		3.10	0.1	260.0
MgO	5		3.17	0.05	572.3

2.3.3 The nature of the α-β transformation

Both the phases of Si_3N_4 are hexagonal in nature[3]. The α phase is a low-temperature (<1400°C) stable form and the β phase is a high temperature (>1600°C) stable form. The α

phase being unstable exhibits a tendency to transform into β (resembling rod-like structures)[9]. The basic transformation of α→β occurs through the reconstruction of the lattice[3]. The rearrangement of the grains is quite sluggish, and the presence of a liquid phase accelerates the transformation. The liquid is induced because of the alloying additions (section 2.3.2) at a temperature greater than the transition point. Hence, this leads to solution-precipitation[9]. The microstructure of the β phase reveals elongated needle-like structures. This structure improves the strength of the material by an interlocking mechanism[3]. Fig. 2.12 shows the schematic of the whole transformation process, whilst fig. 2.13 is the type of microstructure obtained after the transformation process.

There have been many qualitative arguments on this transformation and the stabilities of the two phases. The temperature for the reverse transformation to happen is too low and the reconstruction energy too high[12,118]. Other researchers have claimed partial transformation of β→α based on microstructures and crystalline phases but there is no hard evidence to back up this reverse transformation[3].
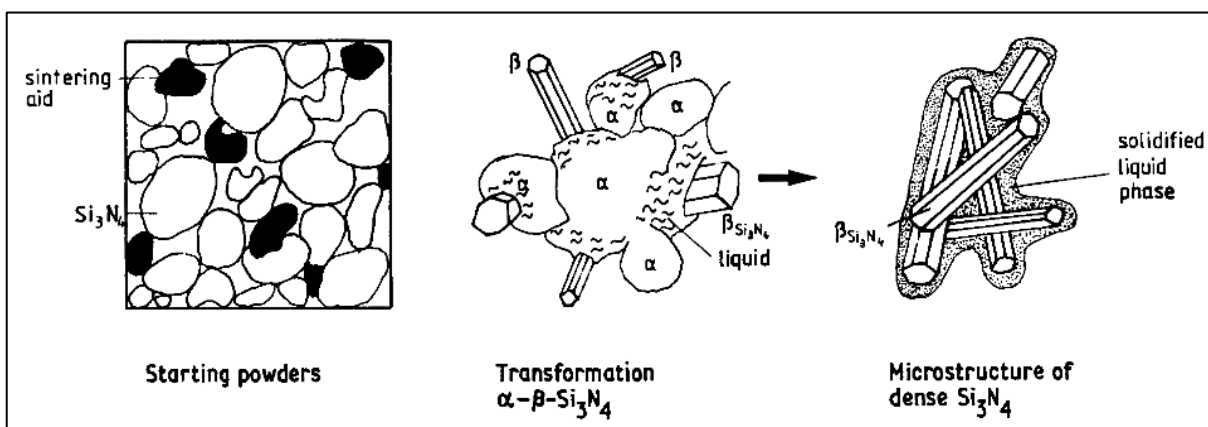
Fig. 2.12: Solution precipitation mechanism for the LPS of Si_3N_4[119]
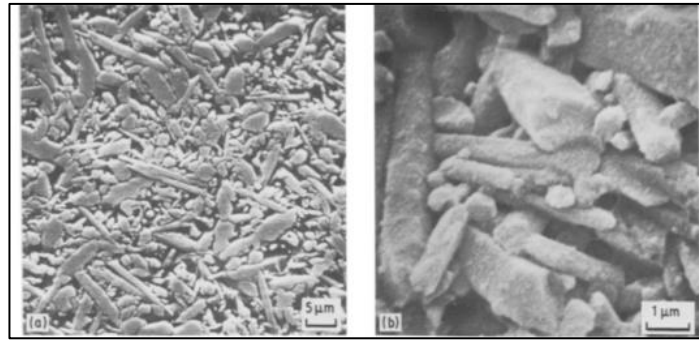
Fig. 2.13: Microstructure of Si_3N_4 characterised by the elongated β phase. a. surface; b. fractured surface[119]

2.3.4 The densification of Si_3N_4

a. Gas pressured sintering (GPS) of Si_3N_4

As discussed in section 2.3.2, rare earth oxides and other additives were initially introduced to increase the self-diffusivity of silicon nitride. Although the self diffusivity was increased, the presence of the additives increased the sintering temperature > 1850°C. This eventually led to the decomposition of Si_3N_4 into SiO_2 and N_2. Therefore, to suppress the decomposition, promote the densification and use lower amounts of sintering aids, gas pressured sintering was put into practice[120]. N_2 gas pressure as high as up to 10 MPa is applied in this process.

HIP is a process where the densification occurs with a simultaneous application of surrounding pressure (via gas) and temperature isostatically on the green body[121]. This is considered as one of the rapid heating approaches for densification among other processes such as microwave press heating, spark plasma sintering, induction hot pressing, etc[121,122]. HIP can be applied to any ceramic for densification.

On the other hand, GPS is applied to nitrogen ceramics which are thermodynamically unstable at higher temperatures[123]. Overpressures of nitrogen suppress the dissociation of

the nitrides[123]. There are several other ways in which hyperbaric ambient gas can affect the densification process during the final stage of sintering[124]. In the last stage, the pore network is broken up into individual, closed pores located on or inside grains and whose rate of shrinkage is controlled by the diffusional flow of the slower-diffusing species, usually presumed to be the entrapped gas at pore closure[125].

The processes HIP and GPS resemble each other in many aspects but there are few key differences as described in table 2.6[69,82,108,120]. These differences are specially employed for the fabrication of Si_3N_4 extensively.

Table 2.6: Key differences between a HIP and GPS process

HIP	GPS
Any gas can be used	Only N_2 can be used
Pressure controls the densification	The pressure is responsible for the suppression of decomposition
No sinter aids are required	Low amounts of sinter aids can be employed
Pre consolidation is required	No pre-treatment is required
Fine microstructure leading to high strength can be attained	The residual pore network is different when compared with that formed via pressureless sintering. This often leads to better oxidation resistance and higher thermal shock in the ceramic.

Mitomo[120] (1976) conducted one of the earliest pressured sintering studies and compared them with pressureless sintering conducted by Terwilliger and Lange[126]. Employing 5 wt.% of MgO as a sintering aid in both the cases, Mitomo concluded that gas pressure sintering achieved more than 95% of the theoretical density which was greater than theoretical density achieved in pressureless sintering (> 80%). GPS also helped to maintain the thermal stability of the ceramic beyond 1600°C. On the other hand, rapid mass loss was observed starting at 1500°C, which marked the maximum density mark. The decrease in the density

and increase in the mass loss was mainly due to shrinkage and thermal decomposition. This behaviour is illustrated in the plots of fig. 2.14.
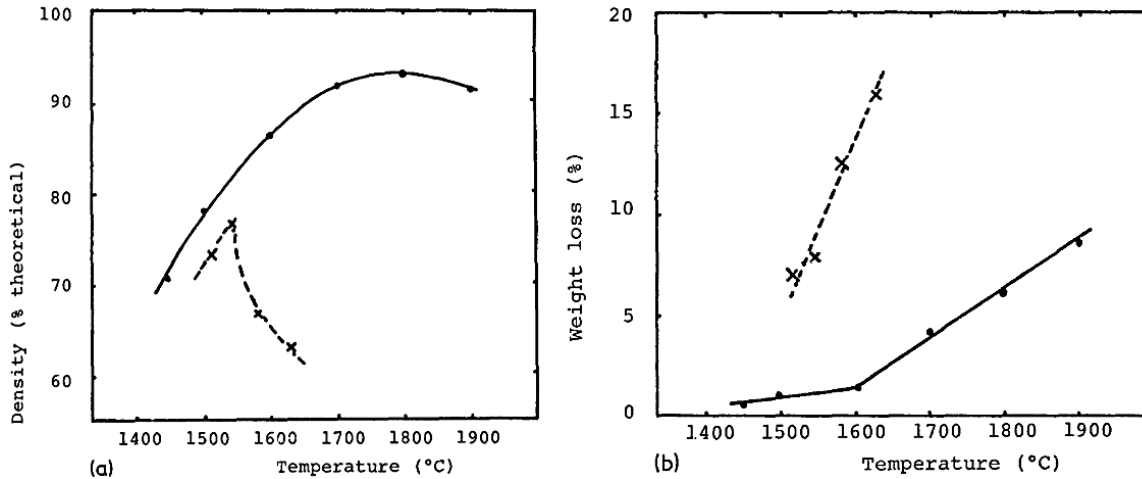
Fig. 2.14: Comparison between a GPS and pressureless sintering process; a. Density vs. temperature; b. Weight loss vs temperature (the dotted lines represent pressureless sintering and the solid line represents GPS)[120]

Mitomo concluded that the densification occurred in two stages satisfying Kingery's model of LPS, i.e., particle rearrangement (up to 1500°C) followed by solution-precipitation at a higher temperature creating a liquid phase of SiO_2-MgO. The shrinkage volume fraction ($\frac{\Delta L}{L_o}$) within the particle rearrangement stage was calculated from the following equation:

$$\frac{\Delta L}{L_o} = k_1 \quad t^{1+y} \qquad\qquad \text{Eq. 2.2}$$

where t is the time, k_1 is a constant and y is some small fraction.

The shrinkage volume fraction changes to the following in the stage of solution-precipitation given by:

$$\frac{\Delta L}{L_o} = k_3 \quad t^{1/3} \qquad\qquad \text{Eq. 2.3}$$

Studies were also conducted on the effectiveness of different sintering aids, employing the same proportion as 5 wt.%. Among these, it was found that alumina, yttria or the combination

of both were the most effective compared to La_2O_3, Ga_2O_3-Al_2O_3 or AlN-Al_2O_3 in the aspects of the density and weight loss at high temperatures. This is due to the fact of a high strength glassy phase formed in the Al_2O_3-Y_2O_3 system. This phase enhances the strength properties and is insensitive to the impurities at high temperatures. Table 2.7 shows some of the densities obtained in GPS of silicon nitride when different sintering aids were used.

Table 2.7: Effectiveness of different sintering aids on the density and the weight losses at high temperatures[120]

Additives	Density / gcc^{-1}	Density / %	Weight loss / %
Y_2O_3	2.58	80.9	4.9
Al_2O_3	2.62	82.1	5.2
Y_2O_3 - Al_2O_3	2.66	83.4	1.3
La_2O_3	2.4	75.2	1.5
Ga_2O_3 - Al_2O_3	2.35	73.7	3.5
AlN - Al_2O_3	2.35	73.7	2.0

Following Mitomo's work, Greskovich[124] (1981) developed a 2 step sintering process using GPS to achieve even higher density and higher sintering rates with 7 wt.% of $BeSiN_2$ and SiO_2 as sintering aids. This development led to more than 99% of the theoretical density in the end component. This process comprised holding the first sintering process in the N_2 atmosphere at a lower pressure (approx. 2 MPa) followed by an increase in the pressure up to 10 MPa in the second step. The motivation behind this work arose from the fact that in the case of a regular sintering process, the glassy phase formed often resides along the grain boundaries of β-Si_3N_4. This damages the thermo-mechanical properties of the ceramic through easy grain boundary sliding and intergranular creep cavitation[50,126]. A variation in the pressure levels was considered to alter the pore distribution and pore closure of the final ceramic affecting the relative density[4]. Although a reduction in the amount of the sintering aids controls the amount of the liquid phase formed, the 2-step sintering process is effective in overcoming the low density.
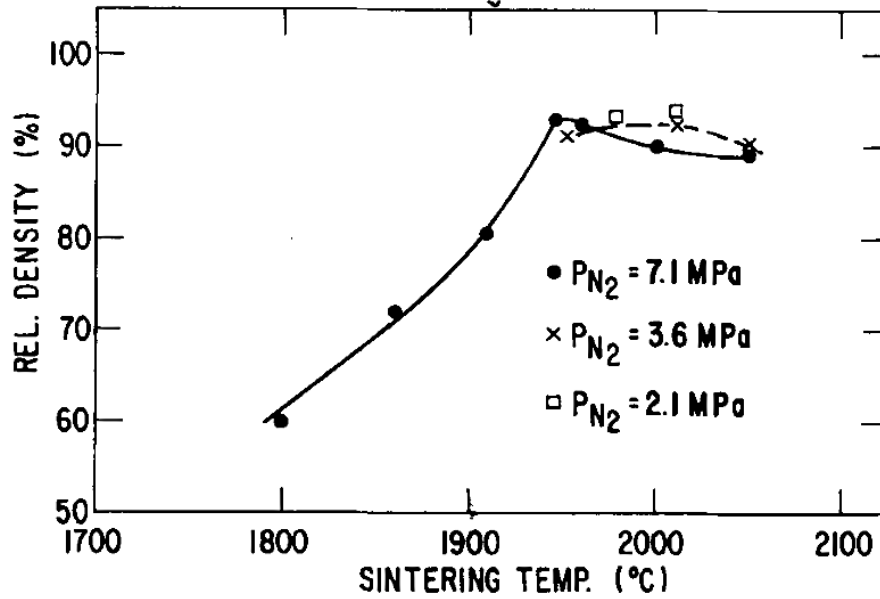
Fig. 2.15: Relative density vs. sintering temperature for single-step sintering process of Si_3N_4 with 7 wt.% of sintering aids[124]
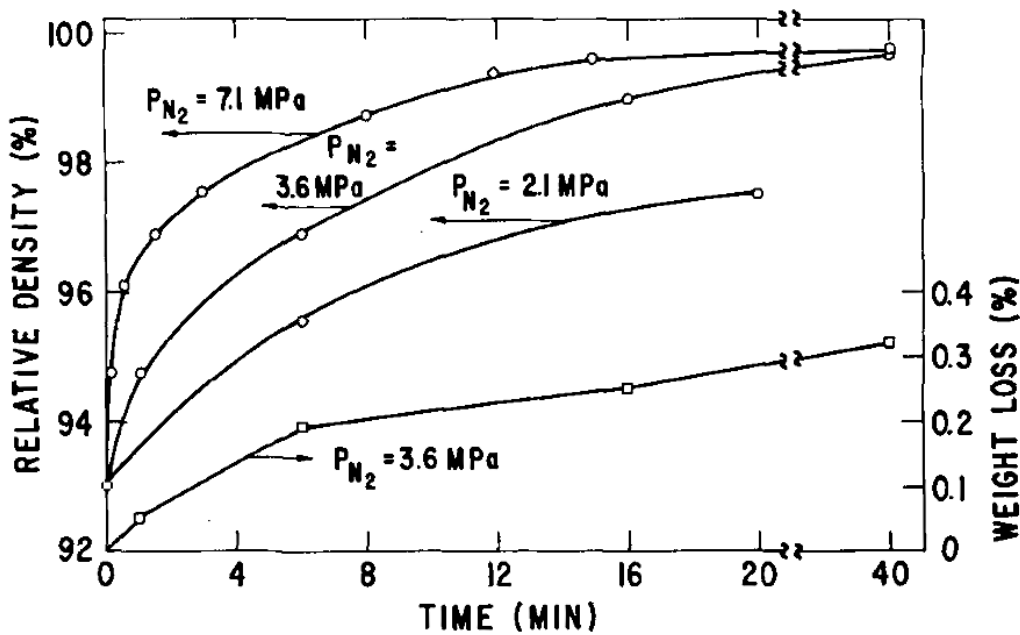
Fig. 2.16: Kinetics of densification and weight loss for of Si_3N_4 sintered in 2 steps with 7 wt.% of sintering aids. The pressures indicated are the ones employed in the 2nd step of sintering[124]

From fig. 2.15, the measurements of the density of the ceramic fabricated under different N_2 pressures reveal a loss of density beyond 1950°C. This was observed in three cases when pressures of 2.1, 3.6 and 7.1 MPa were used. The loss in density was due to shrinkage and thermal decomposition. Hence, a sintering program was devised where a pressure of 2.1 MPa was used for the pore closure (attaining approx. 92% density) followed by an increase in the pressure up to 7.1 MPa for further rapid densification. The final density was measured to be >99%. Fig. 2.16 illustrates the kinetics of densification along with weight loss for the ceramics fabricated under these pressures. This figure represents the pressure in the densification stage. Following this investigation, many other researchers adopted the 2-step sintering process to fabricate thick-walled components and achieved >99% dense ceramics. Some of the studies are reported here[43,44,127].

Pressureless sintering of Si₃N₄

With the introduction of a liquid phase, Si_3N_4 can be densified in pressureless conditions. The glassy liquid phase is mainly responsible for the pore closure and formation of the skeletal structure. Kingery's LPS model illustrates the mechanism clearly in section 2.2.

Pressureless sintering, which involves pressures of <2 MPa, is employed in cases where the starting materials have the α phase in high amounts (≥95%)[115]. This phase being thermodynamically unstable beyond 1400°C tends to transform into the β phase completely[4,115]. This high amount of α phase enhances the amount of the liquid solution leading to a high extent of densification.

On the other hand, when the starting material with a higher content of the β phase is densified, the finer particles of this phase start dissolving due to the high chemical potential. Solution precipitation then occurs on the original β phase particles due to the lack of nuclei

and to achieve low surface energy. This results in the formation of large, spherical and equiaxed β grains as opposed to the elongated, rod-like structures. Due to the inability of the equiaxed particles to interlock among themselves, mechanical properties of the ceramic are severely damaged. Intergranular crack propagation gets easier with equiaxed particles compared to the elongated and interlocked grain structure.

Part C: SiAlON

2.4 SiAlON and its structure

Among the additives identified to form the liquid phase to effectively sinter Si_3N_4, the addition of Al_2O_3, AlN and Y_2O_3 as the sintering aids led to the discovery of SiAlONs[9]. This set of additives can achieve full density without the use of gas pressured sintering. There are other additives besides this combination that form a liquid glassy phase, but the phase is found to reside along the grain boundary[9]. This cannot be accommodated in the crystal structure of Si_3N_4. Additionally, the phase is responsible for downgrading the mechanical properties above the glass transition temperature. However, the glassy silicate phase formed from the Al_2O_3 and AlN system strengthens the mechanical properties and is considered as good as β-Si_3N_4[13]. This phase is given by the empirical formula of $Si_{2-x}Al_xO_{1+x}N_{2-x}$ where $0 < x < 0.2$. The solid solution formed from the β-Si_3N_4 with the simultaneous substitution of Si-N with Al-O is given by **$Si_{6-z}Al_zO_zN_{8-z}$ where $0 < z < 4.2$**[4]. This is the **β SiAlON** phase.

The second form of SiAlON is isostructural with the α phase of Si_3N_4 which exists due to the stacking fault in the β form leading to blocked long channels at regular intervals giving rise to interstitial holes. These holes are then substituted in a limited way by replacing Si-N by

Al-O (quite like the formation of α Si$_3$N$_4$). The valency requirements are satisfied by adding a cation of Y/Mg/Nd/Ca giving rise to the α SiAlON phase. Its empirical formula is given by **Me$_x$Si$_{12-(m+n)}$Al$_{m+n}$O$_n$N$_{16-n}$ where x < 2 and Me is the modifying cation**[3]. The fig. 2.17 and 2.18 illustrate the structural and the phase system (at 1700 – 1730°C) of the SiAlON respectively.
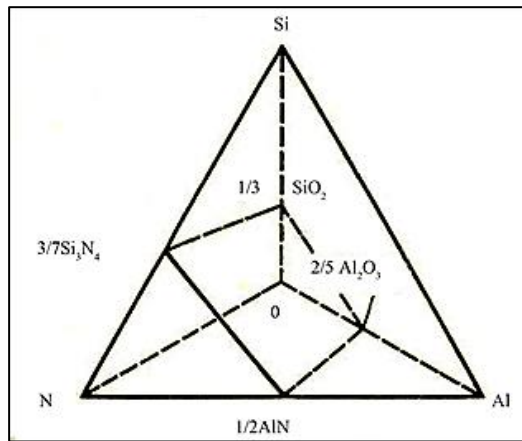
**Fig. 2.17:** Representation of the tetrahedral Si-Al-O-N system[128]
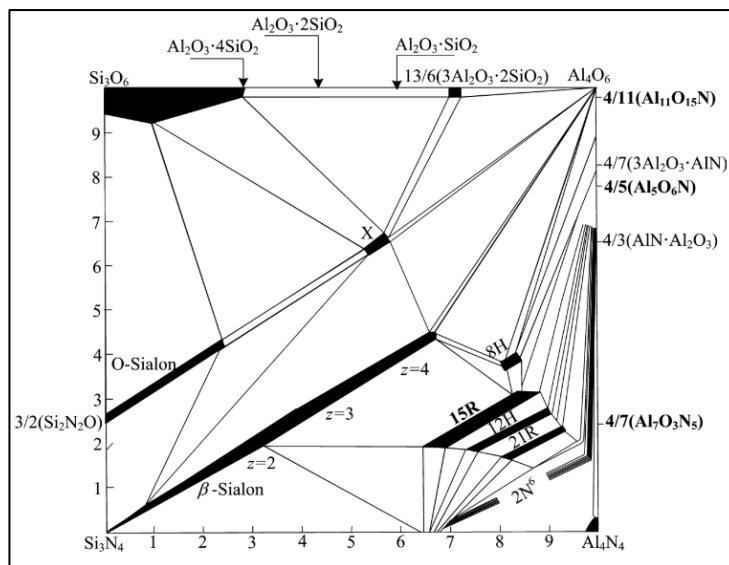
Fig. 2.18: The subsystem of SiO$_2$-Si$_3$N$_4$-AlN- Al$_2$O$_3$ at temperatures between 1700 – 1730°C[9]

2.4.1 The polytypoids in the subsystem of SiO₂-Si₃N₄-AlN- Al₂O₃

There are six polytype phases in the SiAlON system namely 8H, 2H, 12H, 21R and 27R (five of them can be seen in fig. 2.18) which are named by the Ramsdell[9,129,130] symbols. These are structurally similar in most of the metal-SiAlON structures and are distinctive according to their $M{:}X$ (metal:non-metal) atom ratio. In the SiAlON subsystems, the atom ratio is given by $mM{:}(m+1)X$ where m can be 4, 5, 6, 7, 9 and 11. Any metal cation satisfying the charge balance can be incorporated into the SiAlON structure. All the polytypes are constant in the chemical composition and differ only in the way the layers are stacked within the structure. The polytypoids can be identified via X-ray diffraction and contain wurzite (hexagonal) sequence of tetrahedral broken up by single layers of octahedral inserted every m^{th} layer.

Addition of any other metal oxide or metal nitride gives rise to the five-elemental system, Me-Si-Al-O-N. The phase diagram of a five-component such as this can be conveniently represented by Jänecke's prism[116].
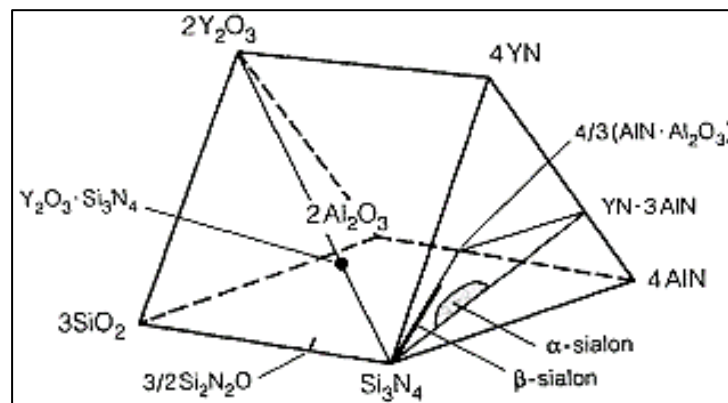
Fig. 2. 19: Part of the Y-Si-Al-O-N system drawn as Jänecke prism. All the structural forms of SiAlON can be seen here[116]

The fig. 2.19 illustrates the phase diagram of the system Y-Si-Al-O-N in which Y₂O₃ is added as a sintering aid. The O¹ phase that forms due to the addition of Y₂O₃ is refractory in nature,

making Y_2O_3 a popular choice as a sintering aid. Addition of other rare earth oxides can create different refractory phases hence facilitating application-based tailoring of the composition.

2.4.2 Properties of doped SiAlON

Via the process of HIP or pressureless sintering, single-phase SiAlON can be produced by adding Al_2O_3 and AlN to Si_3N_4. The amount of the glassy phase can be very little or not exist at all. Addition of rare earth oxide to this system even in the smallest amounts can make a huge difference to the amount and composition of the glassy phase and its effects on the ceramic[4,131]. Ekström and Nygren[4] conducted experiments exclusively on the varying phase composition, microstructure and properties of the SiAlON ceramic with the varying amount and type of sintering aid added. From one of their experiments, they concluded that in the low substituted $Si_{3-x}Al_xO_xN_{4-x}$, a change in the grain size was observed as the value of x was modified. As x increased from 1 to 2, the grain size increased. Smaller values of x resulted in generally rounded grains. As the value of x increased > 2, the grains got elongated. The low substituted β SiAlON formed within this ceramic system was quite like β Si_3N_4 in terms of its properties. However, as the value of x increased, the fracture toughness and the hardness properties deteriorated. This happened due to the coarsening of the grains and the absence of the glassy phase. Addition of Y_2O_3 significantly increased the amount of glassy phase required for the sintering. The preferred ratio was concluded to be as Si:Al:Y = 2:2:1 for a good proportion of the glassy phase[4]. This allowed the tailoring of a preferred crack path and crack branching aiding to the increase in the fracture energy of the ceramic. There was also a correlation observed between the amount of rare earth oxide used and the oxidation resistance of the ceramic. The oxidation rate increased as x increased due to

O_2 diffusing through Al containing amorphous phase than through amorphous SiO_2. Likewise, as the amount of the rare earth oxide decreased, the oxidation rate increased[4].

2.4.3 O^1-SiAlON phase or "Si_2N_2O" ceramics

The Si_2N_2O ceramic is an interesting ceramic at high temperatures. Formation of this phase is often sluggish because of the hindrance of the kinetics by the activity between Si_3N_4 and SiO_2. Sintering aids can help with the reduction in the activation energy, but this addition can have a negative influence on the oxidation resistance of the ceramic. For the formation of Si_2N_2O, the most attractive aid is Y_2O_3. On the other hand, CeO_2 can be added as the least expensive alternative (cost of MgO, CaO< cost of CeO_2 < cost of Y_2O_3). CeO_2 forms an eutectic with SiO_2 at a high temperature, making the liquid phase stable. However, among the experiments conducted, the combination of Y_2O_3 and Al_2O_3 was considered as the best since it facilitated pressureless sintering of the SiAlON ceramic[4]. This combination yielded a high content of the O^1 phase with good overall density (>90%). From the fig. 2.18, it can be seen that Si_2N_2O is a narrow solid solution range in the area of $Si_{2-x}Al_xO_{1-x}N_{2-x}$ where $0 < x < 0.2$. With the addition of Al_2O_3, AlN and Y_2O_3, full density β SiAlON can be achieved with pressureless sintering at 1800^oC. Y_2O_3 has been proven to aid the solidification initiation from 1600^oC onwards.

The mechanical properties of the O^1 phase are difficult to analyse since it is not possible to fabricate or isolate just this phase alone. However, during Ekström and Nygren's experiments[4], they were able to fabricate almost pure Si_2N_2O phase by HIPing Si_3N_4 at 1900^oC with the additives; table 2.8 provides some of the mechanical properties.

Table 2.8: Mechanical properties of the almost pure Si_2N_2O phase[4]

Property	Experimental value
Hardness, HV_{10}	1600
Fracture toughness	3.3 $MPam^{-1/2}$
Modulus of rupture	420 MPa

The poor toughness of this phase is attributed to its strong bonding with the SiO_2-rich glassy phase. This strong bonding makes it easier for the crack to proceed through the glass and the crystals. There is no potential pull out or no crack branching observed and hence, a low fracture toughness value. The hot hardness of this phase is preserved until $1200^{\circ}C$. However, the addition of Y_2O_3 and Al_2O_3 is observed to have a negative effect on the hot hardness due to the promotion of the liquid phase.

2.5 Fabrication methods of SiAlON

SiAlON fabrication process comprises of all the stages mentioned in section 2.1. However, stage 2 (consolidation/shaping) and stage 4 (densification) are of significant interest since these stages impact the end microstructure and properties of the ceramic. Different processes of the different stages mentioned in section 2.1 are mixed and matched to obtain the highest quality of the SiAlON ceramic. The following text briefly summarises some of the research conducted on the same.

Arias[132] at the National Aeronautics and Space Administration successfully densified SiAlON ceramics with the help of Y_2O_3 as a sintering aid. The fabrication was carried out by alloying Si_3N_4 with Al_2O_3 and AlN. The amount of sintering aid was as little as 1.1 wt.%. Consolidation was carried out by cold pressing uniaxially followed by isostatically under 207

kPa and 483 kPa respectively. Densification was carried out in a pressureless non-flowing nitrogen atmosphere at 1760°C. The final ceramic had a density of >98% of the theoretical value. The modulus of rupture was measured to be 460 MPa at ambient temperature and 155 MPa at 1400°C. Oxidation studies were conducted on samples with varying Al_2O_3 and Y_2O_3 content. Increase in the Al_2O_3 content showed better oxidation resistance whilst an increase in the Y_2O_3 had a negative influence on it.

Jiang et. al.[133] fabricated SiAlON ceramics via the gelcasting method. With a content of 25% of resin (a mixture of binder, dispersant and lubricant), samples were made with a solids loading of 44.5%. As for Arias' work[132], sintering was carried out in pressureless non-flowing nitrogen. An increase in the density of the ceramic was observed with an increase in the solids loading content. Table 2.9 shows some of the mechanical and physical properties of the green and the sintered ceramic whilst fig. 2.20 shows some microstructures of the green and the sintered sample respectively.

Table 2.9: Some properties of the green and the sintered sample from the 44.5 vol.% slurry[133]

| Property	Value
Solids loading / vol%	44.5
Green density / gcc^{-1}	2.04
Sintered density / gcc^{-1}	3.14
Microhardness / GPa	16.5 ± 0.8
Flexural strength at 20°C / MPa	295.2 ± 38.1
Flexural strength at 700°C / MPa	281.4 ± 33.1
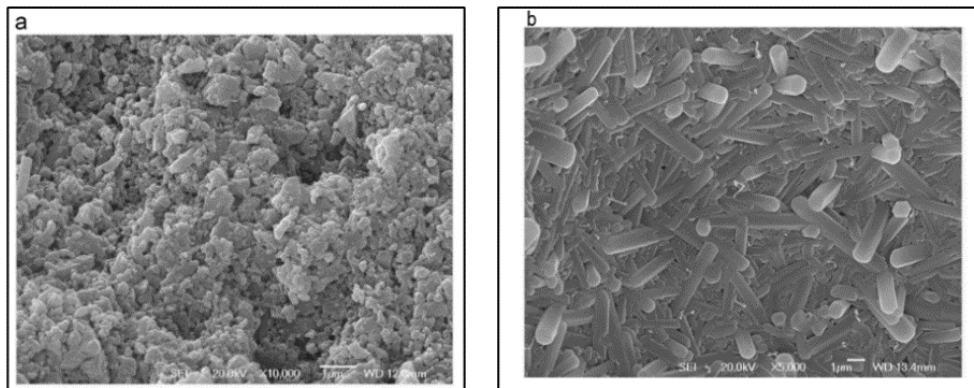
Fig. 2.20: The microstructure of a. the green body and b. the sintered sample[133]

Amin et. al.[134] synthesised Ca α-SiAlON powders by the carbothermal reduction nitridation method. The precursor was prepared via the sol-gel method by combining silica, alumina and calcium oxide. Glucose acted as a gelling agent and a carbon source in the colloidal system and was also observed to be responsible for the homogeneity of the precursor powders. The densification was carried out in a non-flowing nitrogen atmosphere. With the help of X-ray diffraction studies (XRD) of heat-treated samples at different temperatures, the formation of the O^1, β and α SiAlON were identified.

Among other processes, SiAlON ceramics were also fabricated from polymers. Koneggar et. al.[135] studied the interaction between polysilazane and the fillers used, Al_2O_3 and Y_2O_3 stabilised ZrO_2, since on pyrolysis polysilazane yields silicon related ceramics. The samples were warm pressed and densified in a pressureless non-flowing nitrogen atmosphere. It was concluded that the density of the final ceramic depended on the filler used. Samples having alumina as a filler produced β SiAlON ≥ 1300°C. Samples having zirconia as a filler produced α SiAlON ≥ 1300°C. Table 2.10 also gives the measured densities of the end ceramic at different stages of the heat treatment whilst fig. 2.21 shows the microstructures of the ceramics obtained at different temperatures.

Table 2.10: Physical properties of the samples prepared from polysilazane[135]

Material	Calculated density / gcc^{-1}	Pyrolysis temp. / °C	Total porosity / %
Polysilazane /Al$_2$O$_3$	3.66	1000	24.1
		1200	26.3
		1400	30.2
Polysilazane /ZrO$_2$	5.32	1000	23.7
		1200	21.1
		1400	5.9
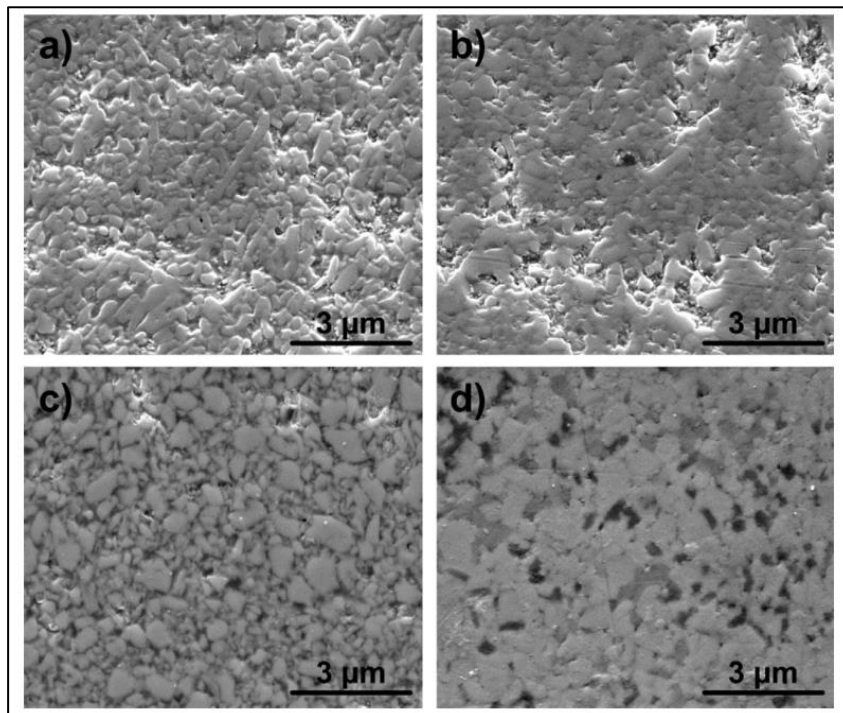
Fig. 2.21: SEM of polysilazane derived ceramics a. polysilazane / Al$_2$O$_3$, 1000°C; b. polysilazane / Al$_2$O$_3$, 1400°C; c. polysilazane / ZrO$_2$, 1000°C; d. polysilazane / ZrO$_2$, 1400°C[135]

From the recently developed field-assisted sintering techniques (FAST), SiAlON has been densified via spark plasma sintering (SPS). Li et.al[136] have presented their research results on the fabrication of β SiAlON via a two-step SPS process. Samples containing different amounts of Al$_2$O$_3$, AlN and Y$_2$O$_3$ were fabricated as shown in table 2.11.

Table 2.11: Compositions and the sample names used in Li et. al.[136] research work

Composition / wt.%			
Si_3N_4	Al_2O_3	AlN	Y_2O_3
85	6	3	6
90	4	2	4
92	4	2	2

The densification was carried out in two stages. Stage 1 was SPS under non-flowing nitrogen at 1600°C for 20 min whilst stage 2 was SPS under nitrogen pressure of 24 MPa at 1425°C for 5 min. Use of both the stages produced β SiAlON with the mechanical properties shown in Table 2.12.

Table 2.12: Some of the properties of β SiAlON obtained after each stage of SPS[136]

Property	Stage 1	Stage 2
Density, g/cc	3.18	3.24
Hardness, GPa	14.82	15.95
Fracture toughness, MPam$^{-1/2}$	6.68	7.03

The use of SPS assured no reaction between the ceramic and the mould used. As seen from table 2.13, two stage-SPS yielded a SiAlON ceramic with better mechanical properties compared to the single stage process. This study can be assumed to be analogous with the two step sintering developed by Greskovich[124]. The sample containing 4% Al_2O_3, 2% AlN and 2% Y_2O_3 that was 2-stage sintered clearly shows the fibre-like, interlocked structure of the β phase, which contributed to it having the best combination of mechanical properties out of the samples investigated, as shown in fig. 2.22.
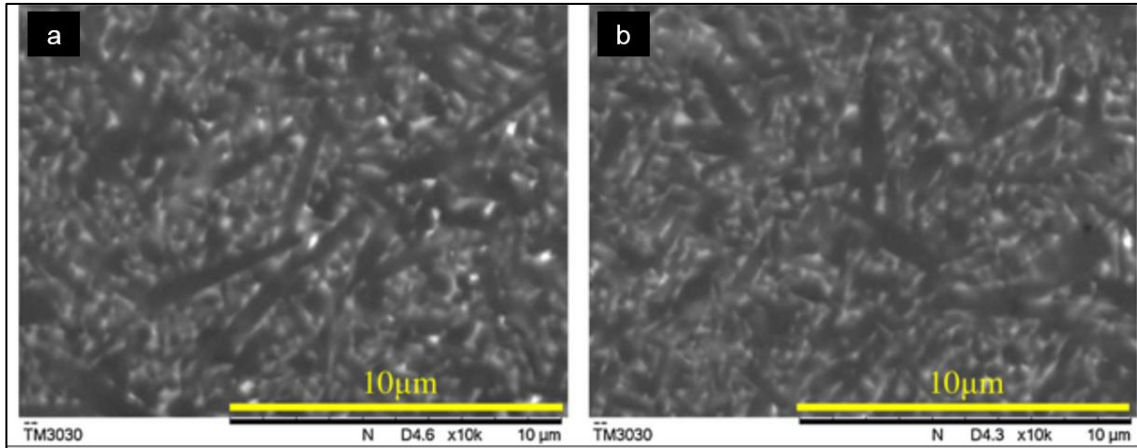
Fig. 2.22: SEM micrographs on polished surfaces after 2 stage sintering at 1425°C, a. the sample consisting 85 wt.%; Si_3N_4; b. sample consisting 92 wt.%; Si_3N_4[136]

2.6 Oxidation of Si_3N_4 based ceramics

Several researchers have conducted oxidation studies at temperatures >1000°C on Si_3N_4 based ceramics to investigate its high temperature properties. The oxidation behaviour of Si_3N_4 based ceramic mainly depends on its glassy phase[119]. Due to the softening of the glassy phase at high temperatures, mechanical properties have been observed to deteriorate. Therefore, the oxidation behaviour is mainly dependent on powder properties, processing and, in particular, the type and amount of sintering additives[119].

It is a well-established fact that the oxidation of Si_3N_4 based ceramics is controlled by the diffusion of reactants[4]. The rate of diffusion is given by Fick's first law:

$$\frac{dm}{dt} = DA_o \frac{dc}{dx}$$

Eq. 2.4

where dm is the mass of the reactant diffusing across a distance dx in time dt, dc is the concentration gradient across the oxide scale, A_o is the cross-section area through which the reactant diffuses, and D is the diffusion constant of the reactant.

If the oxidation process of Si₃N₄ based ceramics is monitored by studying the weight increase (Δw) as a function of time at a specified temperature, the parabolic rate law[1,4,7,13,127] can be rewritten as

$$\frac{\Delta w^2}{A_o} = K_p t^2 + B$$

Eq. 2.5

where K_p, is the parabolic rate constant and B is a constant. Thus, if a uniform compact oxide scale is formed, if A_o is constant during the oxidation process, and if the reaction is diffusion controlled, this relation should be valid.

Oxidation of Si₃N₄ based ceramics may occur by two mechanisms, depending on the oxygen partial pressure[119] namely active and passive. Active oxidation takes place at low oxygen concentrations, leading to volatilization of SiO, associated with weight loss. Passive oxidation, however, which occurs at higher oxygen levels in the atmosphere results in the formation of a protective layer and may be represented by[1,4,119,137]

$$Si_3N_4\ (s) +\ 3O_2\ (g) \rightarrow 4SiO_2\ (s)\ +\ 2N_2\ (g)$$

Eq. 2.6

In case of pure Si₃N₄ the diffusion of O₂ within the oxide scale rather than the outward diffusion of the nitrogen formed by the oxidation controls the kinetics of the growth of the oxide scale[4,9].

In case of SiAlON-based ceramics prepared without, or with various amounts and types of sintering aids, the oxidation rate is generally higher than that of Si₃N₄ as the grain boundary phase eutectic temperatures reach quickly[7]. Some of the oxidation processes taking place are much more complex depending in particular on the composition of the material. Different sintering aids affect the behaviour of the intergranular phase differently[4]. Si₃N₄ containing

metal-oxide sintering additives oxidize more quickly compared to pure Si_3N_4 particularly as grain-boundary-phase eutectic temperatures were reached.

The variations of oxidation rates with additive system and with overall composition within a given system led to the identification of cation diffusion to the surface under its chemical potential gradient as an important rate controlling step of the reaction mechanism[4,7]. This model of oxidation is shown in fig. 2.23. In addition to the cationic diffusion outwards from the ceramic to the oxide scale, the oxygen ions have to diffuse from the surface of the oxide scale to the interface between this scale and the ceramic. the oxidation-formed nitrogen has to migrate in the opposite direction. This could occur via diffusion of nitrogen ions or N_2 gas molecules[4]. This migration of N_2 forms craters or bubbles on the surface of the oxidised ceramic. Additive elements of very low concentration in the Si_3N_4 grain boundaries became concentrated in the surface of the oxide film[7]. Depending on the temperature of the oxidation, partly or a full amorphous scale of mullite and cristobalite is formed. In the case of oxidation of single α SiAlON, secondary phases such as silicates and aluminates of the additive elements along with AlN polytype are formed[138–140].
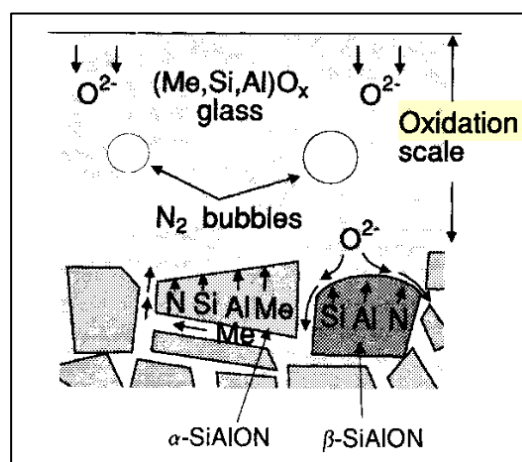
Fig. 2.23: Model of oxidation mechanism in SiAlON[4]

Oxidation also involves molar volume changes within the ceramic. It causes stresses in terms of volume expansion and tensile stress. This causes damage to the ceramic by inducing cracks or spalling. This type of damage was especially seen where Y_2O_3 was used as a sintering aid[7]. However, control on the volume of the glassy phase formed can avoid the damage[117,119].

More recent work has focused attention on providing surface protective barrier layers that inhibit oxidation. However, there has been only limited success. At high temperatures, although the barrier exhibited good oxidation resistance, it was observed to react with the underlying nitride[7,141]. Not much significant change in the oxidation behaviour was observed. Thus, there remains a need to develop surface films of improved resistance to the reaction at high temperatures with the substrate

Part D: Additive Manufacturing

2.7 Additive Manufacturing (AM)

The number of methods for consolidation is on a rise to reduce the number of steps in a fabrication process. This reduction in the number of steps can include cutting down on post processing operations such as grinding, polishing, annealing, time and the costs involved. One of the modern methods includes rapid prototyping (RP). It is a process for fast fabrication of a physical part, model or assembly using 3D computer aided design (CAD)[§]. Additive manufacturing is a type of rapid prototyping fabrication process. It is defined as a manufacturing method of a physical component by placing multiple layers on each other in

---

[§] www.twi-global.com

succession until the desired shape is obtained[142,143]. Fig. 2.24 illustrates the layered approach fabrication[144]. The other type of rapid prototyping method is known as the subtractive manufacturing, where the raw material is cut out of a workpiece until the desired shape is obtained.

The definition of AM given by the American Society of Testing and Materials (ASTM) is as follows: "The process of joining materials to make objects from 3D model data, usually layer upon layer, as opposed to subtractive manufacturing methodologies; Synonyms: 3D printing, additive fabrication, additive process, additive techniques, additive layer manufacturing, layer manufacturing, and freeform fabrication"[145].
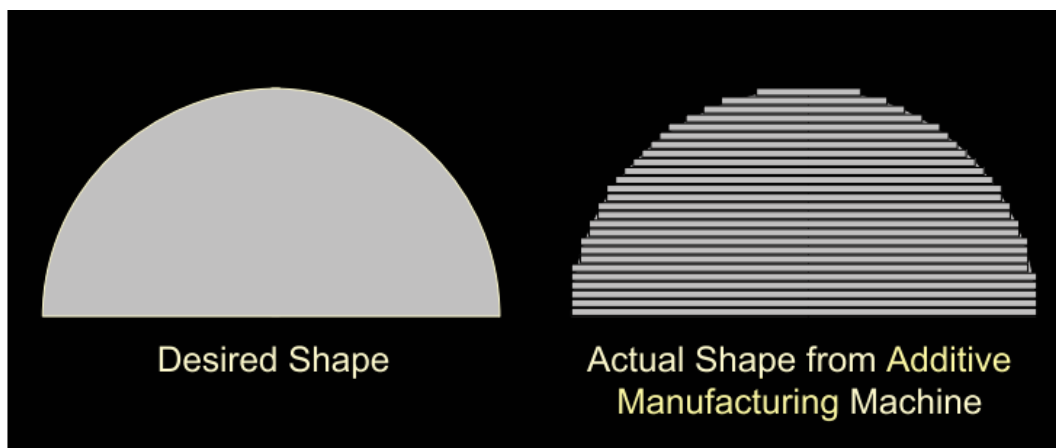
Fig. 2.24: A layered approach to AM[144]

The main advantage of AM is that any shape of any extent of complexity can be manufactured. It opens a way into digitalisation of processes without utilising the resources entirely. It also fits perfectly into the numerical design and the manufacturing chain of supplies. AM not only decreases the manufacturing costs and time of production but also increases the reliability of the process. Fig. 2.25 is a flow chart of any typical AM process[143].
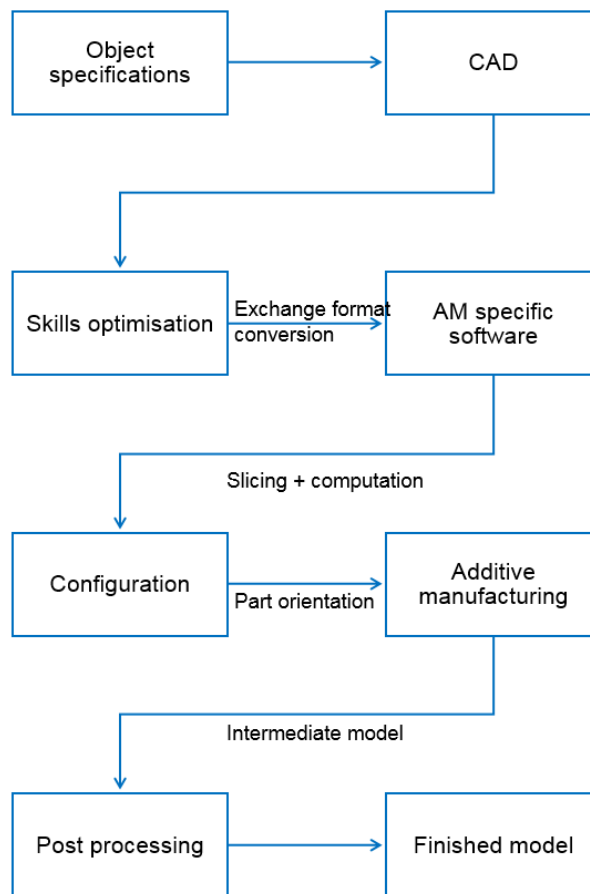
Fig. 2.25: A flowchart illustrating an AM process[143]

Firstly, a CAD of the component to be manufactured is created[143,146,147]. This file is exported in the format of STereoLithography or the Standard Tesselation Language (STL) (the STL format is usually the language of the equipment which performs the additive manufacturing. STL helps to visualise the physical component in terms of small triangles. These triangles address every part of the component specifying their unique coordinates within the printing space. More the number of these triangles, higher is the resolution of the components printed)[148]. Secondly, the STL file is fed into the AM unit and other parameters such as the orientation of the object, the number of units to be printed, individual slice thickness, etc. are

fixed. Finally, the AM process commences. After the final product is obtained, there can or cannot be post processing operations such as (apart from the removal of the object from the AM unit, removal of the support material) the polishing, grinding, etc.

Various parameters must be considered when additively manufacturing any component. Some of these parameters include the type of printing technology, the material used to print, the expected functions of the component (aesthetic/mechanical), [143,149]. The examples where AM can be seen are aeronautics, architecture, automotive industries, art, dentistry, fashion, food, jewellery, medicine, pharmaceuticals, robotics and toys[150,151]. Via AM, it is possible to realise extremely complex parts and their performance. The process paves the way to manufacture new products in the market in a short time. It also removes the assembly time, helps to optimise new topographical surfaces such as the honeycomb structure[152,153] (for lightweight and strong structures) which are otherwise difficult to fabricate via traditional techniques.

2.7.1 AM technologies

Researchers worldwide have adopted various methods of classification of AM technologies. The ASTM classification is based on binder jetting, material jetting, direct energy deposition, sheet laminations, material extrusion, powder bed fusion, and vat photo-polymerization. Table 2.13 provides an ASTM overview of the several AM processes.

**Table 2.13:** ASTM classification of the AM technologies[145]

Process categories	Technology	Materials
Binder Jetting	3D Printing Ink-jetting S-Print M-Print	Metal Polymer Ceramic
Direct Energy Deposition	Direct Metal Deposition Laser Deposition Laser Consolidation Electron Beam Direct Melting	Metal: powder and wire
Material extrusion	Fused Deposition Modeling	Polymer
Material Jetting	Polyject Ink-jetting Thermojet	Photopolymer Wax
Powder bed fusion	Selective Laser Sintering Selective Laser Melting Electron Beam Melting	Metal Polymer Ceramic
Sheet lamination	Ultrasonic Consolidation Laminated Object Manufacture	Hybrids Metallic Ceramic
Vat photopolymerization	Stereolithography Digital Light Processing	Photopolymer Ceramic

The following section describes the processes and the principles involved briefly. The processes are based on the classification on the hardening or the melting sources as given by researcher Gardan[143].

a. Laser based AM

There are four types of processes within laser-based[29,143,154] technologies. Though the processes differ in aspects such as the material being used, application temperature, etc., the main principle remains the same. A laser beam focused on the building material is responsible for the melting and joining of the particles. Fig. 2.26 illustrates the laser based AM processes.

Stereolithography[155,156] or SLA was the first developed AM technology and was developed simultaneously in the USA and France in 1986. The component is made using a photosensitive resin. After designing the component via CAD, the laser is focused on the photocurable resin in the shape of the CAD design. SLA can be used to manufacture small scaled ceramic components[143]. The ceramic powder is mixed into ultraviolet (UV) curable resin. The resulting suspension is then subjected to SLA followed by sintering for the final component. Microstereolithography is a version of SLA but on a much smaller scale. It is used for components measuring <10 μm.
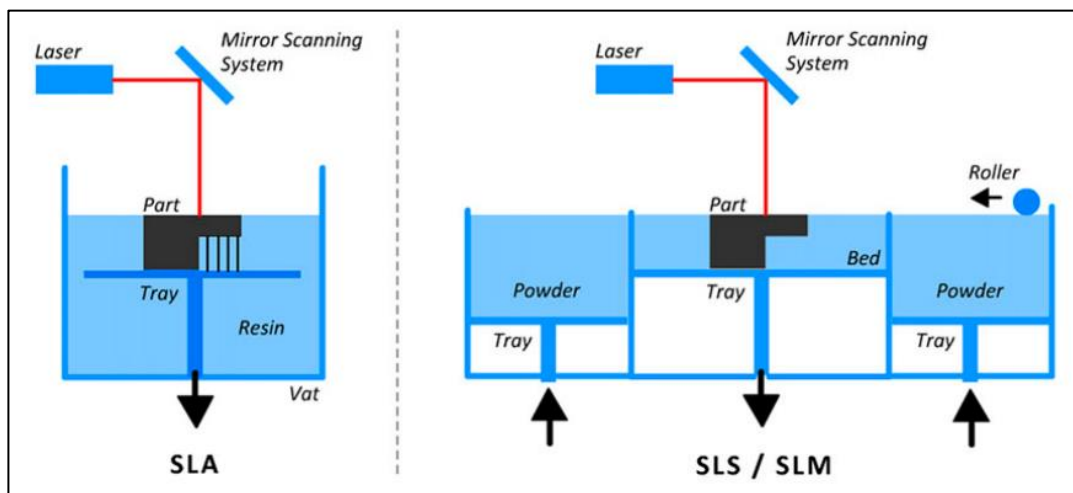
Fig. 2.26: Laser based AM technologies[143]

Selective Laser Melting (SLM)[157] is another method which builds components out of a powder bed of the building material. Like any AM process, once the STL file of the component is fed into the unit, the laser is moved and focused on the powder bed in the shape of the component. This step melts the powder and fuses it. This step is repeated by lowering the powder bed and pouring an extra layer of powder on the fused layer. The process keeps repeating until the whole object is formed. Some of the materials fabricated using this method include steel, stainless steel, Al, Cr, Ti, Co, etc. SLM is being developed

further including the use of double or multilaser beams for a faster and more efficient process.

Selective Laser Sintering (SLS)[143,156] is a method which is quite like the SLM process. The only difference from SLM is that SLS sinters the powder at a lower temperature than the melting point of the powder. Materials such as polyamide, steel, Ti, metallic alloys and ceramics can be fabricated using this technique. The components can be infiltrated to harden or to control the porosity in the component after the SLS.

Direct Metal Laser Sintering (DMLS)[142] is another laser AM technology very similar to the SLS process. This is for metallic alloys exclusively. The metallic powders are locally sintered according to the CAD design of the component. A new layer of powder is poured over the fused layer and the cycle is repeated until the final component is obtained. The powder bed usually consists of two kinds of materials. One of the powders has a higher melting point than the other. The powder with the higher melting point forms the solid matrix and the one with the lower melting point forms a liquid phase that helps to sinter the particles[143]. DMLS also uses support material since the powder alone cannot guarantee the stability of the object from being collapsed. DMLS is often used for small to medium sized complex parts to be used in the aerospace, medical and other industries.

b. Flash-based AM technologies

Flash-based technologies were developed as an attempt to improve on the speed and the time taken by the laser techniques. Especially derived from the SLA, flash-based technologies use an extensive UV curable photo masking system. The main method under the flash based AM is the Digital Light Processing (DLP) also known as the Film Transfer Imaging (FTI)[142,143]. A UV photopolymerisable material is the main building component. The

process starts with the first layer of the component being masked by the UV curable material. A projector then helps to shine the UV light on the entire surface rather than scanning points or moving through a line. Once the curing is completed on one layer the component is moved upwards from the resin and another film of the mask is applied. The process is repeated until the final component is obtained, see fig. 2.27.
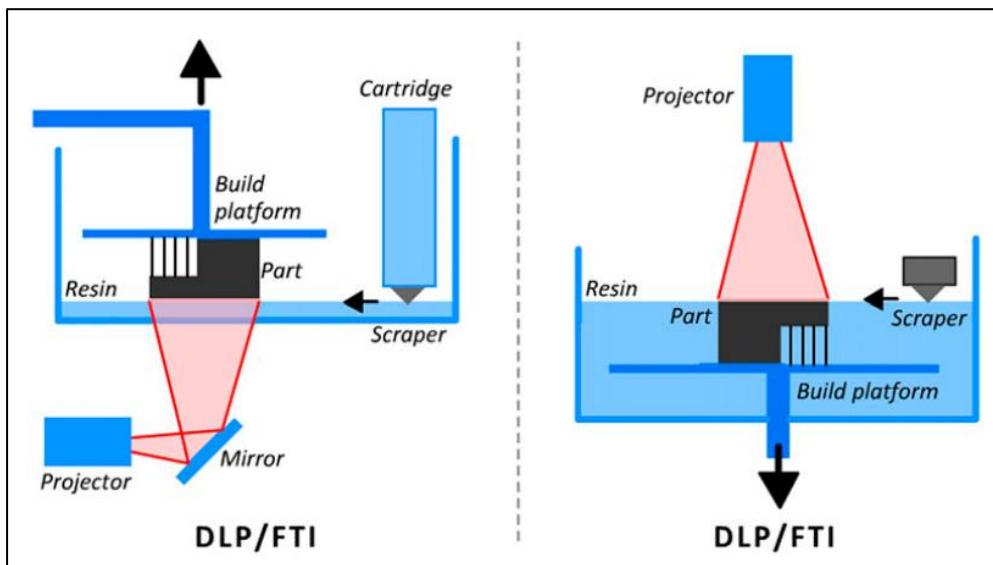

Fig. 2.27: Flash based AM technologies[143]

DLP method is much faster than the laser-based AM since the entire surface is exposed to the light at once. Unlike the SLA process, the part is pulled from the resin and built in an upside-down manner[143]. Due to this, much adhesion is required between the layers being built. Avoiding the peel off between the successive layers is extremely important. The build platform can also be placed at an angle where the projector is on the top and the component is being built at the bottom, as clearly illustrated in the fig. 2.27. This method assures higher resolution than the laser based AM up to a thickness of 50 µm.

c. Extrusion based AM

Fused Deposition Modelling (FDM) is a type of extrusion based AM process, developed and trademarked by the company Stratasys Inc., USA[143]. In this process, the thermoplastic filament is melted initially in a tank. This is then extruded through a nozzle where its fused deposited according to the CAD design. The component is built layer on a layer from the extruded filament. Not all materials can be used in the FDM process. Some of the common ones used are acrylonitrile butadiene styrene (ABS), poly lactic acid (PLA), poly carbonate (PC) and ethylene vinyl acetate (EVA)[158]. The final additively manufactured product differs in the properties because of the moisture content and ageing. FDM's main effect on the component is the anisotropy induced in it[28]. Apart from the main building material, there is often a support material being printed simultaneously. The support material is removed by either heating or dissolving in a solvent, which is used differs from system to system. The AM unit is portable and usually available in a tabletop version. It is a slower process and the resolution of the component is lesser when compared to the other AM technologies. Complex and bigger parts can take from hours to days depending on the capacity of the AM unit. Due to the mentioned limitations of the process, FDM is often limited to less professional applications.

Another extrusion based technology is Direct Energy Deposition (DED)[142,143,155]. This is an umbrella term for many processes such as the Layer Engineered Net Shaping (LENS), Directed Light Fabrication (DLF), Ion Fusion Formation (IFF), Direct Metal Deposition (DMD) and 3D laser cladding. The DED processes are usually employed to either add or repair a part to the already existing component. Most of these processes work on the principle of melting and depositing the material at the target. There is no size restriction within these

processes and the components can be several meters long. Fig. 2.28 illustrates the extrusion based AM processes.
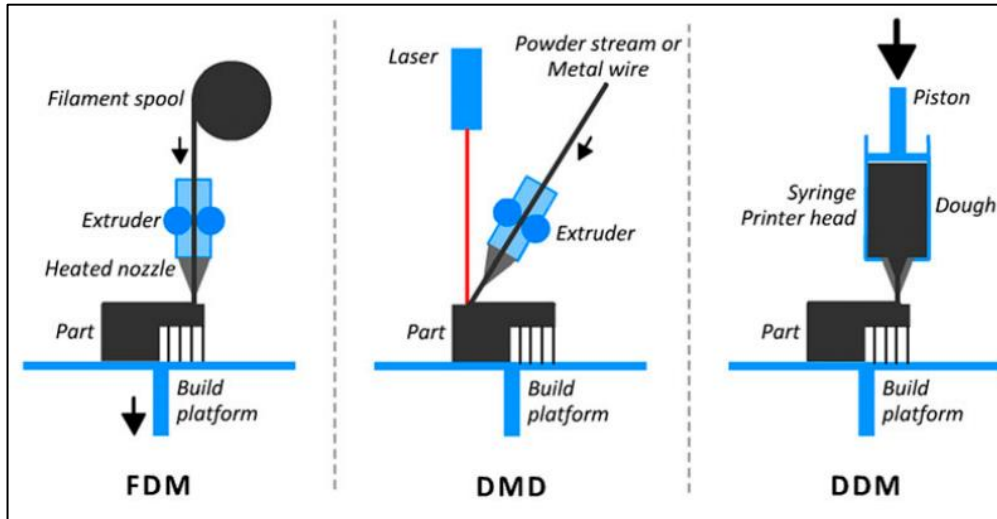

Fig. 2.28: Extrusion based AM technologies[143]

The food industry and the biomedical fields utilise the process of Dough Deposition Modelling (DDM). The process resembles injecting a dough into a syringe and depositing at the target with an application of pressure, fig 2.28. Medical applications include the addition of the biomaterials and cells to the tissue for repairs.

d. Jetting based AM technologies

Multi Jet Modelling (MJM) is a jetting based technology, illustrated in fig. 2.29[143]. The process helps in depositing droplets of a photopolymeric material with various jets on a building platform in the form of ultra thin layers[28,154]. These layers are then cured by using a UV source. There are usually two materials jetted - one is the main building material and the other is the gel based support material. The latter is removed by using a water jet after the curing. MJM provides with good dimensional accuracy and good surface finishing on the final object. A thickness of 50-25 μm can be easily obtained in the MJM process.
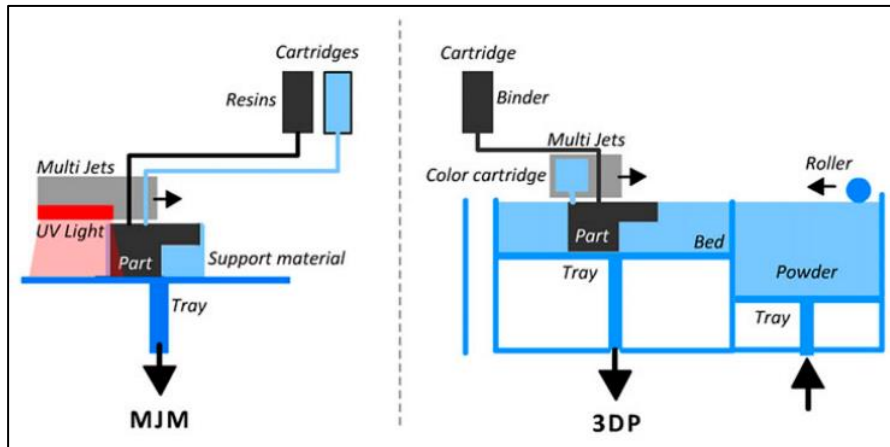
Fig. 2.29: Jetting based AM technologies[143]

Thermojet[143] process is an extension to MJM. It can be used to produce 3D wax models. It deposits tiny wax droplets which later cool and harden to form the object.

Colour Jet Printing (CJP)[143] also known as the 3D printing (3DP) is a process developed by the Massachusetts Institute of Technology. The process facilitates the combination of powders and binders. Once a layer of powder is sprinkled by a roller, the nozzle jets droplets of the binder to selectively link the powders[159]. The build platform moves downwards after every layer and the process repeats itself until the object is formed. Many metallic alloys, ceramic and polymeric materials can be used for any geometry. The final model is extracted from the powder bed and is infiltrated with special liquid glue. This glue is responsible to impart colour and shine to the object[154]. This process is especially popular with architects.

Another jetting process called as 'Prometal'[143] is used for fabrication of rapid tooling and dies. The main material used here is stainless steel. Post processing such as sintering, infiltration, polishing might be required after the printing process.

e. Lamination based AM technologies

The process of Laminated Object Manufacturing (LOM)[143] is used where the parts are made by successive pasting of the material in layers[142,149]. Commonly used materials are paper, wood, plastic, metal, woven fibre sheets, etc[160]. A forming tool on the top of the building platform helps to cut the papers into the desired shape. These layers are bonded together with the help of a heat sensitive glue. Finally, all the layers are laminated together with the application of heat and pressure from the top and bottom of the surfaces for the object[161].

Unlike metals, where a wide variety has been additively manufactured such as Al, stainless and tool steels, Co-Cr alloys, Inconel and Ni alloys, Cu alloys, Au, Ag and Pt[28,29,142,162], only a relatively small number of ceramics have been successfully investigated, including alumina, zirconia (yttria stabilised), SiC and reinforced composites[35,161,163,164].

2.7.2 Limitations of AM processes

Although AM is one of the trending concepts within the fabrication industry, a lot of its aspects still need to be assessed before it can replace conventional techniques within the metallic and ceramic [163,165] industries. Even after careful consideration of the materials and a selection of an AM technique for an application, there can be still some manufacturing constraints compared to conventional fabrication. Issues such as the orientation of the model in the AM process affects the quality of the geometry, the material gradient and the manufacturing direction[146]. Any specific part orientation of the object modifies the planarity, circularity and the surface accuracy of the object. The non-spherical particles used in the slurry tend to align the particles in the direction of shear flow giving rise to anisotropy in the objects[143]. Ageing in the UV curable materials and the crack propagation are some of the issues to be considered because of the induced anisotropy[146]. Unlike the conventional

techniques where the refined powders are preferred for higher densities, they can reduce the flowability and hence affect the density of the component. Additionally, not all the AM techniques promise the elimination of the post processing stages such as the sintering, polishing, machining, etc. Other issues such as the porosity, purity, micro-defects and interfacial defects still need to be addressed. Last but not the least, the raw materials can be expensive and the recycling of the scraps by the end of the process must be investigated. Greater details of each of the limitations can be found here[146,147,163], whilst Chartier et.al.[161] have highlighted some of the advantages and limitations of the leading AM processes for several materials in use in table 2.14.

Table 2.14: Leading AM techniques highlighting their advantages and limitations[161]

3D AM techniques	Tolerance	Advantages	Limitations
Material extrusion	1 mm	– Ease of support removal – Good mechanical properties – No material waste	– Precision limited by the filament diameter (about 1 mm)
Material jetting	0.05 mm	– High accuracy – Good surface finishing – Multimaterial process	– Cost of the ink – Limited to thin layers – Limited lifetime of the water based objects
Binder jetting	0.05 to 0.1 mm	– Wide variety of materials – Simple technology	– High roughness of the surface – Expensive technology – Poor mechanical properties – Use of toxic organic binders
Sheet lamination	0.1 mm	– High production rates possible – Wide variety of materials – Low costs – No need of support	– Low vertical accuracy – Poor surface finishing – Difficulties to produce hollow parts
Vat photopolymeriza-tion	0.01 to 0.1 mm	– Complex designs – Good surface finishing – Good mechanical properties – High accuracy	– Expensive photosensitive resins – Cleaning step necessary – Control of the vertical accuracy
Selective laser sintering powder bed fusion	0.2 to 0.5 mm	– High production rates possible – Complex designs – Low costs – Good surface finishing	– High roughness of the surface – Poor mechanical properties – Limited to materials which absorb IR light

Newer methods and newer AM units are constantly being evolved and developed from those already existing to facilitate additive manufacturing with more number of materials. Combining different AM techniques with various sintering processes for ceramics are also

in research. A couple of examples for this development include AM of components followed by chemical vapour infiltration (CVI) to fill up the porosity obtained post sintering[166,167] and simultaneous AM and FAST to cut down on separate sintering process[168].

2.8 Introduction to indirect AM (the "investment" approach)

As discussed in section 2.7, though the use of AM is increasing owing to its versatility, there are still some aspects that need further research to get on par with conventional fabrication techniques.

On the other hand, an attempt to overcome the above-discussed challenges led to the development of indirect AM (IAM) or negative AM[38,39,169]. This method was inspired by the lost wax casting process and comprises of additively manufacturing polymer moulds for ceramic [170,171]. This method is mainly based on the FDM process and works on the thermojet principle (refer to sec. 2.7.1, jetting technologies). The desired component's CAD geometry is built and additively manufactured from a sacrificial polymer. Ceramic components can be shaped within these moulds either in the form of powders or slurry. The green bodies are then separated by burning off the mould. This is followed by regular heat treatment and sintering processes to obtain the final ceramic component. The main advantage of IAM is that hard materials can be consolidated into complex shapes by using the sacrificial mould. The process is considered to be easier and cost-effective (depending on the AM unit used) compared to other processing techniques[39]. Applicable for shaping metals and ceramics, this process has yielded high density parts and better surface finish than most of the other AM processes. Researchers such as Khan et.al.[38] were successful in applying this technique for biomedical applications using apatite wollastonite and poly-lactide-co-glycolide as glass

ceramic implants and biopolymers respectively. Khan also studied the dimensional accuracy of an Al alloy component fabricated via IAM. It was concluded that the dimensional accuracy was lower and the surface texture better than those obtained from conventional techniques. However, the application of IAM can produce different results for different materials because of the kind of sacrificial material used. Khan also added that in his view IAM wouldn't be able to fabricate complex shaped parts, but rather concluded that IAM should be restricted to softer materials' fabrication. To date, IAM has been successful on soft materials such as glass, Al alloy and polymers[39,170,172].

Since the evolution of AM from small case to the big scale, many researchers are working on fabricating Si_3N_4 and SiAlON. Though no published papers exist as of the date this survey was conducted (30th June 2020), the company Lithoz (Austria), was successful in additively manufacturing SiAlON micro gas turbine as a part of the project ToMax, see, fig. 2.30[173]. Syalon 101, from International Syalons, UK, was used as the precursor ceramic powder. Additionally, the company 3D Ceram, France, was successful in manufacturing a Si_3N_4 disk of approximately 30 mm diameter and 3 mm thickness (which was exhibited at the Advanced Materials show, UK 2019). Researchers at Ceram 3D are trying to develop the AM process for the fabrication of complex shaped Si_3N_4[**].

[**] Personal communication (2019)
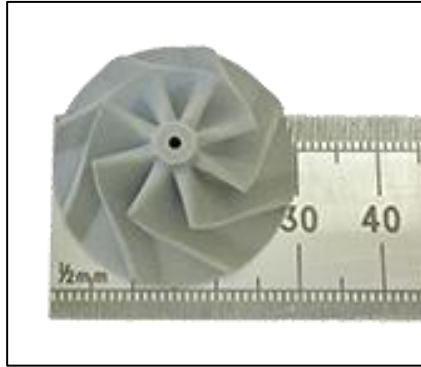
Fig. 2.30: SiAlON gas turbine fabricated by Lithoz in collaboration with International Syalons, as a part of the ToMax project[173]

The following experimental work is based on the IAM process of SiAlON components. This technique aims to fabricate a structural ceramic such as SiAlON into complex-shaped engineering components. The study aims at assessing the potential of IAM for the fabrication of high-performance ceramics including the challenges faced in the process.

CHAPTER 3

EXPERIMENTAL PROCEDURE

This chapter consists of four main sections. The first describes the additive manufacturing unit in detail whilst the second includes the experimental procedure along with a brief description of the raw materials used. The third discusses the parameters affecting the green body whilst the final section describes the characterisation techniques used to perform a qualitative analysis of the components.

3.1 The AM unit, Solidscape 3Z Pro

The AM unit used for this study was the Solidscape 3Z Pro, purchased from Solidscape by Prodways, New Hampshire, USA. It was the main source of the additively manufactured moulds for the study (Note: From hereon, the terms AM and printing will be used interchangeably). Fig. 3.1 is a photograph of the AM unit.
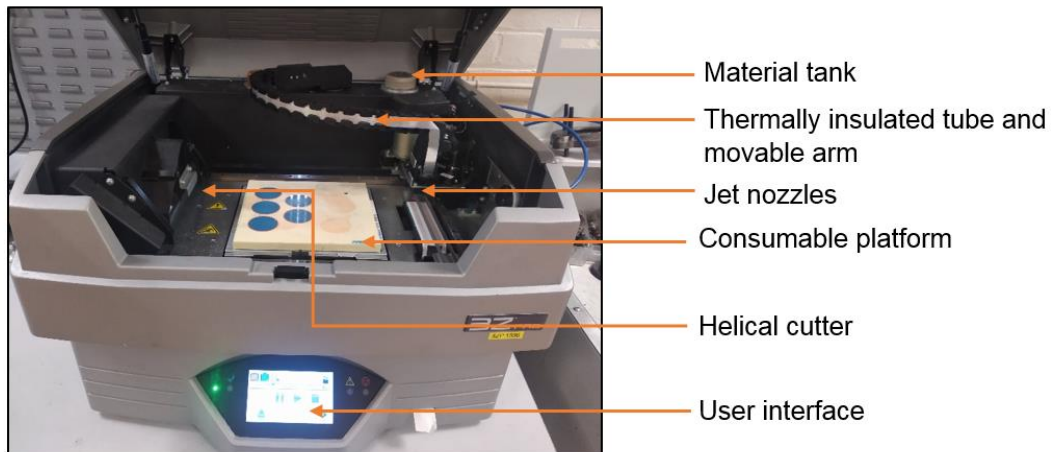
Fig. 3.1: Solidscape 3Z Pro – the AM unit used for the additive manufacturing of the moulds

The equipment described in fig 3.1 is a desktop model intended to manufacture moulds for the jewellery industry and is ideal for platinum, silver and gold casting. It is classified under fused deposition modelling, FDM, technology, specifically as a thermojet unit (see section 2.7.1). The main parts of the equipment are as follows:

a. Consumable platform – All the printing takes place on a polymeric foam platform which is movable upwards or downwards. The platform moves downwards from the base level after the printing of each layer. This means that the object is printed from the bottom first. The platform moves upwards to its original position after finishing the print job. The maximum range of this movement is approx. 100 mm. During the calibration of the AM unit, a thin layer (in the order of microns) of the platform is removed ensuring a flat and clean surface for the new print job. The standard dimension of the platform is 101.6 x 101.6 mm.

b. Material tanks – Two tanks are located behind the platform accommodating the build and the support material respectively. These tanks have enough heating capability to melt the materials. The temperatures can be programmed within the range of 0 to 150°C.

c. User interface/touch screen – The touch screen serves as an interface between the user and the machine. The options available include an overview of the machine and the status of the printing process. The user can start/pause/end the printing, calibrate the unit and troubleshoot the problems using this interface.

d. Cutter – The helical shaped cutter is responsible for maintaining the dimensional accuracy of the components by cutting down the excess material during printing.

e. Jet nozzles – There are two jet nozzles connected to the free end of the movable arm. They are responsible for jetting out, separately, the molten build and support materials.

f. Thermally insulated tubing for the material flow and the movable arm – This system of tubing transports the molten materials from the tank to the jet nozzles. The tubes are thermally insulated, ensuring that the materials remain molten and hence reducing the risk of clogging. Additionally, the system is free to move in the horizontal plane across the platform for any complex design jobs.

g. Vacuum powered cleaning unit – The whole AM unit is connected to a vacuum system, which sucks the debris and scraps from the platform during the printing process.

3.1.1 The additive manufacturing of objects on the Solidscape 3Z Pro unit

The process of additive manufacturing starts with the design of the component using CAD software. The file is then exported into .STL format and then transferred to the 3Z Modelworks (10.10.2 v) software. It is compatible with the AM unit and allows the user to set or change several parameters of the printing such as the slice thickness, number of units to be printed, extent of support material to be provided, orientation and placement of the object, scaling of the object, etc. It also estimates the printing time and the volume of the materials needed for the job. This file is then automatically opened in the 3Z Analyser (10.10.2 v) software. This software exports the .STL file to .3ZP format, which is the only format

recognized by the AM unit, to commence the job. Figures 3.2 and 3.3 illustrate screenshots

from CAD software, 3Z Modelworks and 3Z Analyser software respectively.
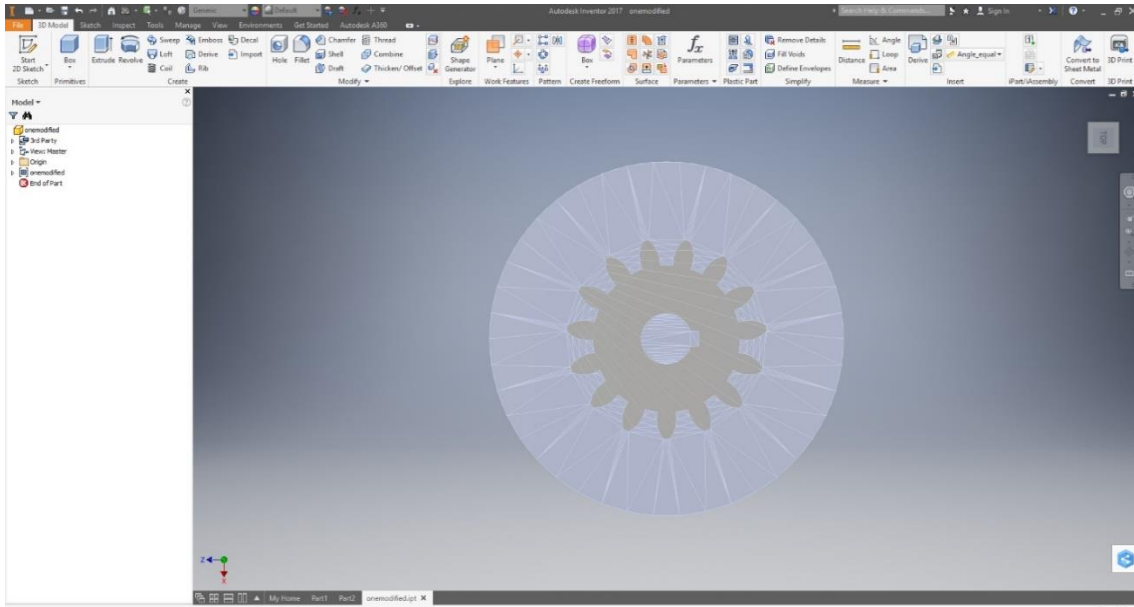
Fig. 3.2: A screenshot of the CAD software (Autodesk Inventor)
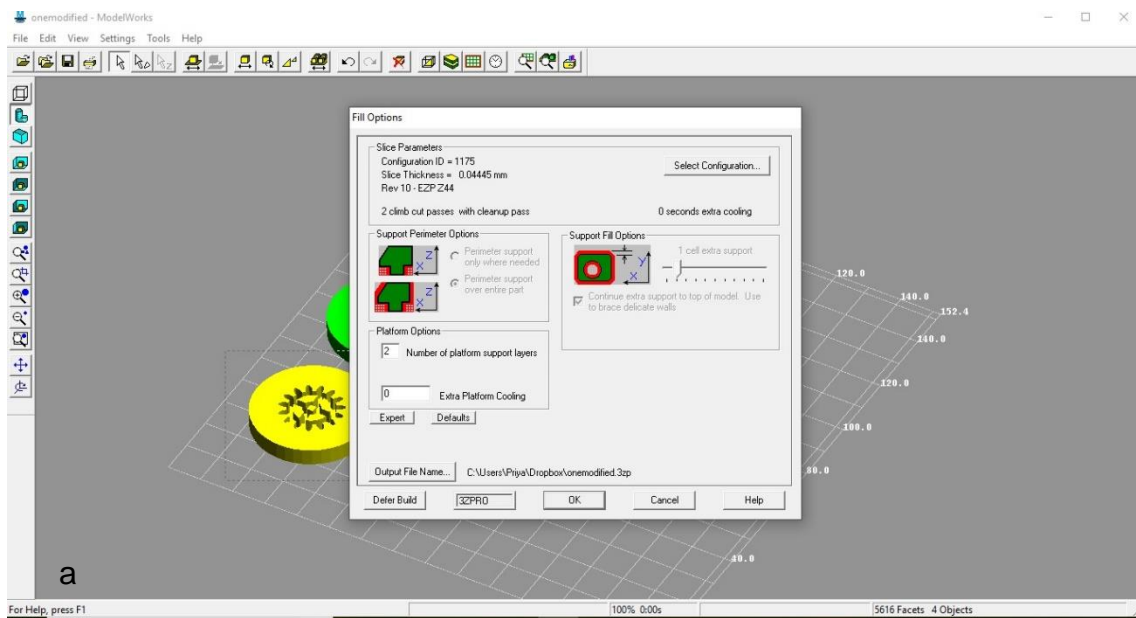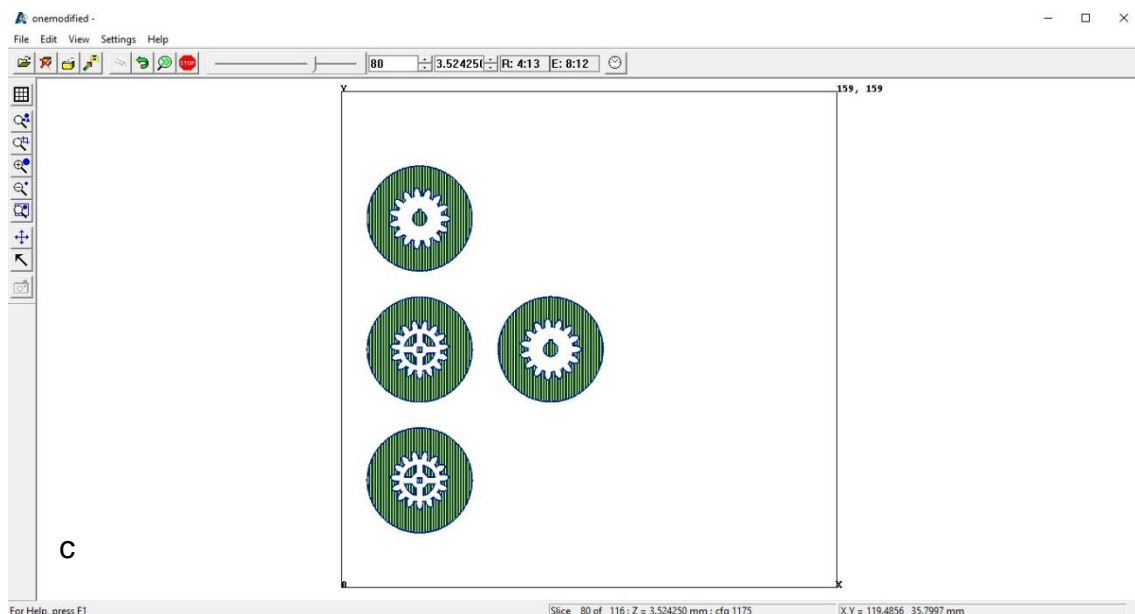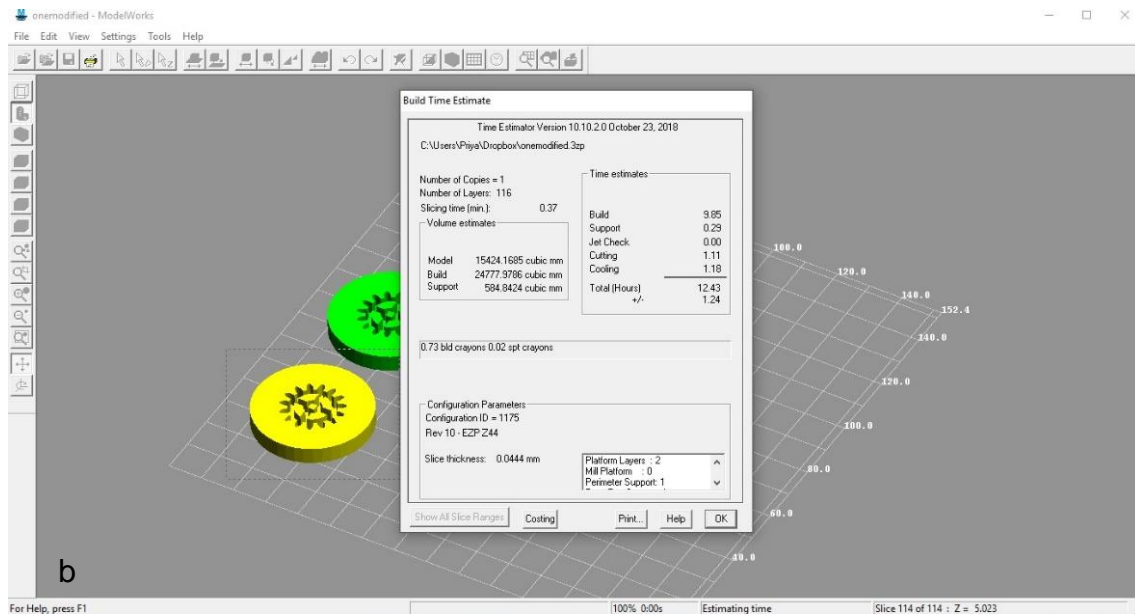
Fig. 3.3: Screenshots of the Solidscape 3Z Pro dedicated software, a). 3Z Modelworks – filling options such as the slice thickness, number of units and the extent of support for the object; b). 3Z Modelworks – window giving the time and material consumption estimate; c). 3Z Analyser – Print orientation of successive layers of the objects to be printed.

3.1.2 Materials used in the AM unit

Build material: This was custom-made for the AM unit and was purchased from Solidscape Inc. It was a thermoplastic material, made up of p-ethylbenzenesulfonamide, pentaerythritol tetrabenzoate and three other unrevealed polyesters. It dissolved in acetone almost instantly

and melted at approx. 135°C. Some characterisation tests were performed to understand its thermal, topographical and compressive behaviour. The results will be discussed in chapter 4 of this thesis.

Support material: It was custom-made for the AM unit and was also purchased from Solidscape Inc.[††]. It was made up of eicosanoic acid and melted at approximately 115°C. It was removed from the 3D printed component by ultrasonication in dewaxing oil (also provided from the same source).

Both of the materials were sold in the form of solid crayons that could be easily fed into the material tanks of the AM unit. They were safe, non-toxic and required no special handling. Figure 3.4 shows the packaged version of both the materials.

Fig. 3.4: Packaged versions of the build and support materials for the AM unit

---

[††] https://www.solidscape.com/products

3.1.3 The working of the AM unit
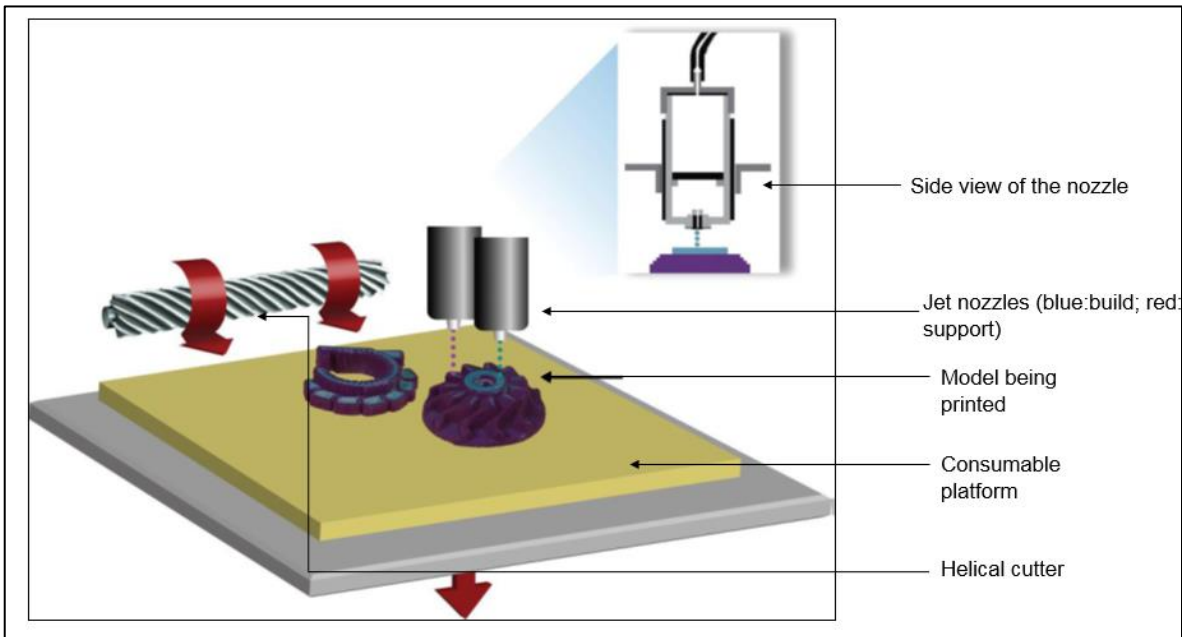
Fig. 3.5: Schematic illustration of the working of the AM unit[‡‡]

Figure 3.5 illustrates the basic working of the AM unit. To start the printing process, a crayon each of the build and the support material was fed into the respective material tank. While the calibration took place, the heated tanks melted the crayons. After the calibration, the final .3ZP extension file was input into the AM unit via an external drive. The file was read by the unit and the nozzles start jetting the material on to the platform in the shape of the designed geometry. The printing started with a designated number of support material layers. After printing a layer (with a specific slice thickness), the printing stopped momentarily, allowing the material melt to cool. This was followed by the helical cutter (rotating milling blade) moving across the platform and removing the excess deposited material. This action helped to maintain the dimensional accuracy of the object being printed.

[‡‡] https://www.syalons.com/

The platform was then lowered for the other layers to be built. The cycle of printing-cooling-cutting-lowering was repeated until the object was finished.

After the printing process was completed, the platform was detached from the unit and heated up to 115°C on a block heater. The heating melted the bottom-most support layers, displacing the model. Finally, the model was placed in a beaker containing dewaxing oil and ultrasonicated. This step helped dissolve the support material in and around the object. The duration of the ultrasonication depended on the size and complexity of the object that was printed, but times typically ranged from 0.5 – 72 h. After this step, the printed object was removed and was ready to be used. Figure. 3.6 shows some of the additively manufactured objects and their castings advertised as being capable of being manufactured by the AM unit.
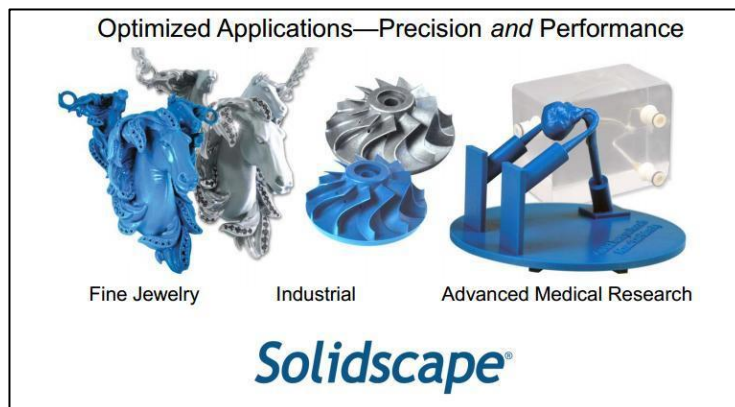
Fig. 3.6: Some examples of the printed objects from Solidscape 3Z Pro

Some of the unique features of the AM unit were as follows:

- The minimum feature size that could be printed was 0.254 mm.

- Models could be built with varying thicknesses of 0.006, 0.012, 0.025, 0.038, 0.051, 0.077 mm.

- Different types of models could be printed at the same time as long as they were of the same slice thickness.

- The dimensional tolerance of the AM unit was ± 0.025 mm in the X, Y, and Z dimensions.

3.2 Experimental

This section describes the work conducted for the fabrication of complex shaped SiAlON components. The flowchart in fig. 3.7 outlines the steps for the additive manufacturing of the moulds (refer to section 3.1.1 for the details). This is followed by a flowchart, fig. 3.8, that outlines the rest of the thermo-chemical process for the final SiAlON sintered components.
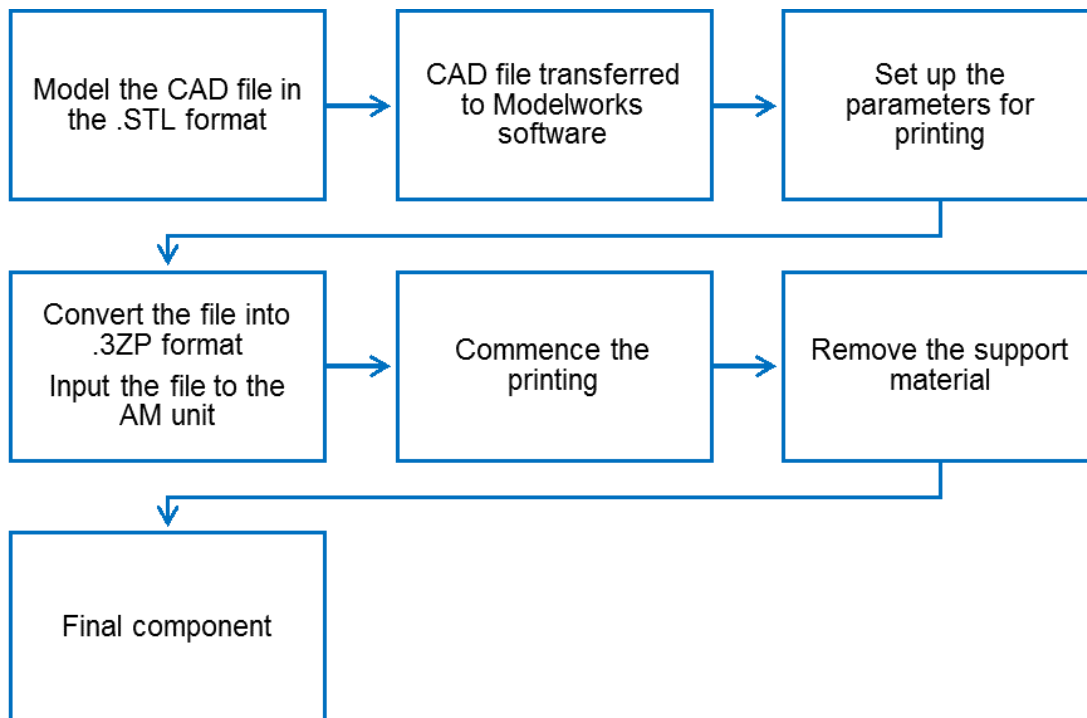
Fig. 3.7: Flowchart – the process of additive manufacturing.
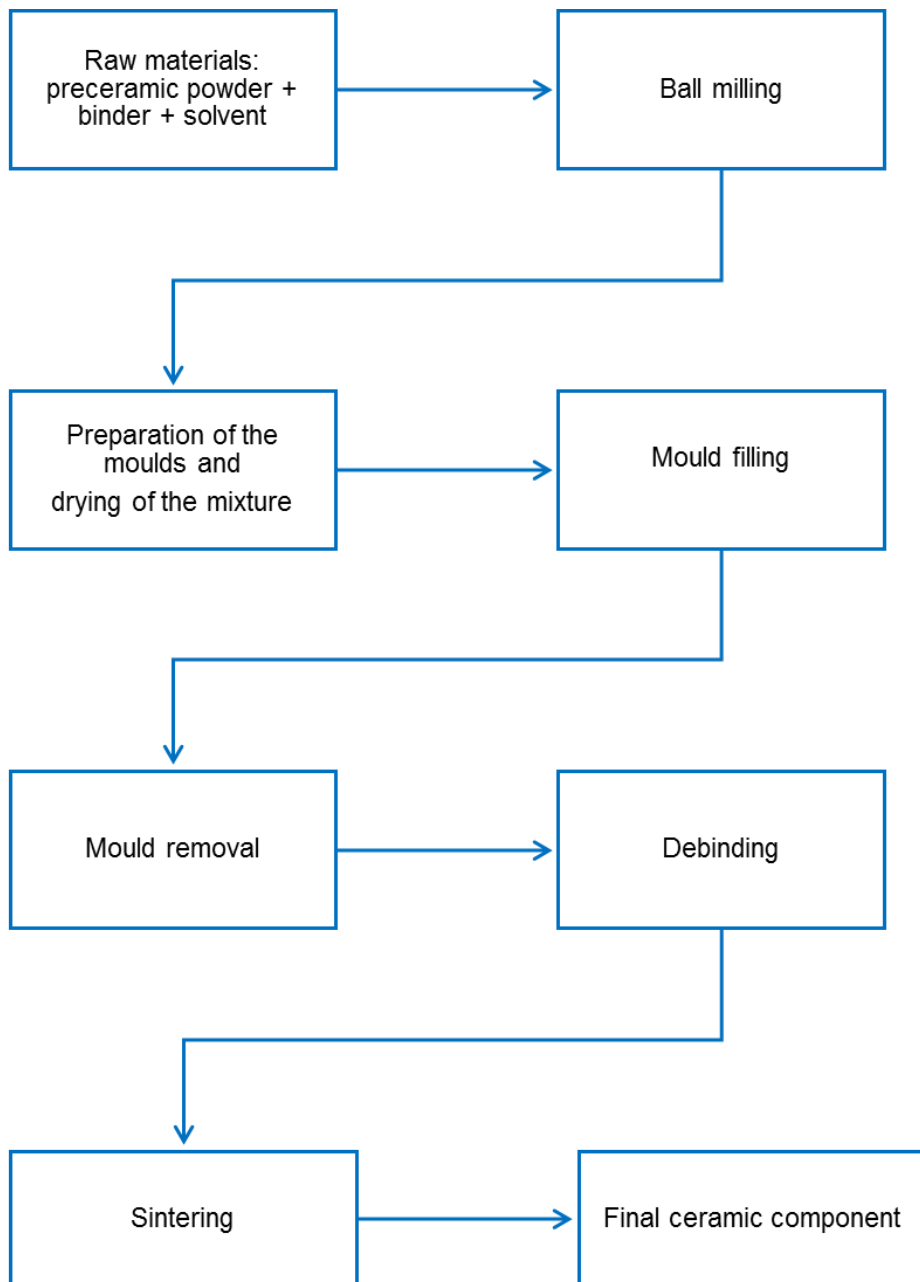
Fig. 3.8: Flowchart – the process for producing complex shaped ceramic components.

Fig. 3.8 describes the key stages of the fabrication process. Initially, the raw materials were weighed. The binder (5 wt.% of the total of ceramic powders and binder mixture) was then dissolved in deionised water and heated at 90°C for 45 minutes with occasional stirring. The resultant viscous melt was then mixed with the 95 wt.% of the ceramic powders. Then, the mixture was ball milled for 24 h, using ethanol as the solvent and alumina balls as the milling

media. In the meantime, the moulds were printed and sprayed with the Vitcas® heat resistant interfacial material which acted as an interface between the mould and the powder compact later on in the process. After the ball milling was finished, the powder slurry was dried at ambient temperature overnight to evaporate the solvent. The dried powders were then prepared for compaction, by adding ethanol in the same volume as the weight (ml : g) of the powders followed by thorough mixing. Addition of ethanol helped overcome the in-situ friction between the powder particles during compaction. The mould cavity was filled with an excess of this mixture and the filled mould placed in a simple die that was lubricated. As illustrated in fig. 3.9, the die was comprised of three parts - a base on which the filled mould was placed, a cylindrical housing enclosing the mould to contain the pressures, and a solid piston that acted as a force transmission medium during pressing. The filled mould was made to sit on the base in an upright position. This facilated the pressing of the powders by the piston. [Note: The geometrical shapes of the AM moulds and the die were custom made for compatibility].
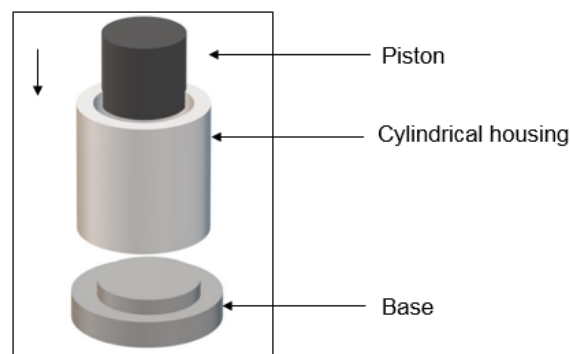
Fig. 3.9: Schematic illustration of the die used for compaction.

The powder was then compacted within the mould using a hydraulic press at a pressure of 110 MPa in the vertical uniaxial direction for 30 s. The mould was released from the pressure and carefully ejected from the die. The excess compacted powder on the mould was ground

78

carefully with grade 400 SiC paper until the shape of the component was revealed. The compacted moulds were then left overnight to evaporate the ethanol.

Subsequently, the moulds were placed on a thick bed of the ceramic powders and subjected to a heat treatment to melt the polymer mould. The heating rate was $0.2^{\circ}C$ min^{-1} in air and the final temperature was $150^{\circ}C$. The green bodies were removed at the end of the heat treatment and carefully transferred into a fresh powder bed where the melted mould material was completely removed by debinding in air at $600^{\circ}C$ using a heating rate of $0.2^{\circ}Cmin^{-1}$ and a dwelling time of 120 min.

In the final step, the fragile bodies (the ones subjected to debinding) were sintered in a high-temperature tube furnace at $1750^{\circ}C$ in a controlled atmosphere of flowing forming gas (95% N_2 / 5% H_2). The heating rate was $5^{\circ}Cmin^{-1}$, the dwell time was 180 minutes and the process concluded by allowing the furnace to cool at its natural rate. The sintered samples were removed and the excess powder from the bed was dusted off. This marked the completion of the fabrication process.

Note that many parameters and challenges affected the overall process, including the binder selection, the need for an interfacial material between the mould and powder (see section 4.1.3) and many others. Section 3.3 contains a discussion of these parameters whilst section 3.4 describes the finalized starting materials based on the investigations conducted in section 3.3.

3.3 Parameters affecting the fabrication process

The current research study was aimed at fabricating complex shaped components using structural ceramics. The objectives included obtaining 'a good green body' as a first

milestone. This was defined as a green body with close to the required dimensional accuracy to create a sintered body within the desired tolerances and having no cracks or flaws, no contamination and good structural integrity. From this definition, three important factors were identified that were responsible for the making of the green body. They were:

a. The binder

b. The mould characteristics

c. Effective mould removal and isolation of the green body

The three factors listed above were in turn dependent on several other parameters as illustrated in fig. 3.10.
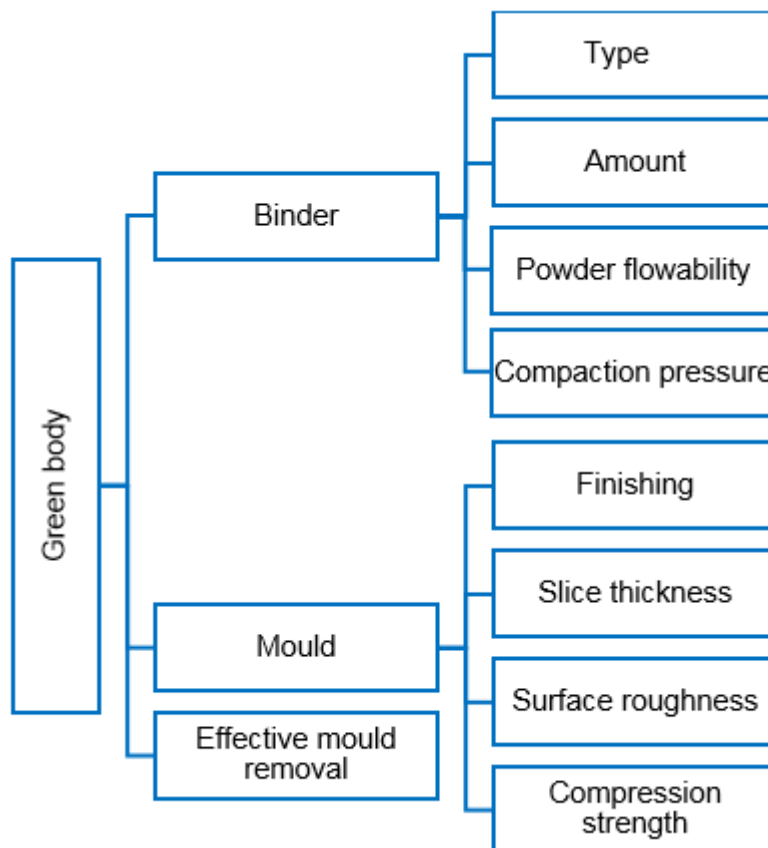
Fig. 3.10: A chart illustrating the parameters affecting the fabrication of the green body

Each of the factors affecting the green body and the successive selection of the parameters is discussed below.

3.3.1 The binder

Based on the process flow devised, the ideal binder was expected to exhibit the following requirements:

- The required powder flowability into the intricate design moulds;

- The required level of compaction under reasonable pressures;

- Good adhesion capacity, allowing for good retention of the structural integrity of the complex-shaped green bodies until the sintering process;

- Easy burnout after compaction;

- Chemical inertness between it and both the mould material and the ceramic powders;

- All of the above to be achieved whilst using minimal amounts of the binder.

The other important aspect of the fabrication process was the type of solvent. An ideal solvent was:

- Which dissolved the binder completely;

- Chemically inert towards the mould material and ceramic powders.

The experiments started with using an amount of 35 wt.% of binder which was eventually scaled down to 5 wt.% in the total powder mixture. This amount was chosen as a benchmark to investigate the binder's performance and versatility. If the binder qualified for its adhesion capacity, the amount was lowered, and green bodies were fabricated again to test if the adhesion properties retained. This was helpful to optimise the content.

Based on the above criteria, the following tests were performed to assess and finalise the binder for the study.

a. Type and amount of binder – Different binder systems were subject to visual and green strength tests. A simple assessment was done on the binder's capability to check if it could retain the green strength of the whole component until the debinding process.

Table 3.1: Different binder systems used for the binder selection process

Sample No	Binder system	Solvent	Amount added / % wt.
1	Poly Vinyl Alcohol (PVA)	Deionised water	35
2	PVA and starch	Deionised water	35
3	Poly-methyl-meth acrylic acid (PMMA) and PVA	Deionised water	35
4	Poly Ethylene Glycol (PEG) and PMMA	Deionised water / ethanol	35
5	Paraffin wax and stearic acid	Deionised water	35
6	Methacrylamide (MAM) and N-N^{1}methylenebisacrylamide (MBAM) [4:1] (ammonium persulfate (APS) as initiator-Tetra methylethylene diamine (TEMED))	Deionised water	35
7	Walocel™ CRT	Deionised water	20
8	Aquazol™ 500 (poly (2-ethyl-2- oxazoline)	Isopropanol / ethanol / deionised water	10 and 5

One of the challenges to initiate the research study involved finding a binder system compatible with the ceramic powders. Table 3.1 shows some examples of the binder systems investigated for the study. These were selected based on the criteria listed in section 3.3.1. The systems 1-6 (purchased from Merck Sigma Aldrich, Missouri, USA) in table 3.1 were used by other researchers in various fabrication[22,63,69,164,174–178] and were checked for their suitability in the current research study. Binder system 7 (sample obtained from Dupont, Delaware, USA) and 8 (sample obtained from Polymer Chemistry Innovations Inc., Arizona, USA) were selected from the research and their compatibility with the pure ceramic powders.

b. Effect of the binder on the powder flowability – The powder mixture obtained by mixing with each potential binder was subjected to several powder flowability tests (see section 3.5.3). The powder flow index (FF_c) was calculated to assess its potential to flow into intricately shaped mould cavities during compaction. The normal force was set to 2000 Pa, taken according to the stress tool calculator supplied by the manufacturer[§§] of the equipment used to measure the powder flowability.

c. Compaction pressure required during uniaxial pressing to achieve the desired green body density – A range of experiments were conducted to fabricate green discs using varying stress levels with the resulting green density being determined. That yielding the highest value but without any damage to the die was selected for subsequent use.

3.3.2 Characteristics of the mould

a. Green body surface finish – A good surface finish was required to remove the need for post-sintering operations such as grinding and polishing. Since the mould material could not be changed, experiments were conducted to assess the surface finish of the green bodies. During the mould removal stage, the green compacts were found to absorb the molten mould material due to capillary forces; though the shape was retained, the finish ended up being quite poor. To overcome this problem, the use of an interfacial material between the mould and the powder mixture was necessary to inhibit the capillary action. The interfacial material needed to be heat resistant to at least until 180°C, as well as chemically inert towards the moulds and the powder mixture. The selection of this material and its potential consequences will be discussed in detail in section 3.4.3 and 4.1.3 respectively.

[§§] https://www.dietmar-schulze.de/rstowe.html

b. Mould slice thickness – One of several important traits of an AM component is governed by its slice thickness. It is an important factor in understanding the resolution of the components. It refers to the axial resolution of the print being carried out. Improper selection of the slice thickness can result in anisotropy in the components. This deteriorates the mechanical properties in the +/- vertical (height/thickness) direction of the component. The selection of the slice thickness usually depends on the following factors:

- If the component has intricate designs and the visual looks are important
- If there is a possibility of printing the components with higher slice thickness at all. This implies less printing time and less material consumption and relatively better mechanical properties than the fine layered designs for chunky components.

However, some processes such as the SLS or SLM have overcome this challenge since the default resolution is already adequate for most of the applications. Additionally, several researchers are working towards high-grade thermoset materials which could remove the possibility of anisotropy[179,180].

The AM unit used in this research program could print AM bodies with fine structures and as well as simple block geometries. This is possible due to the different slice thicknesses that can be set before the printing commences. Therefore, to investigate which slice thickness could be beneficial for the current study, an investigation was conducted by printing moulds using three slice thickness values such as the 6, 19 and 38 µm separately. The investigation included just these slice thicknesses based on the AM unit's defined capability from its manufacturer. Any slice thickness beyond 38 µm was meant for bulky

components having less intricate features, e.g. a solid cube, a solid cylindrical block, etc. The results of this surface profilometric investigation will be discussed in the next chapter

c. Mould surface roughness – This affected the topographical quality of the green and sintered components. Hence, the surface roughness and profile forms were studied as a function of slice thicknesses and the presence of the interfacial material on the moulds. A separate study was conducted on the sintered samples to analyse their surfaces. This was done to check the potential for eliminating the post-processing process such as polishing.

Surface roughness, R_a is defined as the arithmetic average of the absolute values of the profile height deviations from the mean line, recorded within the evaluation length. Simply put, Ra is the average of a set of individual measurements of the surface's peaks and valleys. The calculation of R_a is given by[181].

$$R_a = \frac{1}{N}\sum_{i=1}^{N} Z_i$$
<div align="right">Eq. 3.1</div>

where N is the number of measurements and Z is the profile height deviation in µm.

d. Compressive strength – As the fabrication involved uniaxial pressing of the powders into the moulds, the compression strength of the moulds needed to be assessed. The measurements determined if the moulds could withstand the stresses during the compaction.

The compression strength is one of the characteristic properties of the mould governing the quality of the green body. It was critical to test the mould's compression strength to check it could withstand the uniaxial normal forces exerted during the compaction of the powders. A compression test was conducted according to the ASTM D695 standard for rigid plastics.

3.3.3 Efficient mould removal

Different heating rates were employed until crack-free green bodies were obtained. This included melting away most of the mould material. It was absorbed in a powder bed due to the latter's capillary forces.

3.4 Starting Materials

3.4.1 Syalon 050 (the ceramic powders)

Pure SiAlON (commercially known as Syalon 050) ceramic powder was purchased from International Syalons, Newcastle, UK. These powders were made up of the 21R polytype (see section 2.4.1) having the formulation $SiAl_6O_2N_6$ and had the composition outlined in table 3.2. Spray dried and Y_2O_3 alloyed SiAlON powders were received for the final fabrication. These were prepared from aforementioned 21R polytype, were greyish in colour and insoluble in water. According to the manufacturer, they had a D_{50} of <5.5 µm (this was independently measured and the results are presented in chapter 4) and on sintering yielded a mixture of α and β SiAlON phases. Note that the sintering aid Y_2O_3 made the heat treatment easier by facilitating pressureless sintering[***].

Table 3.2: The main composition of the Syalon 050 powders used within the study[182]

Property	Value / %
21R polytype (included Y_2O_3)	>97.5
Aluminium nitride (AlN)	<2.5
Iron (Fe)	<0.1
Calcia (CaO)	<0.02
Oxygen (O)	9.3

[***] Information from the manufacturer

3.4.2 Aquazol® 500 (the binding agent)

Aquazol® 500 was purchased from Polymer Chemistry Innovations Inc. (PCII), Tucson, Arizona, USA. It is chemically known as poly (2-ethyl- 2-oxazoline) and has the formulation shown in fig. 3.11.
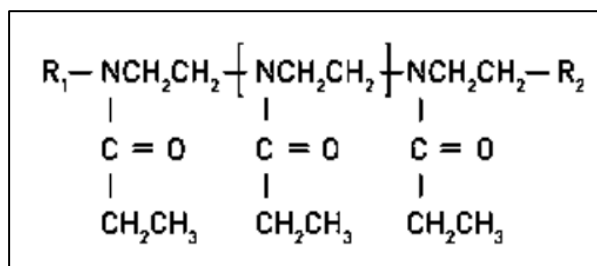
Fig. 3.11: Chemical formula of Aquazol® 500[183]

Aquazol® 500 has a reputation as an excellent alternative to poly vinyl alcohol, possessing added thermal stability. This formulation of oxazoline was relatively new to the ceramics market, though was well known for its use in the paint industry because of its excellent adhesive properties. As a result, it is used to renew archaic oil paintings[184,185]. According to PCII, this formulation was studied and improved by its researchers to broaden its range of applications to include being a ceramic binder as well as use in coatings, textiles, oil and gas, personal care, soap and detergent, water treatment, lubricants, etc[†††]. Aquazol® 500 is known for its excellent solubility in water and organic solvents that are easily available such as ethanol, acetone, etc[186]. It is a light yellow solid with a neutral pH and has a kinematic viscosity of $6 \times 10^{-5} - 8 \times 10^{-5}$ m^{2}s^{-1} and starts to chemically decompose from 380°C. It was chosen as the binder for the green strength that was provided to the additively manufactured parts.

[†††] https://www.polychemistry.com/products/aquazol/

3.4.3 Vitcas® heat resistant spray paint - red (the interfacial material)

Vitcas® heat resistant spray paint - red was purchased from Vitcas® Refractory Materials, Bristol, UK. This was sprayed on the internal mould cavity and acted as an interfacial material between the mould and the powder mixture during compaction. Its presence inhibited the capillary action of the powder compact during the mould removal process and provided a better finish to the green body.

However, because of the capillary actions of the powder compact, the surface finishing was poor. Hence, to avoid the capillary effect, a barrier/interface between the mould and the powder compact was necessary. An investigation into heat resistant, easy application materials led to the discovery of Vitcas® silicone spray paint. The efficiency of the interface was put to test by subjecting the powder compact within the interfacial mould to the mould removal heat treatment. The results will be shown in the next chapter. The spray paint was silicone resin-based and was available in the form of an aerosol. The typical drying time once sprayed was twenty minutes and the curing temperature was $160^{\circ}C$. It was heat resistant up to $300^{\circ}C$.

The ease of application on the mould, availability, inertness towards the moulds and the heat resistance of Vitcas® silicone spray paint allowed an almost immediate opportunity to investigate the feasibility of reducing the capillary action of the powder compact.

3.4.4 Ethanol (the solvent)

Pure ($\geq99.5\%$) ethanol (C_2H_5OH) was purchased from Merck-Sigma Aldrich, Vienna, Austria. It was used as a solvent throughout the fabrication process.

3.4.5 Forming gas (the sintering atmosphere)

To prevent oxidation during the sintering process, forming gas (95% N_2 / 5% H_2) was purchased from BOC Group Plc, Guildford, UK, in the form of cylinders of compressed gas and was used to eliminate the oxygen by purging the tube furnace with it three times before each sintering run and during the entire sintering process at a rate of 3 lmin^{-1}. The gas was non-flammable.

3.5 Characterisation techniques

Every step within the flowchart in the fig. 3.8 was qualitatively assessed. The aim of characterising the material at every stage was to understand the physical and the chemical state of the components being fabricated. Table 3.3 provides an overview of the characterisation techniques that were carried out throughout the process.

Table 3.3: An overview of the characterisation techniques carried out within the fabrication process

Type of material	Characterisation technique
Raw materials - ceramic powder	• Particle size analysis • SEM • Powder flowability • XRD
Ball milled dry powders	• SEM • Powder flowability • XRD
Additively manufactured moulds	• Compressive strength • Surface profile • TGA • Interfacial coating material effectiveness
Filled up moulds	• SEM • X ray computer tomography
Green bodies	• Density
Bodies subjected to debinding	• XRD
Sintered ceramic components	• SEM • Raman spectroscopy • XRD • X ray computer tomography • Density • Surface profile • Flexural strength • Oxidation studies

3.5.1 Density and shrinkages in the dimensions and mass

A standard densitometer (based on the Archimedes principle) sourced from Mettler Toledo, Ohio, USA was used to measure the density of the samples. The density was used to assess the quality of the ceramic, including the presence of pores. Shrinkage measurements in the dimensions and masses were used to provide tolerances for design criteria. The following procedure was used; the samples were weighed in air (W_a) and water (W_s) separately. The

density (ρ) was calculated according to the following formula (assuming standard laboratory temperature and pressure):

$$\rho = \frac{W_a}{W_a - W_s}$$

Eq. 3.2

and densities were determined for both the green and sintered components.

The shrinkages were calculated according to the following equations:

$$\% \ Shrinkage \ in \ dimension = \frac{D_g - D_s}{D_g}$$

Eq. 3.3

$$\% \ Mass \ loss = \frac{M_g - M_s}{M_g}$$

Eq. 3.4

where D_g and D_s are the dimensions of the green and sintered component (length, thickness, width, diameter, etc) respectively; M_g and M_s are the mass of the green and sintered components respectively. The dimensions were measured to 2 decimal places using callipers and the mass was measured to 2 decimal places using a laboratory weighing scale.

3.5.2 Particle Size Analysis (PSA)

One of the main assumptions of this analysis is that all the particles are spherical. Hence, the equivalent projections of a sphere were calculated for the size (diameter), surface volume, surface area from this analysis. Since the powders of Syalon 050 were fabricated via spray drying, the assumption of spherical particles holds to a high extent. Examining the particle size and its distribution affects the packing density during the compaction. Controlling the particle size at this stage can alter the grain size and the mechanical properties of the final component.

The PSA of the as-recieved ceramic powders was measured using a laser diffraction sensor-based automated particle size analysis facility (Helos / BR Sucell, Sympatec GmbH, Germany). The results indicated the particle size distribution of the powder and were used to determine if a milling process was required to attain uniform sized powders before the fabrication. Prior to the PSA measurement, the powders were initially dispersed in aqueous sodium pyrophosphate ($Na_2P_2O_7$) (as a deflocculant and stabilizer) solution and ultrasonicated within an in built ultrasonicating unit. Different concentrations of the stabiliser solution were used such as 0.1 M, 0.5 M and 1 M. However it was observed that some of the larger agglomerates failed to break down and hence subsequently 99% pure ethanol was used as the dispersant for the powders and the same ultrasonic regime used. This was found to be more successful and hence the powders were dispersed in ethanol in 1:1 wt.:vol. for the PSA.

3.5.3 Powder flowability

The powder flow index (FF_c) was investigated using a ring shear tester (RST) XS from Dr. Dietmar Schulze, Wolfenbüttel Germany. The measured FF_c helped qualify the binder to be used in compaction. It was important for the powder mixture to be free flowing so that it was able to penetrate the intricate crevices of the complex-shaped moulds, resulting in flaw-free components of the desired shape and density. Various ball milled compositions of the powder mixture containing different amounts of the ceramic powders, the binder and stearic acid (as a lubricant), were prepared for the test and the flow indices of these compositions determined. The compositions are shown in table 3.4.

Table 3.4: Various compositions prepared for the powder flowability tests

Sample no.	Compositions prepared
1	As-received Syalon 050 powders
2	5 wt.% binder + 95 wt.% Syalon 050
3	5 wt.% binder + 1 wt.% stearic acid + 94 wt.% Syalon 050
4	10 wt.% binder + 90 wt.% Syalon 050
5	10 wt.% binder + 1 wt.% stearic acid + 89 wt.% Syalon 050

The RST determined the flowability index by shearing a consolidated cake of powder under a predefined stress. The test also measured the compressive strength and bulk density of the powders along with the angle of internal friction between the powder particles. Fig. 3.12a shows an image of the RST equipment used, whilst 3.12b shows a schematic of the operating principles.
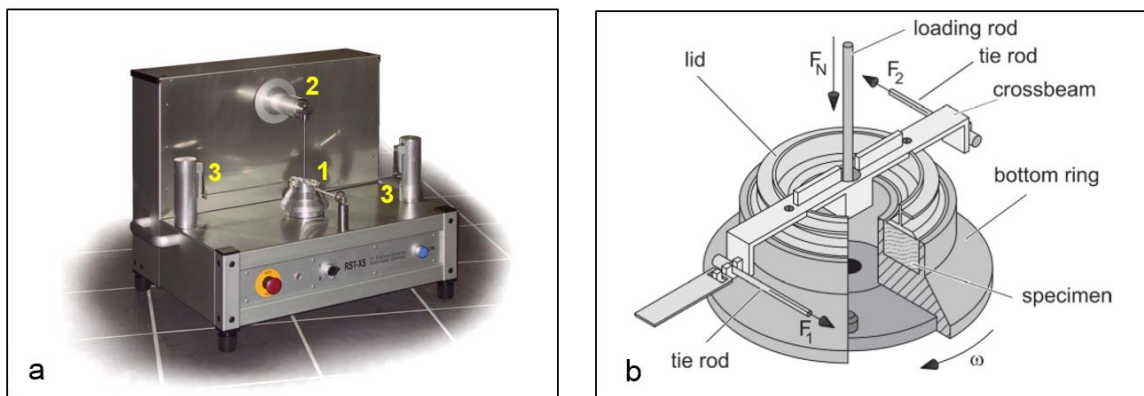
Fig. 3.12: a. The ring shear tester for measuring the powder flowability[187]. 1. The shear cell, 2. Computer-controlled source of the force, 3. Tie rods; b. the operating principles of the shear cell[188]

Initially, the powder was enclosed in a shear cell with a volume of 30 ml. A normal force was exerted on the cell resulting in the consolidation of the powder. The bottom of the shear cell was then rotated whilst the lid remained stationary because of the tie rods. This action exerted a shear force on the consolidated specimen, resulting in shear failure. The loading

of the forces on the shear cell and the corresponding construction of the Mohr's circle are shown in fig. 3.13.
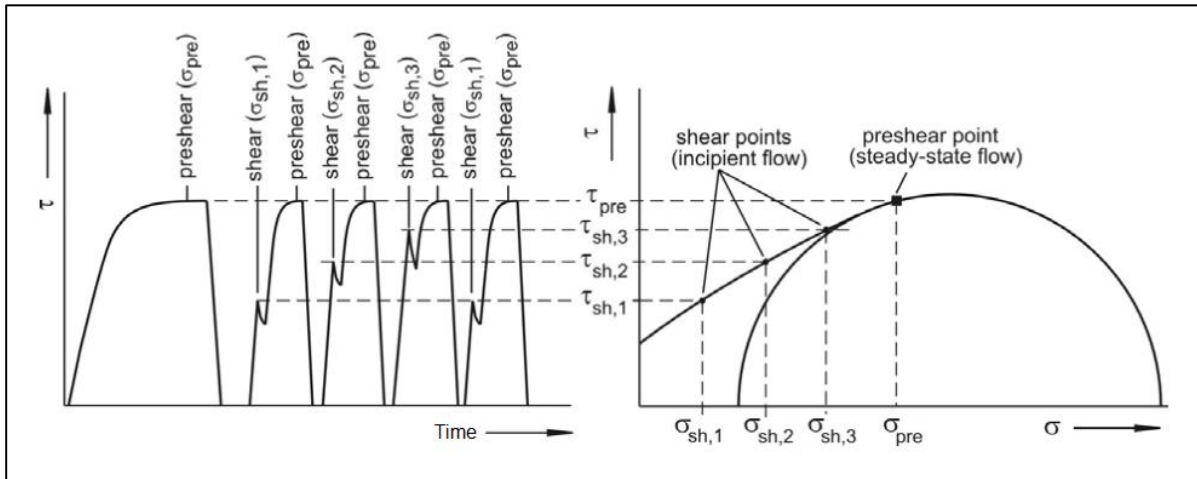
Fig. 3.13: The plot of stresses and the yield locus[188]

The flowability of the powders depended on the consolidation stresses. Within the RST test, yield loci were determined for various normal stresses consolidated under the same pre-shear load. Each yield locus represented the shear resistance for the same consolidation whilst the Mohr's circle represented all the stresses at a point in the powder mass. To construct the Mohr's circle, a fixed normal stress, σ_{pre}, was initially applied for the consolidation of the powders. During this time, the powders attained constant shear stress, ζ_{pre}, and a specific bulk density (see the left side of fig 3.13). This was the steady state flow and was termed the 'preshear'. Once this was attained, the shear stresses were returned to zero and were followed by an application of a new shear stress, σ_{sh} ($< \sigma_{pre}$). This created shear and was responsible for breaking the consolidated mass, causing particle flow. It was accompanied by a decrease in both the bulk density and ζ_{sh}. A yield locus was obtained by repeating the cycle of consolidation and shearing, from which the flow properties were determined. The flowability index was subsequently given by:

$$FF_c = \frac{consolidation\ stress}{breaking\ stress} = \frac{\sigma_1}{\sigma_c} \qquad \text{Eq. 3.5}$$

Note: The breaking stress was termed the unconfined yield stress in fig.3.13.

Table 3.5 provides the range of the FF_c and the corresponding nature of the flow.

Table 3.5: The flowability indices and the corresponding nature of the flow[187]

Flowability index, FF_c	Nature of the flow
$FF_c < 1$	Not flowing
$1 < FF_c < 2$	Very cohesive
$2 < FF_c < 4$	Cohesive
$4 < FF_c < 10$	Easy flowing
$10 < FF_c$	Free flowing

3.5.4 X-Ray Diffractometry/Diffraction (XRD)

Samples of the pure ceramic and ball milled powders and green, brown and sintered bodies were analysed for their diffraction patterns (Bruker D2 Phaser, Massachusetts, USA, Co source, λ = 0.17 nm) allowing the reactions and the phase transformations that occurred during the different heat treatments to be deduced. The approximate phase fractions were calculated based on the intensity ratios of the highest peaks of the phases. The following equation[115] was used for the calculation

$$i\ \% = \frac{height_i}{\sum height_i} * 100 \qquad \text{Eq. 3.6}$$

For the diffraction, each of the samples was scanned for 60 min each with $4^o \geq 2\theta \leq 128^o$ without any rotation.

3.5.5 Thermo Gravimetric Analysis (TGA)

TGA (Netszch STA 449C, Selb, Germany) of the polymer used to make the moulds and the binder was used to determine the mass loss in air with respect to temperature, which was, in turn, used to design the heat treatments for the mould removal and debinding stages. TGA of the sintered Syalon 050 was used as a part of the oxidation behaviour assessment. In each case, the sample size was <1 g and for the organic samples (the binder and the mould), mass loss was observed until a temperature of $600^{\circ}C$ using a rate of $10^{\circ}C$ min^{-1}, whilst for the sintered sample, mass loss was recorded until $1500^{\circ}C$.

A simultaneous differential scanning calorimetry (DSC) was also conducted. The DSC curve obtained was useful to draw conclusions regarding the reactions being exothermic/endothermic and phase transformations.

3.5.6 Computer tomography

The X-ray microtomography, X-μCT (Bruker Skyscan 1172, Massachusetts, USA), was used on the filled moulds and sintered components to determine the extent of the filling of the mould cavity and the presence of pores, cracks and other anomalies. The X-ray source was powered by 20 – 100 kV, 10 W, with a <5 μm spot size with an Al+Cu filter combination and the flatfield corrections were set to a resolution of 5 μm, the smallest pixel size. A minimum threshold of 30% of attenuation for the X rays was set for the scanning results. Three software packages were used for the analysis:

- Vertical dimension image reconstruction was achieved using NRecon software (Micro Photonics, Allentown, PA, USA).
- Porosity calculations were achieved using CTan software (Bruker, Massachusetts, USA).

- 3D visualisation of the components was achieved using CVox software (Bruker, Massachusetts, USA).

The scanning time was dependent on the size of the sample and the resolution scale.

3.5.7 Raman spectroscopy

Raman spectroscopy (inVia Qontor Confocal Raman microscope, Renishaw plc, Wotton-under-Edge, UK) was used to identify the phases in sintered samples and to examine shifts in the peaks in the patterns on the fractured surfaces of sintered samples. A shift in the peaks would indicate the presence of fabrication-induced residual stresses in the sample. The tests were conducted on samples <20 mm in size using a laser of 532 nm (He-Ne) with the laser power being varied until the best pattern was achieved. Results were collected within the range of $0 \leq \lambda \leq 4000$ cm^{-1} wavelength and a magnification of 20x was used consistently for all the measurements. No surface preparation was done to avoid affecting the stress state.

3.5.8 Surface profilometry

Topographical studies on both the mould and the resultant sintered samples were performed (Infinite Focus G5, Bruker Alicona, Leicestershire, UK) to quantify their surface roughness and profiles. Measurements were made at 20x magnification. For the moulds, the surface roughness was also measured as a function of slice thickness and with/without the interfacial material used to prevent absorption of the molten mould material by capillary action during mould removal stage.

3.5.9 Microscopy

A regular, benchtop optical microscope was used to visually examine the quality of the surfaces of the sintered components, before and after polishing, by looking for pores and scratches.

Extensive microstructural studies were conducted on both the sintered and subsequently oxidised samples using scanning electron microscopy (SEM) (Quanta 3D FEG Dual Beam microscope, FEI, High Wycombe, UK). The presence of different phases, grain orientations, grain sizes and the extent of oxidation were all areas of interest. The samples were cut transversely using a diamond coated circular blade and then mounted in conductive bakelite resin with the cross-sectioned area exposed on one side of the mounting. Buehler's SiC abrasive grinding papers from grade 80 to 3200 were used for initial polishing and the process concluded by using colloidal silica to achieve a mirror finish. The polished samples were then sputtered with gold for 3 min (SC 500, Emscope, East Sussex, UK) to achieve a 10 – 12 μm thick coating. Secondary electron (8 – 10 kV) and back scattered electron (20 kV) imaging were used to investigate the microstructures of the samples, the latter yielding a good contrast between the different phases. Additionally, Energy Dispersive X-ray Spectrocopy, EDS (Inca – Oxford Instruments, Abingdon, UK) was used to determine the elemental distribution within the phases the oxidized samples (see section 3.5.13).

3.5.10 Compression strength testing

This was conducted according to ASTM D695 (compression tests for rigid plastics) on the mould material on the Bluehill 5507 machine (Instron, Buckinghamshire, UK) to assess its strength to see if it would be adequate for uniaxial pressing. Six samples were additively

manufactured, without any support material, in the shape of solid cylinders having a diameter of 12.7 mm and length 25.4 mm.

3.5.11 Hardness

Microhardness measurements using a diamond indenter and 10 kgf for 10 s were conducted on both polished outer and cut internal surfaces of sintered ceramic samples (5030 SKU Vickers hardness Identec machine, Brierley Hill, UK); sample preparation followed that described in section 3.5.8. The lengths of the diagonal from the indentation were measured using an in-situ scale and were input into the machine, which then instantly calculated the HV_{10} hardness.

3.5.12 Flexural strength testing

Sintered bar samples measuring 28 x 5 x 3 mm[‡‡‡] were fabricated according to the process described in section 3.2 and then subjected to 3 point flexural testing (Instron 4467, Instron, High Wycombe, UK). Note that due to the size of the samples, some cracking and warping was encountered due to thermal stresses that occurred during the sintering process. The best samples were selected for testing and a uniform loading rate of 0.2 $mmmin^{-1}$ was applied. A total of nine samples were tested and the approximate flexural strength calculated using the following equation[§§§]:

$$\sigma_f = \frac{3FL}{bd^2}$$
Eq. 3.7

[‡‡‡] ASTM C1161 could not be followed due to the lack of suitable equipment for pressing the green bars.
[§§§] National Physical Laboratory - Flexural strength testing of ceramics and hardmetals

3.5.13 Oxidation studies

A series of oxidation tests were carried out on the sintered Syalon 050 to investigate the behaviour and oxidation resistance at temperatures >1000°C. Samples were fabricated according to the process outlined in section 3.2 and oxidation took place in a muffle furnace in an air atmosphere using the conditions outlined in Table 3.6. The heating rate was 5°C min^{-1} for all the tests.

Table 3.6: Oxidation tests undertaken on samples of sintered Syalon 050

Temperature / °C	Duration / h
1250	24
	48
	72
1350	24
	48
	72
1450	24
	48
	72

The masses of the samples before and after oxidation were measured and recorded. The samples oxidised at 1450°C were analysed using the SEM and EDS was also conducted to examine to the extent of the oxygen diffusion in the samples along with the final elemental distribution. Based on the weight loss of the samples after oxidation, the parabolic rate constant[4] was calculated according to the following formula given in eq. 2.5:

$$\left(\frac{\Delta w}{A_o}\right)^2 = K_p t + B$$

where, Δw is the weight loss, A_o is the area of cross section through which the reactant diffuses, K_p is the rate constant, t is the temperature and B is a constant. Combined with the

XRD data, the microscopy results were used to determine both the nature of the phases formed and their kinetics during the oxidation heat treatments.

CHAPTER 4

RESULTS AND DISCUSSION

This chapter consists of all the results and the corresponding discussion from chapter 3 and is divided into four sections. The first three sections contain the results and discussion on the qualitative and quantitative analysis of the following:

a. The moulds

b. The ceramic Syalon 050 powders

c. The sintered bodies.

The final section contains the discussion on the oxidation studies conducted on the sintered Syalon 050 components.

4.1 Additive manufacturing

4.1.1 Additively manufactured moulds and the parts produced

Several printing operations took place to additively manufacture positive and negative moulds for the ceramic fabrication. The printing process concluded by the removal of the consumable platform from the AM unit. It was then heated to 125°C to melt the support material layers underneath the printed component. This action helped to detach the components from the platform. These components were then subjected to ultrasonication in the dewaxing oil provided by Solidscape Inc. After the dissolution of the support material in the oil, the moulds were taken out and were ready to be used in the ceramic fabrication

process. Fig. 4.1 shows some of the additively manufactured moulds of different aspect ratios.
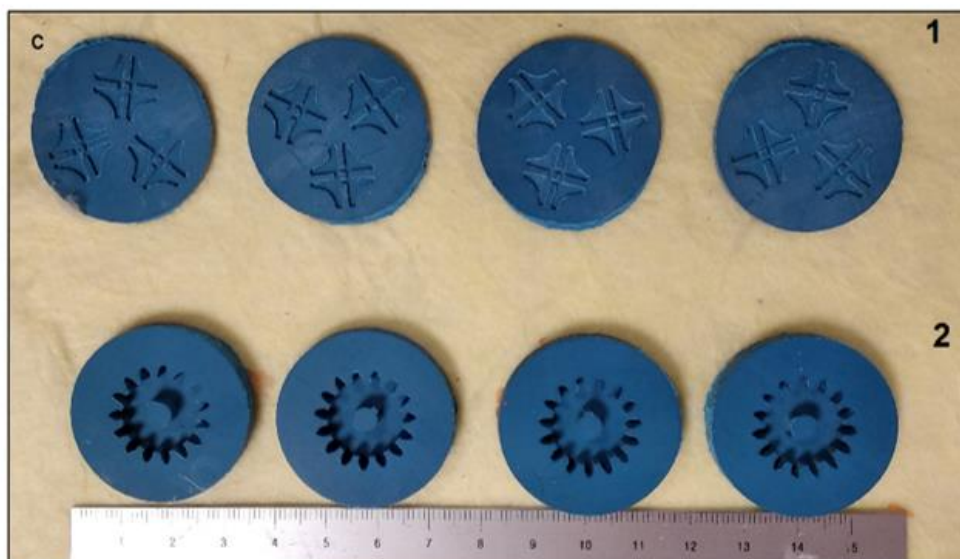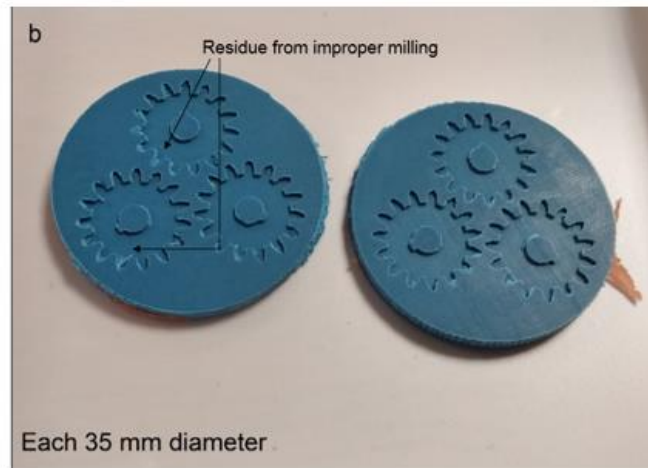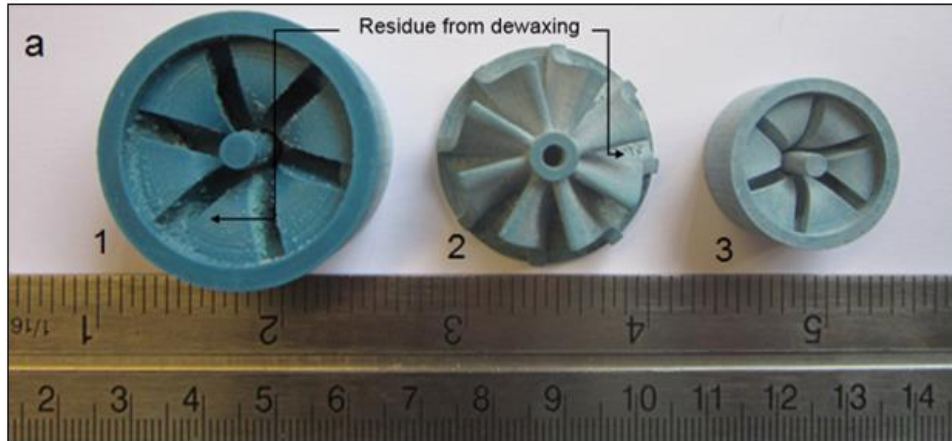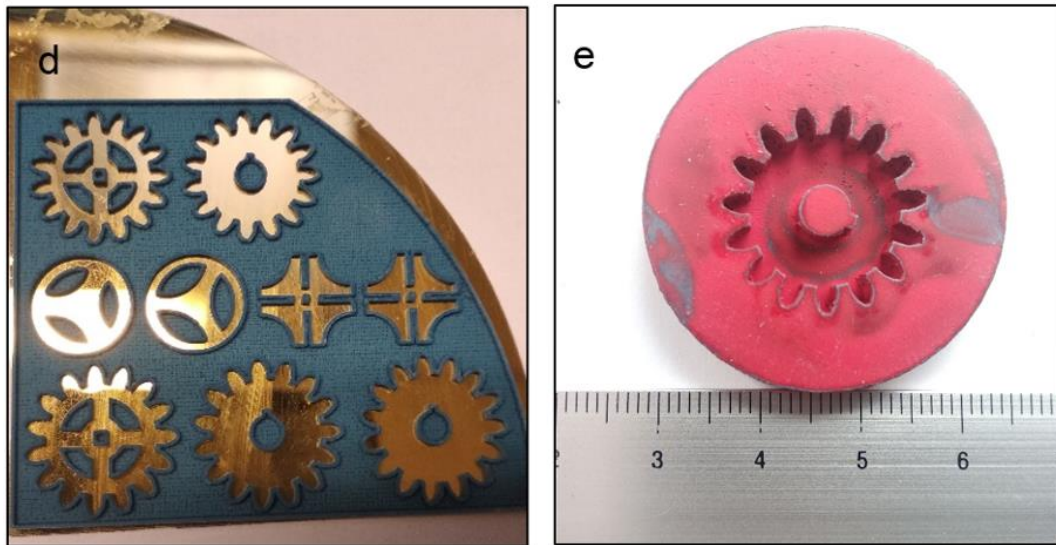
Fig. 4.1: Some examples of the additively manufactured moulds, a. 1. negative of a turbocharger, 35 mm dia, 2. positive of a turbocharger, 30 mm dia, 3. negative of a turbocharger, 26 mm dia; b. lower aspect ratio engineering components, 35 mm dia disks, c. 1. lower aspect ratio components, 2. higher aspect ratio components; d. AM on Au plated Si wafer for electroforming of Ni components, 35 mm wafer quarter; e. a mould with the interfacial material sprayed on

The examples in fig. 4.1 include moulds for turbocharger rotors of different diameters, engineering gears of different thicknesses and an example of substrate printing for electroforming. For components with spacial features in three dimensions (such as the turbocharger rotor), a negative mould was printed to obtain the actual component. Other than the mould in fig. 4.1.d, all the moulds were made of 38 µm slice thickness and had two layers of support material. The printing shown in d was on Au coated Si wafer, made up of a slice thickness of 6 µm, without any support material. These moulds were subjected to Ni electroforming for fabricating micro-scale parts, which was an attempt to exploit the potential of the AM unit used.

Initially, some residue was observed in some of the parts as seen the fig. 4.1a. One reason for this could be because the dewaxing oil became saturated with support material from previous ultrasonication operations, whilst an alternative could be that insufficient time was

employed for the removal of the support material. The presence of the residue is a hindrance to getting good components since the improper filling of the moulds could lead to bad finishing and poor density. Hence, for cleaner moulds, measures such as constant replacement of the dewaxing oil and slightly longer ultrasonication periods were taken up. This resulted in cleaner moulds with a residue-free cavity in the mould design. Also, on many occasions, flakes from the mould were noticed on the edges of some of the intricate features, e.g. see fig. 4.1b. This was due to trapped flakes within the cavity and the vacuum system not conducting the suction operation efficiently after the milling operation. The presence of flakes affected the fabrication in the same manner as the residue. Unfortunately, this problem remained throughout since detaching or replacing the vacuum system wasn't an option due to the technical specifications of the AM unit. Once the moulds were detached from the platform, they were gently tapped and dusted off. This ensured the complete removal of the flakes before the final use. Moulds as high / thick as 25 mm could be printed, see fig. 4.1c, top image. The last image in fig. 4.1e shows a mould with the (red) heat resistant interfacial material sprayed on.

4.1.2 Effect of the slice thickness in the AM parts

Fig. 4.2 illustrates the end printed products of an intricate design made up of three different slice thicknesses of 38, 19 and 6 µm.
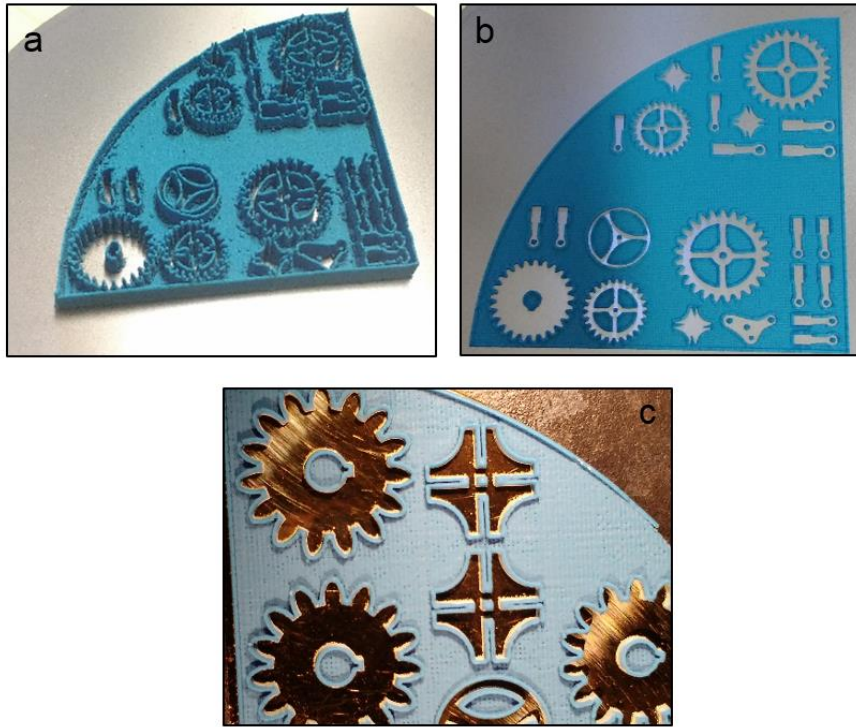
Fig. 4.2: Evolution in the sharpness of the features (printed for electroforming Ni components with varied thickness) as the slice thickness is reduced, a. 38 µm; b. 19 µm; c. 6 µm

The designs depicted in fig. 4.2 were intended as moulds for Ni electroforming for microscale applications. Therefore, the application demanded fine details and high resolution. Initially, the design was printed with a slice thickness of 38 µm, as shown in fig 4.2a. From the image, it was concluded that the design lacked resolution and mechanical strength in the vertical direction (height). This was followed by a second printing with a slice thickness of 19 µm, as shown in the fig. 4.2b. The design improved markedly with respect to its resolution. Upon reducing the slice thickness further to the lowest minimum i.e., 6 µm, the best resolution was obtained. A stark difference among the designs can be seen. Therefore, for the electroforming application, the slice thickness was set to 6 µm and a slice thickness of 38 µm was selected for all other designs throughout the study.

When the visual appearance of the component is the main concern, a selection of low slice thickness is ideal since it results in a smooth finish. Additive manufacturing of intricate designs vs. bulk shapes can be understood by the illustration in fig. 4.3.
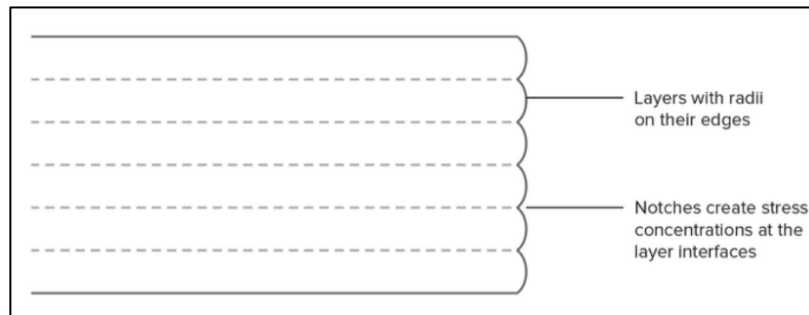
Fig. 4.3: Schematic of the layer by layer construction of a 3D printed part[****]

Intricate designs produced from high slice thickness formed bulges on the edges with radii. These sequential layers create notches, which not only act as stress concentrators but also increase the surface roughness of the component leading to the deterioration of mechanical properties and surface smoothness[148].

On the other hand, a similar investigation was done by printing less intricate shaped moulds (turbocharger rotors of 14 and 17 mm height). The results are shown in the fig. 4.4. Although employing a low slice thickness didn't make a significant difference to simple-shaped components from a purely visual perspective, however, a longer time was taken to print the component and a higher volume of the material was consumed. This would increase the overall production costs. Therefore, to additively manufacture less intricate designs, high slice thickness is recommended.

[****] www.3dhubs.com

Fig. 4.4: Photograph showing turbocharger printed of different slice thicknesses

4.1.3 Effect of the interface material on the mould

As discussed in section 3.3.2, the finishing of the green body is dependent on the surface quality of the mould. Powder components compacted within the mould without the interfacial material sprayed on gave a poor surface finishing. The latter is attributed to the capillary action of the powder compacts, due to which the molten material started to seep into the powder compacts. Section 3.4.3 described the interfacial material that was sprayed on the moulds to reduce/inhibit the capillary action. Fig. 4.5 illustrates two green bodies, one made without the interface and one made with the interfacial sprayed mould.
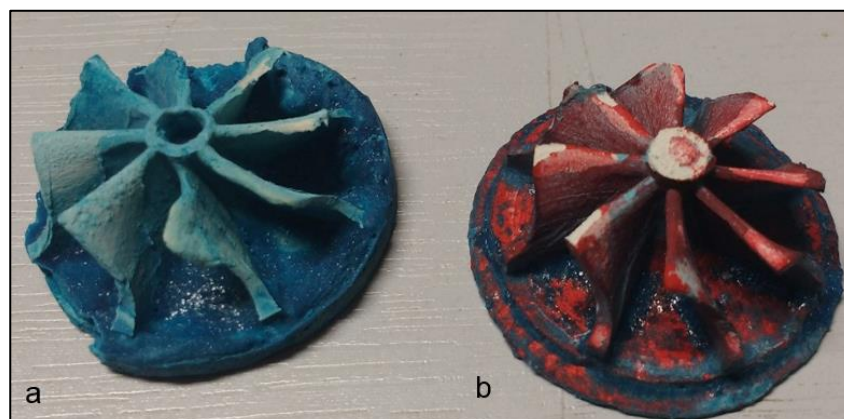
Fig. 4.5: Complex shaped turbocharger green bodies (35 mm dia), a. without the interfacial material; b. with the interfacial material

A stark difference can be seen between the two green bodies in fig 4.5. Although the green body with the interface is not flawless, a significant improvement in the finish and better shape retention can be seen compared to the one fabricated without the interfacial material. The residual red colouration on the green body suggests that it is providing an efficient barrier between the mould and the compact. The blue remains are from the mould material that didn't absorb into the powder bed during the removal stage; the same image also confirms that the molten material wasn't absorbed by the powder compact either. Further to this qualitative analysis, a study was conducted on the quantification of the influence of the interface on the mould in terms of surface roughness. Surface roughness values were measured on two moulds, one without the interface and the other with the interface layer. Readings obtained were compared with each other to understand the interface's potential influence on the finishing of the green body and the sintered components. Measurements were made on a gear mould and fig. 4.6 indicates the locations these measurements were made.
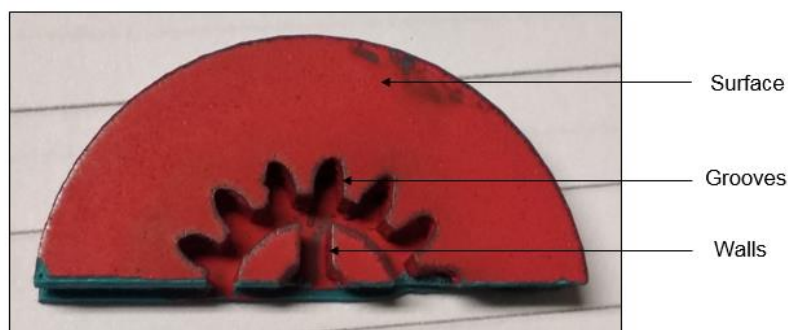
Fig. 4.6: A labelled photograph of an AM mould (dia. 35 mm with interfacial) pointing the locations of the surface roughness measurements

The surface roughness readings were coupled with one more parameter that affected the quality of the green body – the slice thickness used for the AM of the moulds. Eventually, a comparison study was conducted between non-interfacial and interfacial moulds with

different slice thicknesses in the AM moulds. Table 4.1 is an overview of the readings of the surface roughness (R_a) obtained at the locations as highlighted in fig. 4.6, with a comparison being made between the non-interfacial and interfacial surfaces, across the three different slice thicknesses (6, 19 and 38 µm).

Table 4.1: Readings of surface roughness measured between the non-interfacial and interfacial mould surfaces

Slice thickness / µm	Location of the measurement	Non-interface R_a / µm	Interface R_a / µm
6	Wall	2.7	8.6
	Groove	9.4	2.7
	Surface	1.2	1.7
19	Wall	1.4	2.5
	Groove	1.6	2.4
	Surface	1.1	1.8
38	Wall	1.3	0.9
	Groove	0.9	2.7
	Surface	0.9	1.2

The set of images in fig 4.7 - 4.15 illustrate the readings in table 4.1 in terms of 3D constructed surfaces and show the height profiles. The depiction in the case of the interfacial mould surface is a function of the amount and uniformity of the interfacial spray applied. Though the top of the mould surfaces was observed to be smoother than the interfacial counterparts, a wavy pattern was often observed. This depicts the working direction of the helical cutter after the milling operation on the last layer of the mould. As discussed in the previous section, the lower the slice thickness employed, the longer the time taken to finish the printing job. In contrast, some of the locations, such as the inner grooves on the 6 µm slice thickness (non-interfacial), exhibited high surface irregularity compared to the other areas. These areas, when applied with the interfacial spray, were found to become smoother due to the irregularities being filled in.

Note: In fig. 4.7- 4.15, the scale is different for every image.
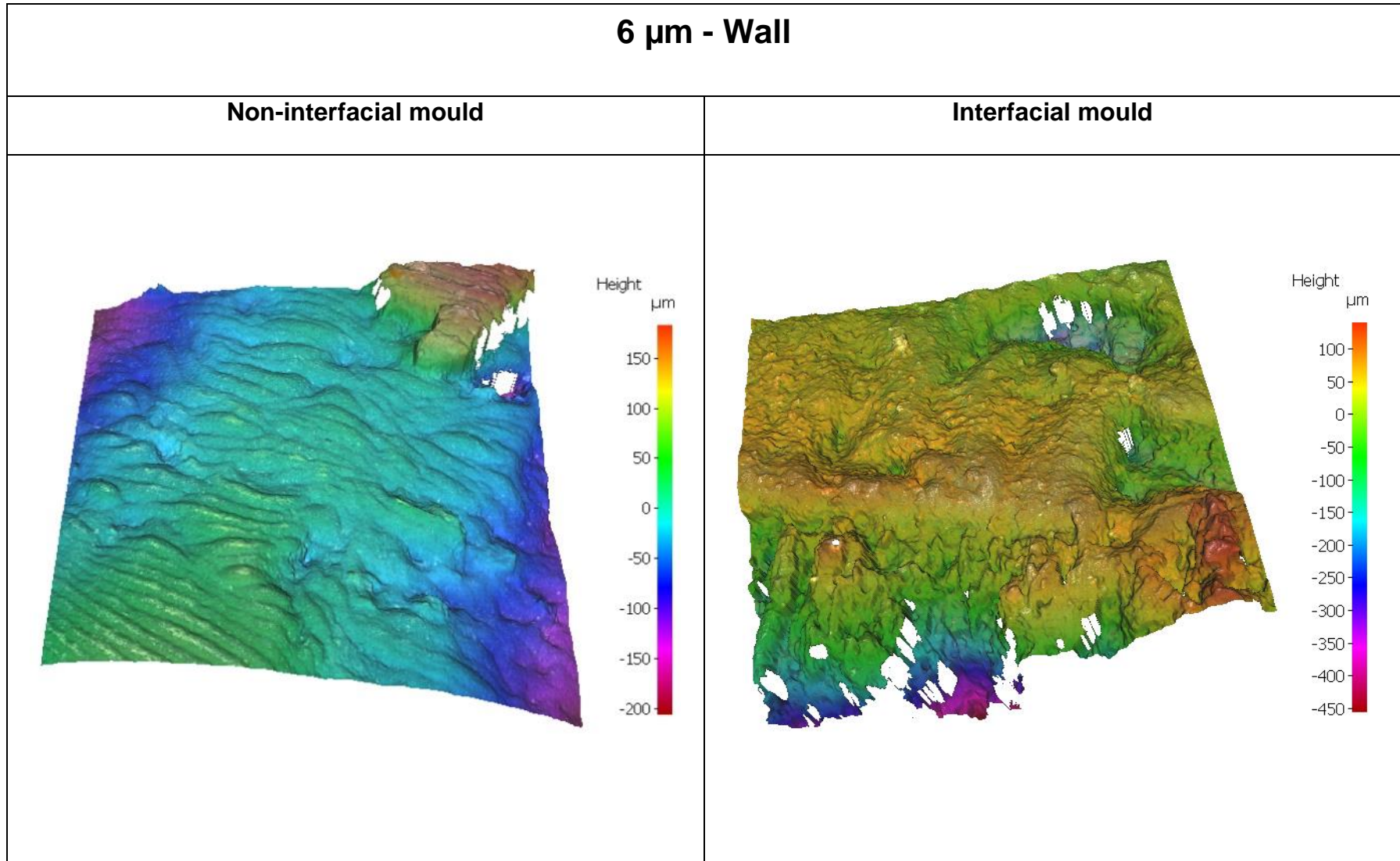
Fig. 4.7: A 3D reconstruction of the surface roughness of the 6 µm-wall surface of a non-interfacial and interfacial mould

6 µm - Groove	
Non-interfacial mould	**Interfacial mould**
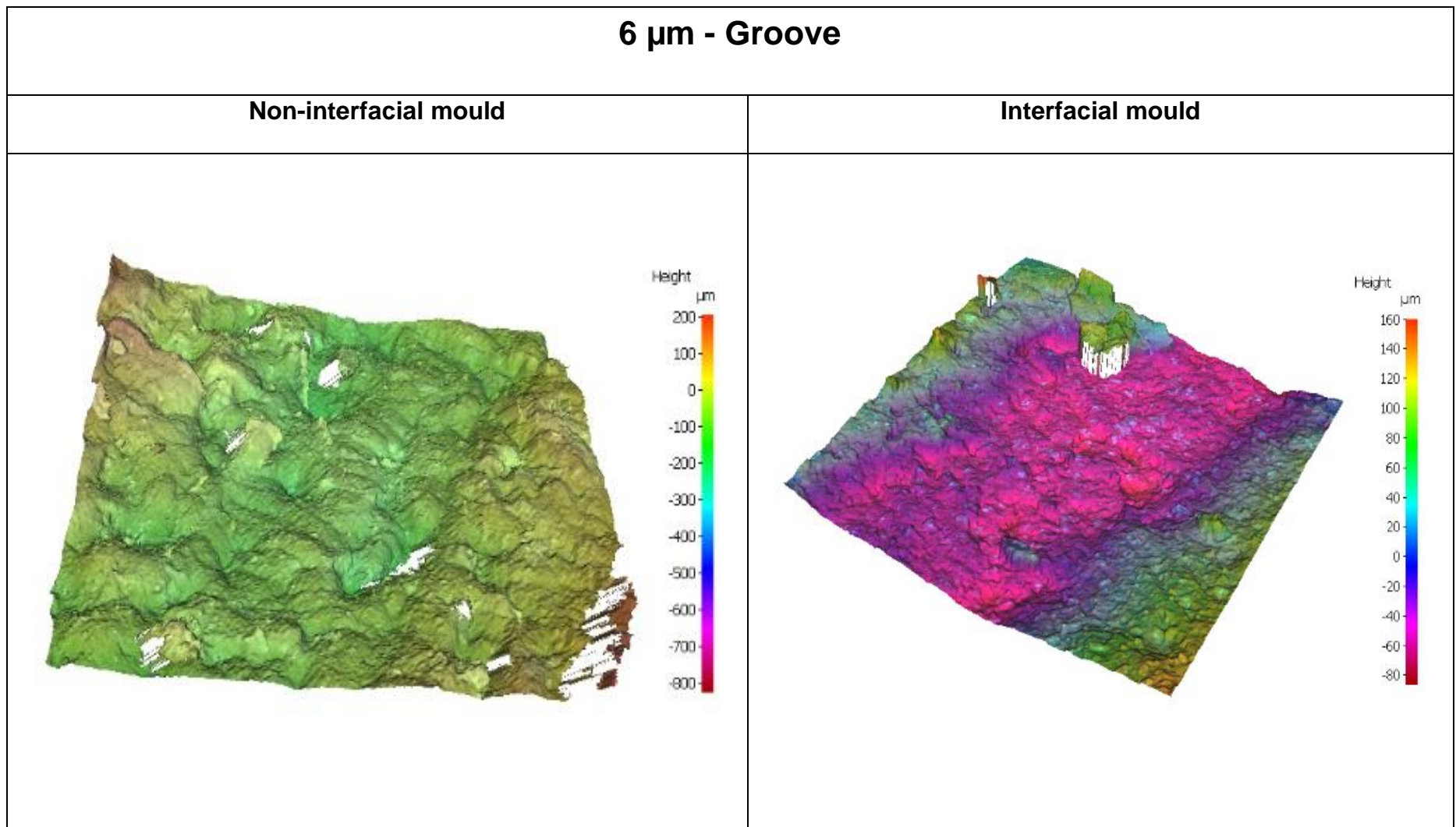
Fig. 4.8: A 3D reconstruction of the surface roughness of the 6 µm-groove surface of a non-interfacial and interfacial mould

6 μm - Top surface

Non-interfacial mould	Interfacial mould
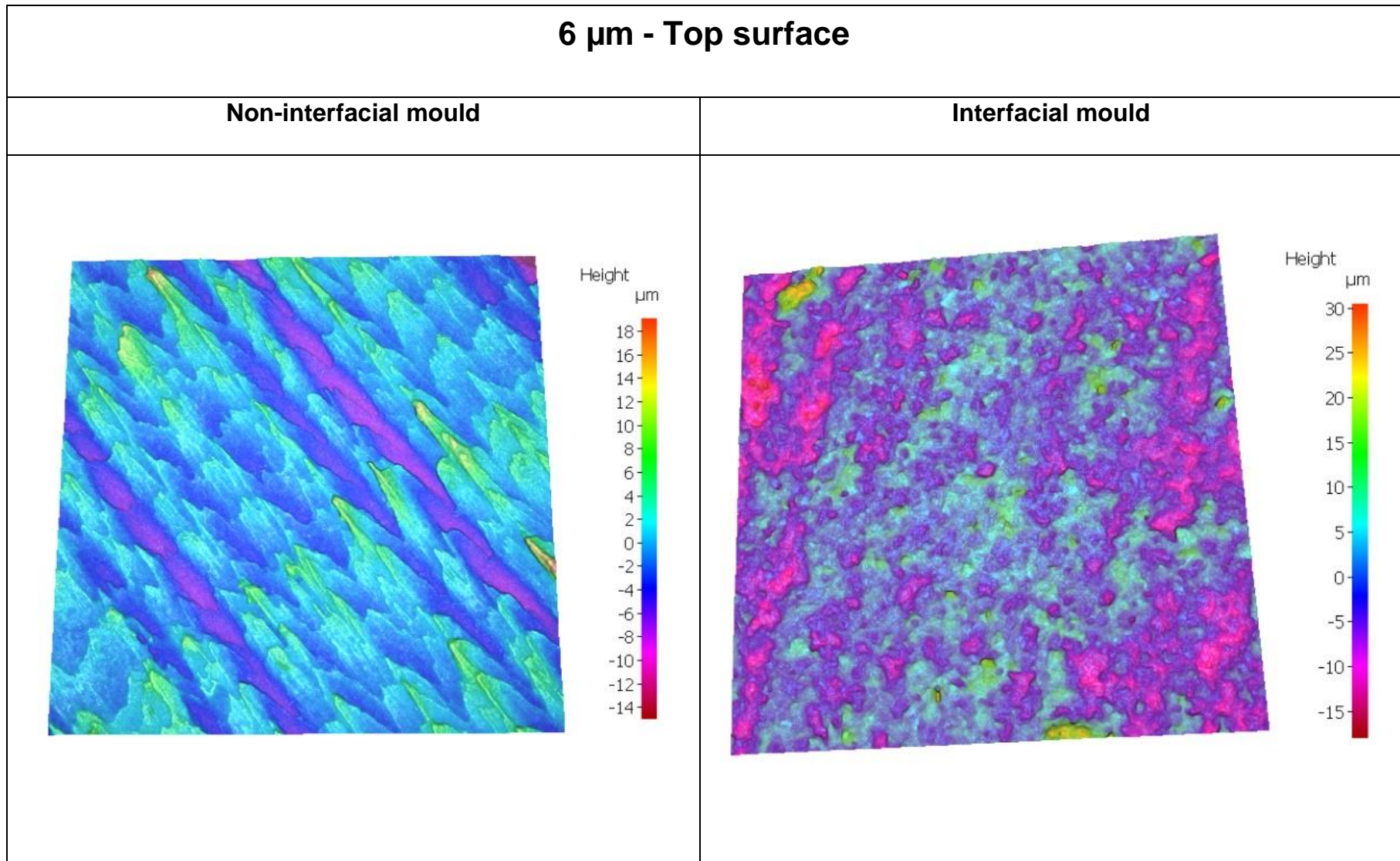
Fig. 4.9: A 3D reconstruction of the surface roughness of the 6 μm-top surface of a non-interfacial and interfacial mould

114
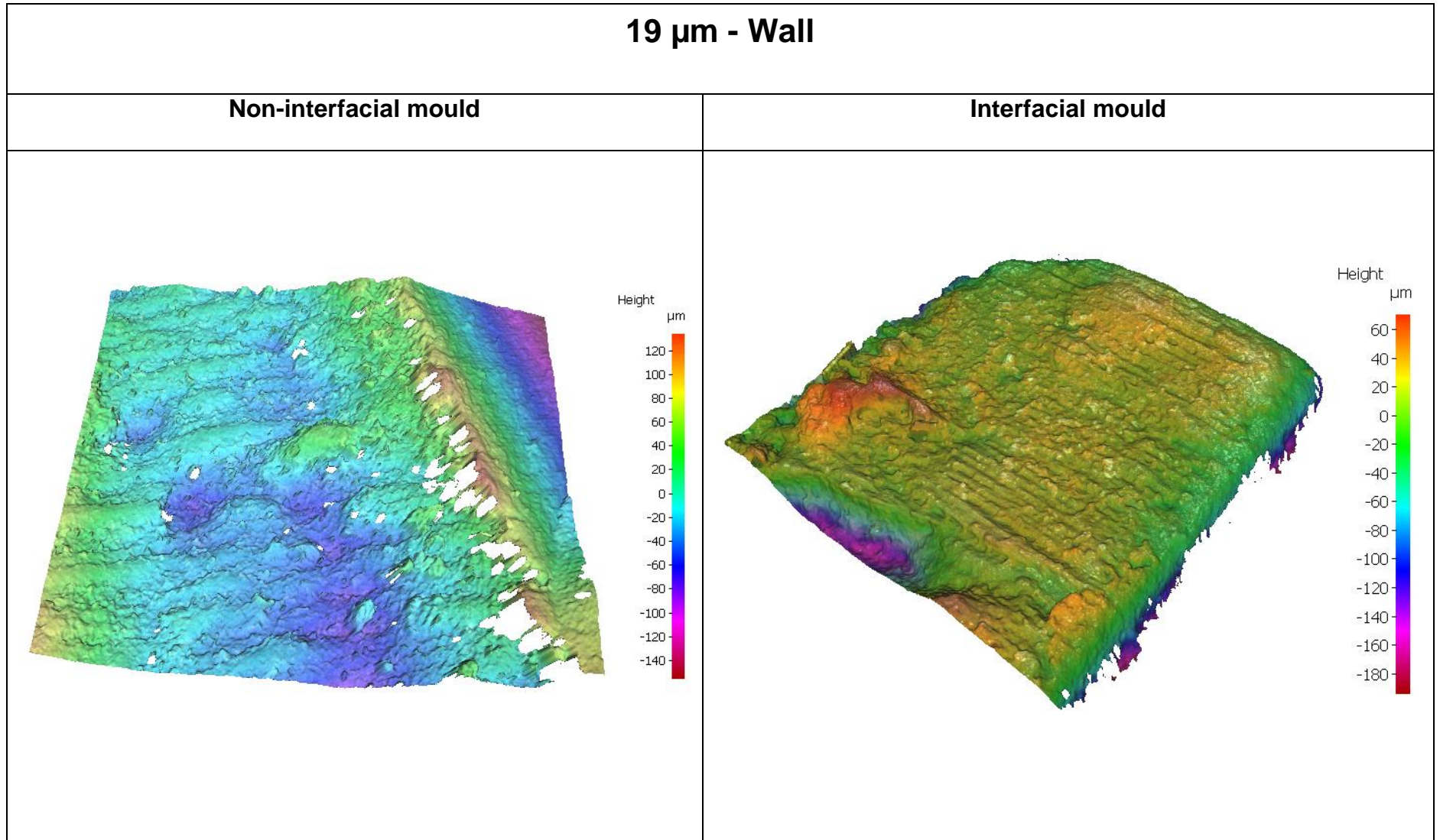
Fig. 4.10: A 3D reconstruction of the surface roughness of the 19 µm-wall surface of a non-interfacial and interfacial mould

Fig. 4.11: A 3D reconstruction of the surface roughness of the 19 µm-groove surface of a non-interfacial and interfacial mould

19 µm – Top surface
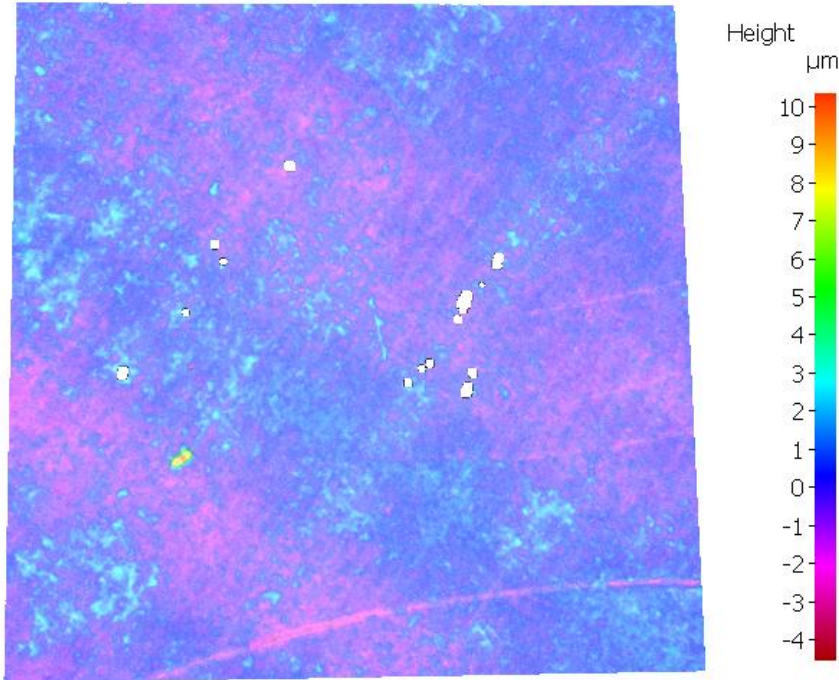
Non-interfacial mould	Interfacial mould
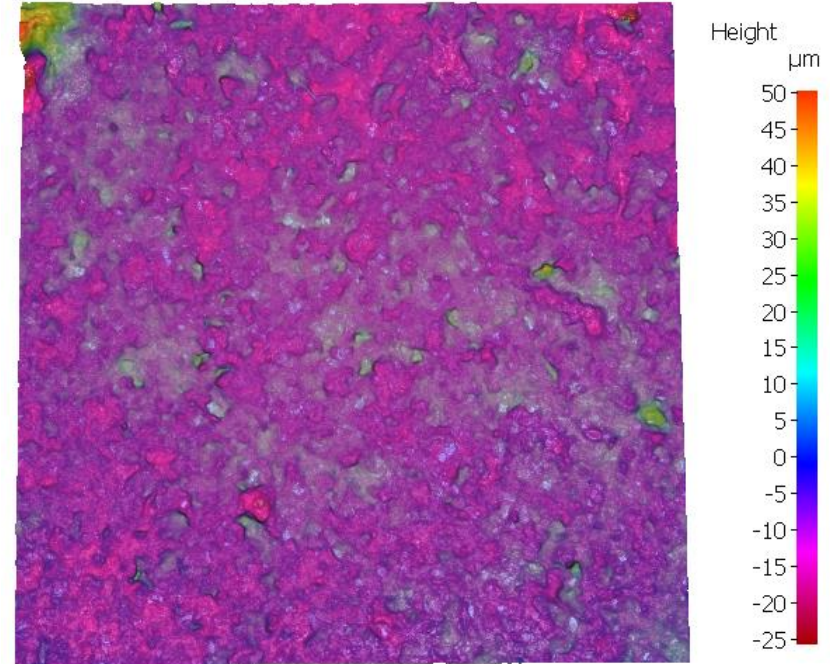
Fig. 4.12: A 3D reconstruction of the surface roughness of the 19 µm-top surface of a non-interfacial and interfacial mould
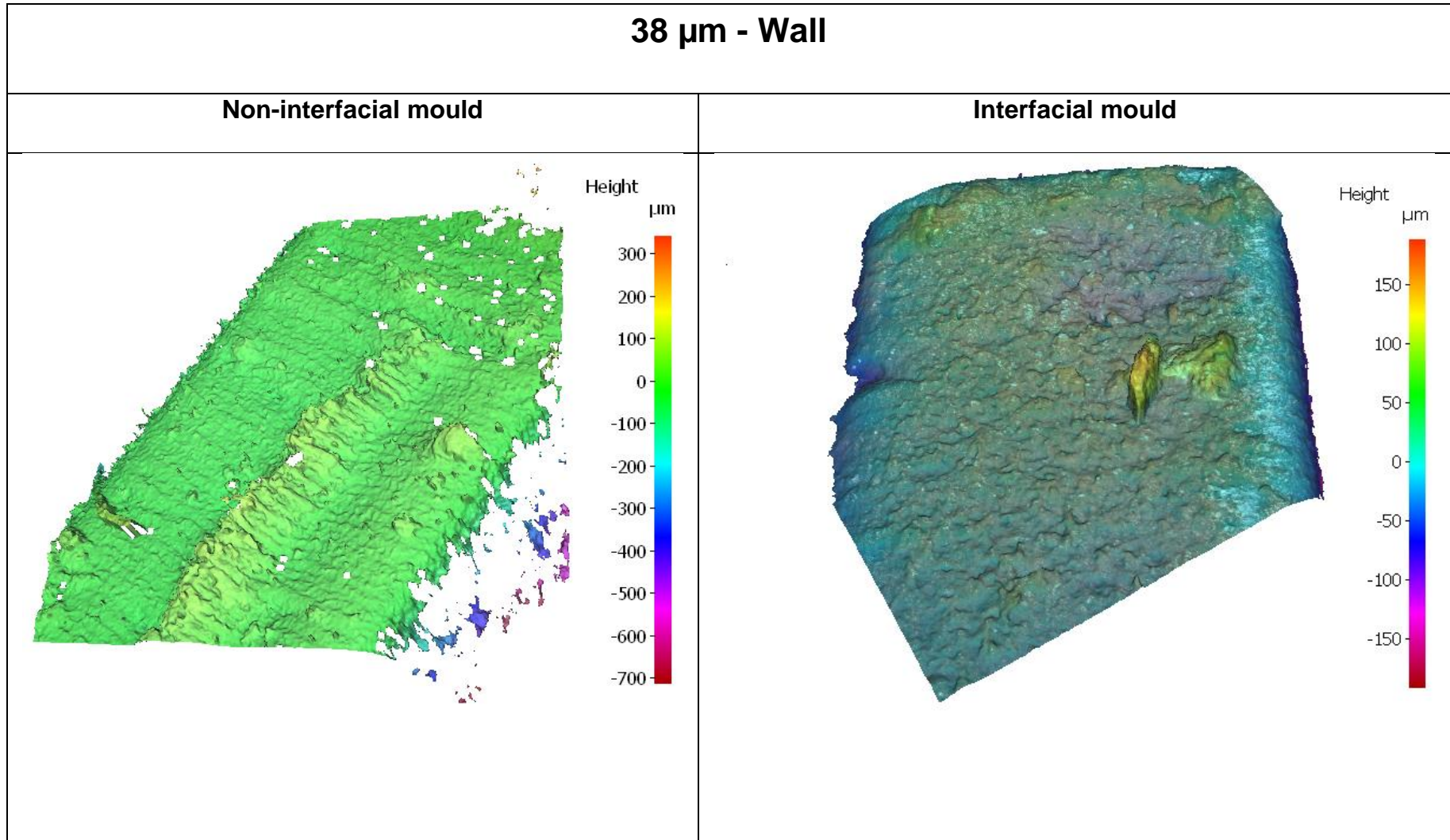
Fig. 4.13: A 3D reconstruction of the surface roughness of the 38 µm-wall surface of a non-interfacial and interfacial mould
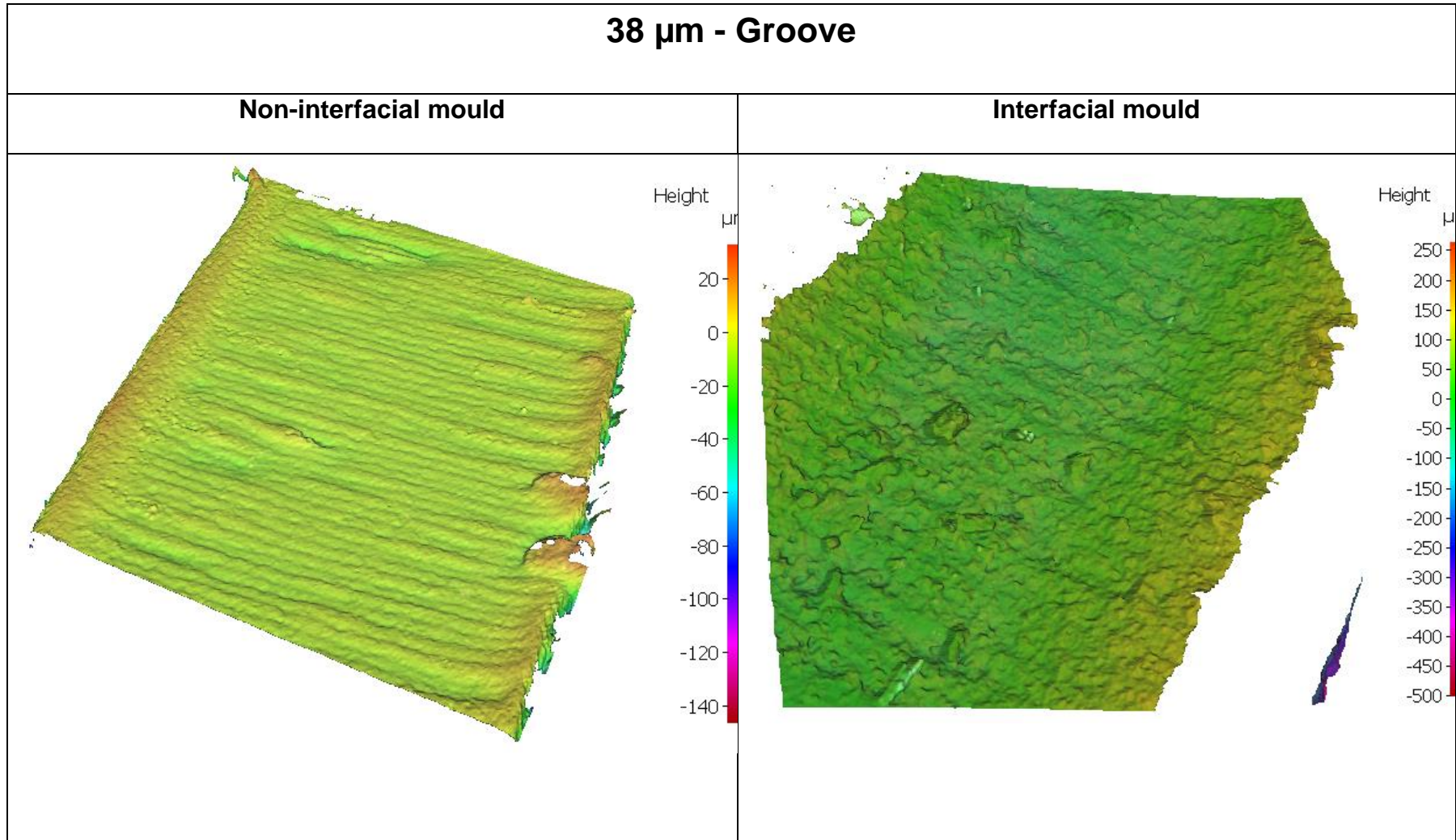
Fig. 4.14: A 3D reconstruction of the surface roughness of the 38 µm-groove surface of a non-interfacial and interfacial mould
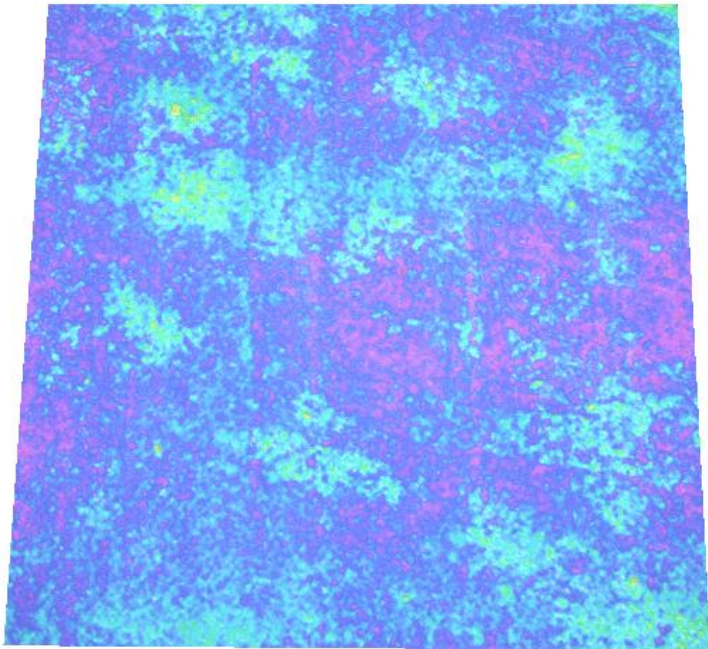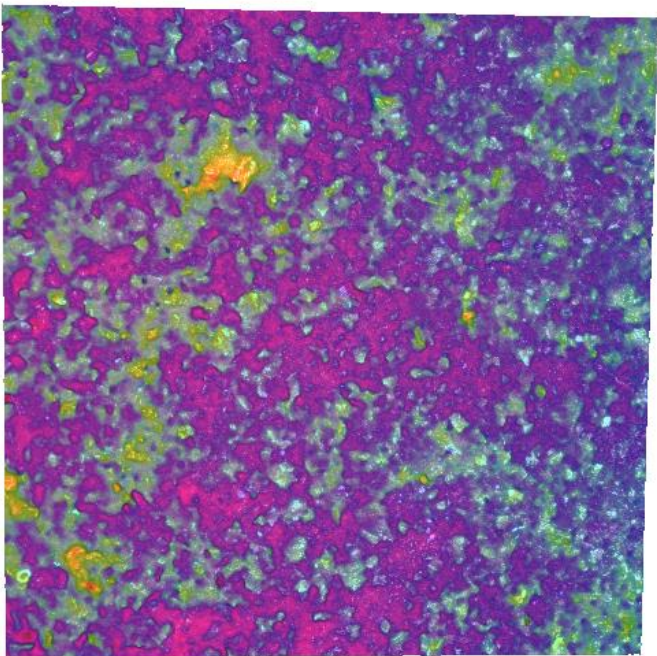
Fig. 4.15: A 3D reconstruction of the surface roughness of the 38 μm-top surface of a non-interfacial and interfacial mould

4.1.4 The compression strength of the AM moulds

A total of 5 samples were subjected to the compression test and the average compression strength was calculated to be 87 N.
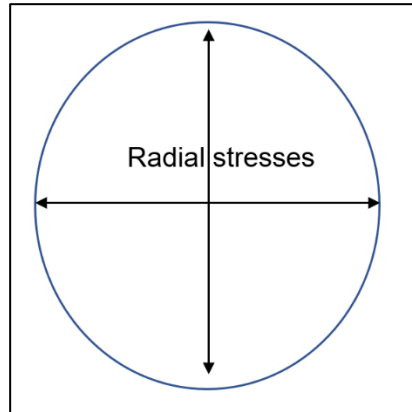
Fig. 4.16: Directional movement of the radial stresses in uniaxial compaction

The compression strength is slightly lower than the compaction force optimised for the uniaxial compaction of the powder, i.e. 98 N. However, non-failure of the mould after the compaction could be contributed to the presence of the encasement of the mould within the cylindrical housing of the die. This housing could be responsible for absorbing some of the radial stresses transferred from the powders and the mould. A schematic of the direction of the radial stresses is shown in fig. 4.16. Though absolutely no damage was seen in case of moulds with significant x-y plane features, e.g. engineering gears of thickness ~1.5 mm, minor and rarely major damage was observed in the moulds with an aspect ratio less than ~1.75, e.g. the negative of the turbocharger mould, which had a height 20 mm or more. Minor damage included chipped edges of the mould after compaction. This was not observed to influence the compact in any way. On the other hand, owing to the induced anisotropy in the z-direction, major failures included complete breakage of the mould in the transverse plane after compaction. This could be attributed to the radial stresses acting on

the thinner parts (such as the area between adjacent blades) coupled with the inability of the mould to withstand the stresses. However, this failure was only observed occasionally.

4.1.5 Thermogravimetry analysis

A simultaneous TGA, DSC and the DTG analysis was performed on the mould material at a rate of 10°C/min until a temperature of 600°C was reached; the resulting data is shown in fig. 4.17 below.
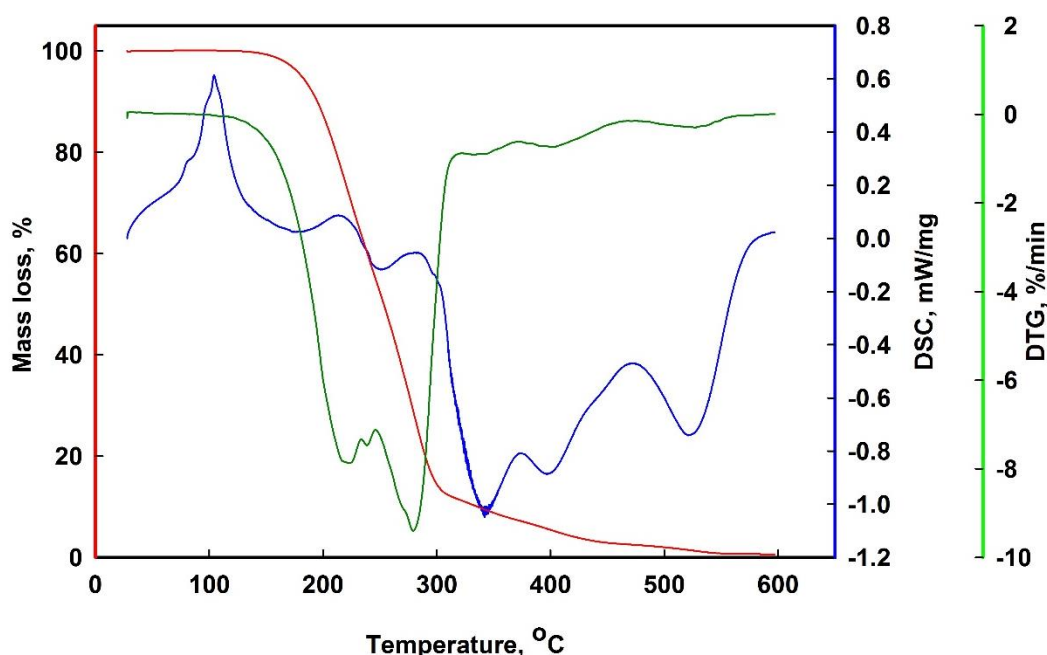
Fig. 4.17: Thermal analysis of the mould material

The TGA data exhibits a drop in the curve after ~120°C and the mass loss is observed to occur until the end of the test. The evolution of moisture, CO and CO_2 in the form of gases is probably the primary reason for this mass loss[189]. From the known components of the mould's material, mass loss can also be contributed to SO_2, hydrides and oxides of nitrogen[190,191].

An exothermic reaction is indicated by a peak in the curve of the DSC measurement at approx. 100°C. Polymers are known to exhibit curing or crystallisation processes just below

their melting point and are exothermic in nature. Therefore, this peak can be concluded as a representation of the same. This fact could be confirmed if the complete composition of the polymer was known. Two endothermic reactions depicted by a fall in the curve at ~350°C and beyond 500°C can be attributed to the evolution of sulphur-based and carbon oxide gases respectively.

4.1.6 Melting of the mould

To obtain a green body without any cracks, different heating rates in the range of 3°C/min to 0.2°C/min were employed and the resulting quality was investigated. The higher heating rates, such as 3°C/min, led to the formation of several cracks and increased capillary action in areas that happened to have a less interfacial coating. As the heating rate was reduced, the number of cracks decreased. The heating rate of 0.2°C/min resulted in the best green bodies, with no visible capillary action of the powder compact and no visible cracks. Additionally, if the powder bed was found to be saturated with the molten mould material, it was swiftly replaced. This ensured that the green bodies did not get exposed to the ambient temperature and pressure for a long time to avoid thermally induced stresses and potential cracks.

Therefore, a heating rate of 0.2°C/min was employed until a temperature of 150°C was reached. Although slow, this melted most of the mould material and helped to separate the green body. Fig. 4.18 illustrates some of the green bodies obtained after subjecting it to the best heat treatment.
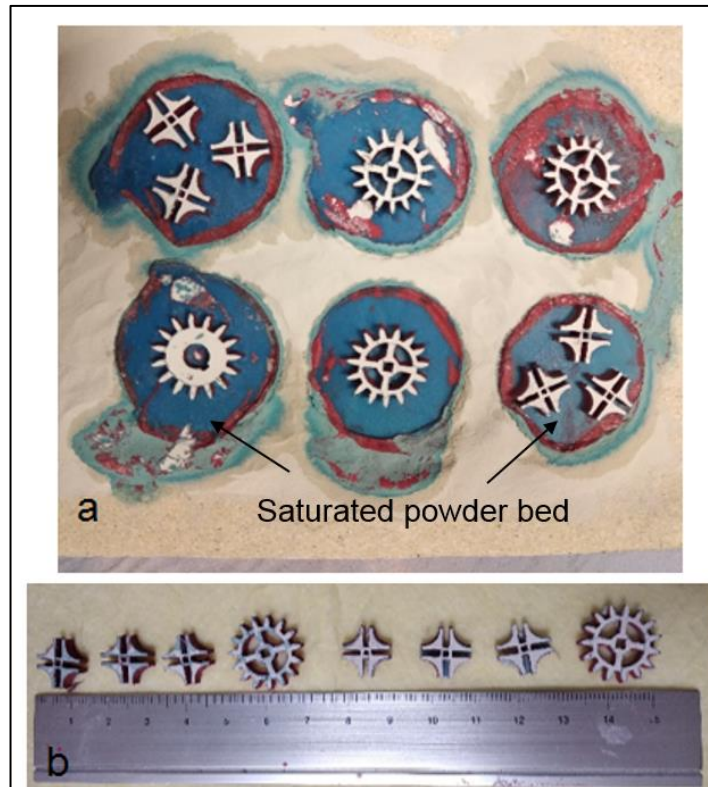
Fig. 4.18: Photographs of the green bodies, a. on the powder bed just after the mould removal heat treatment; b. green bodies removed from the powder bed

From fig. 4.18, both red and blue colouration can be seen on the green bodies; this is due to the residual presence of both the interfacial material (red) and the mould walls (blue) respectively. Fig. 4.17 suggests the onset of degradation of the mould material to be around 180°C. Although the interfacial material is heat resistant until 800°C, the red colour is known to degrade beyond ~300°C[††††]. A longer dwelling time could be employed to remove the mould material completely from the green body, it is not recommended since it caused the molten material to be absorbed into the powder compact wherever the interfacial material was missing. This was especially true for the fabrication of the turbocharger rotors where the top of the filled mould (base of the actual component, the mould being negative) was placed upside down on the powder bed to maintain the structural stability. To maintain

---

[††††] Information obtained from the manufacturer

consistency in the fabrication process, longer dwelling periods were not practised for other geometries. Hence, approximately 85-90% of mould removal was performed. The remainder of the mould material and the interfacial material was removed in the subsequent heat treatments.

The green bodies were critically examined for flaws such as surface cracks, voids due to improper filling and pores. This examination allowed unsatisfactory green bodies to be discarded since there was no way to heal the cracks or fill the pores in the processes that followed.

4.2 Ceramic Syalon 050 powders

4.2.1 Particle size analysis
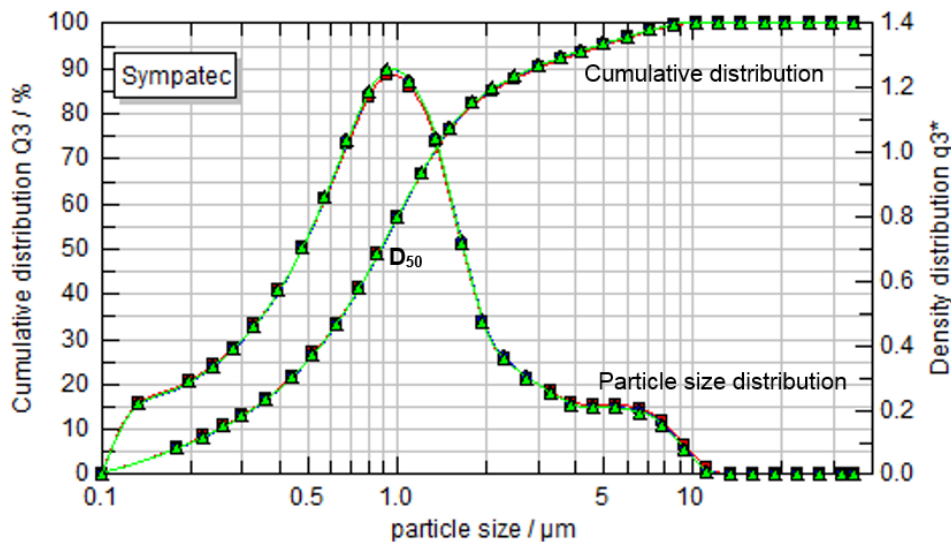
Fig. 4.19: Particle size analysis of the as-received Syalon 050 powders

The graph in the fig. 4.19 consists of two plots. Gaussian cumulative distribution of the particles is a curve drawn to draw a relationship between the cumulative distribution (the per

cent of the particles below that micron size) and the particle size. At an optical concentration of 17.7%, approximately 90% of the particles measured 0.89 µm, which is the median size of the particles measured, i.e. the D_{50}. The particle size distribution curve (bell shaped) exhibits small peaks in the range of 6 – 10 µm; these can be assumed to be agglomerates that weren't broken during the ultrasonication. The plot ends asymptomatically at 10 µm, which confirms no particles ≥10 µm existed within the sample tested.

4.2.2 X - Ray diffraction studies

The as-received powders were subjected to X-ray diffraction to investigate the phases present; fig. 4. 20 shows the diffraction pattern obtained.
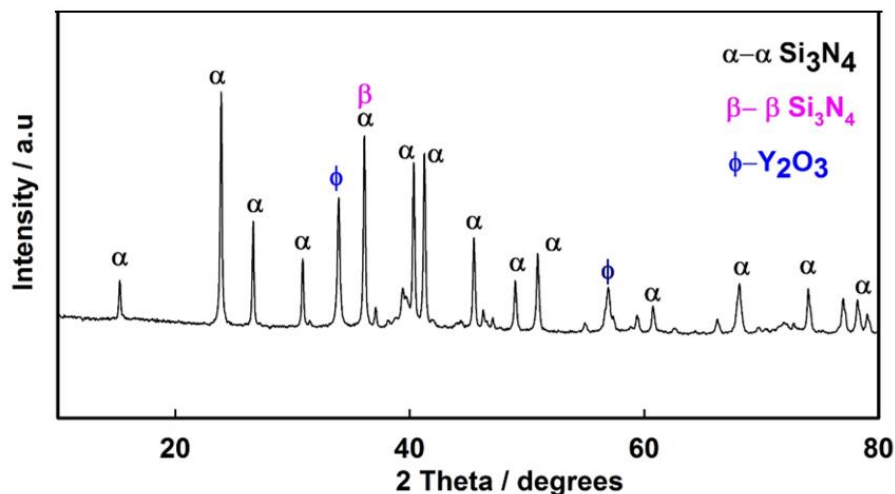
Fig. 4.20: X-ray diffraction pattern of the as-received Syalon 050 powders

The as-received powders exhibit strong peaks of crystalline α-Si_3N_4, small amounts of β-Si_3N_4 and a few peaks of Y_2O_3, which was present as a sintering aid. This is very much as expected for this powder, though some traces of Al_2O_3 and AlN, as alloying additions, might also have been expected.

4.2.3 Selection of the type and amount of binder

After the basic characterisation of the ceramic powders, the compatibility with the binder was investigated in terms of the adhesive capability and powder flowability. Of the binders listed in table 3.1, formulations 1 – 5 were incapable of providing enough adhesion capacity for even simple geometries such as a disk. Formulation 6 looked promising initially but failed to maintain the structural integrity of the whole green body by the end of the mould removal. The following images, fig. 4.21, show some of the complex shaped green bodies obtained by using formulation 6.
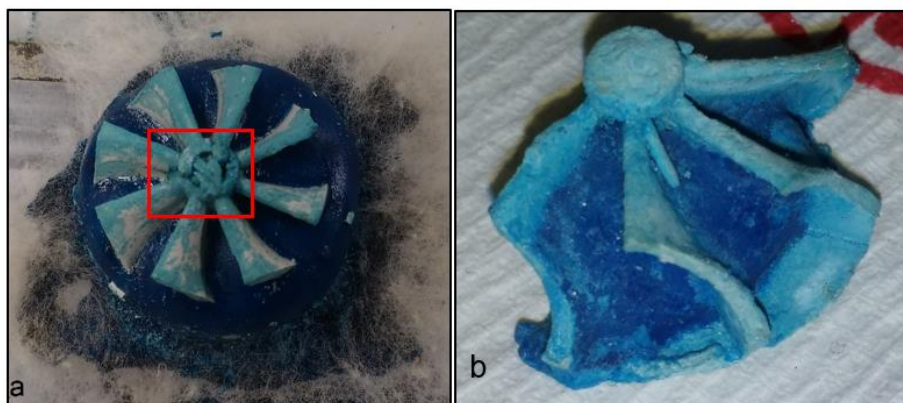
Fig. 4.21: Green bodies (approx. 35 mm dia) made from binder formulation 6, a. turbocharger rotor-sample 1; b. different turbocharger rotor-sample 2

Though the binder in formulation 6 could initially retain the green shape, cracks were induced during the mould removal stage. These grew and led to the breaking of the component, as shown in the highlighted square in fig.4.21. Other trials for obtaining the green body included slower and longer periods of heating, though the latter led to more cracks and breakage. This indicated an absence of green strength within the compact.

The binder in formulation 7 was cellulose-based. When attempting to ball mill the powder mixture with this binder system, an aerated slurry was obtained. Upon drying, a hard and

extremely porous mass was left making it unsuitable for the current fabrication method. Fig. 4.22 shows the photograph of a shrunken green body within the mould.

Fig. 4.22: Shrunken green body made from formulation 7, Walocel™ CRT as a binder

The binder selection process was finally successful when using system 8, i.e., Aquazol® 500. Though the finish of the green body was not satisfactory in the initial trials, complete retention of the green shape was observed. Fig. 4.23 shows an example of the green shape retention with 10 wt.% binder addition. After observing good adhesive properties with 10 wt.%, further experiments were conducted using 7.5, 5 and 2.5 wt.% of binder content in the powder mixtures. The green strength was observed to be sufficient to retain the green shape except for 2.5 wt.%, which was clearly insufficient. Based on these qualitative results, 5 wt.% of Aquazol® 500 was chosen to be used for the remainder of the research.

Fig. 4.23: Green body (approx. 35 mm dia) made from formulation 8, Aquazol® 500 as a binder

4.2.4 Effect of the binder on the powder flowability

Fig. 4.24 illustrates the stresses measured in the as-received ceramic Syalon 050 powders during the flowability test. The powder flowability index (FF$_c$) was calculated by taking the ratio of the consolidation stress (σ_1) and the unconfined yield stress (σ_c) under a preshear stress, σ_{pre}, of 2000 Pa. The FF$_c$ obtained was 17, which indicates extremely free flowing powders as mentioned in section 3.5.3, table 3.5. This value was expected, however, since the as-received powders were fabricated via spray drying. The other parameters measured were the bulk density (RHOB), the effective angle of friction, (PHIE(ψ_e), the minimum angle at which the particles start sliding without external force), the slope angle of the linearised locus (PHILIN,(ψ_{lin}), the angle between the tangent to the circle and x-axis) and the angle of internal friction at steady state (PHSF (ψ_{sf}), the angle between shear stress and normal stress where the breakage occurs).
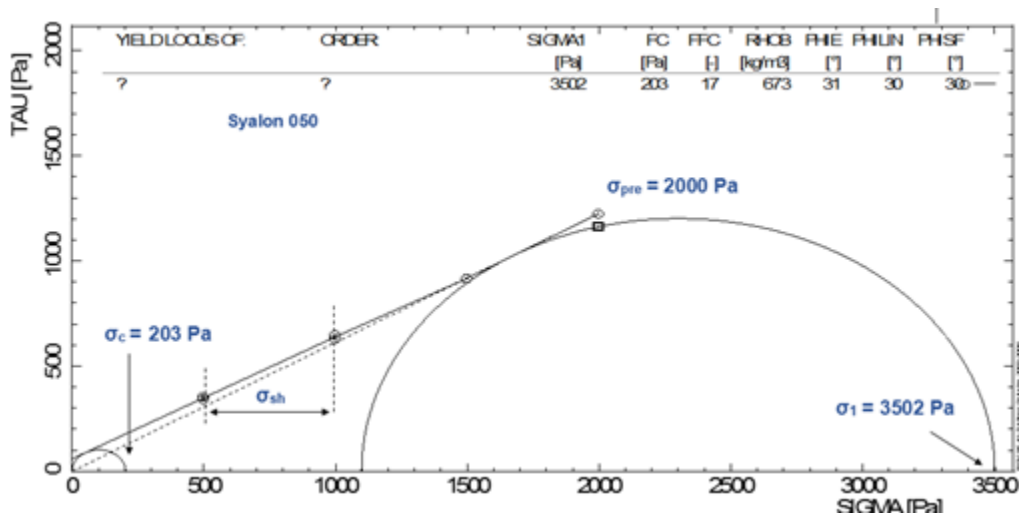
Fig. 4.24: Yield locus - Stress representation of the as-received Syalon 050 powders under a normal force of 2000 Pa

Powder mixtures containing both Aquazol® 500 as the binder and stearic acid as a lubricant were subsequently tested for their flowability since a combination of good adhesion and

flowability was needed for the indirect AM process. Fig. 4.25 shows the results for the following powder mixtures:

a. 5 wt.% binder

b. 5 wt.% binder with 1 wt.% stearic acid

c. 10 wt.% binder

d. 10 wt.% binder with 1 wt.% stearic acid
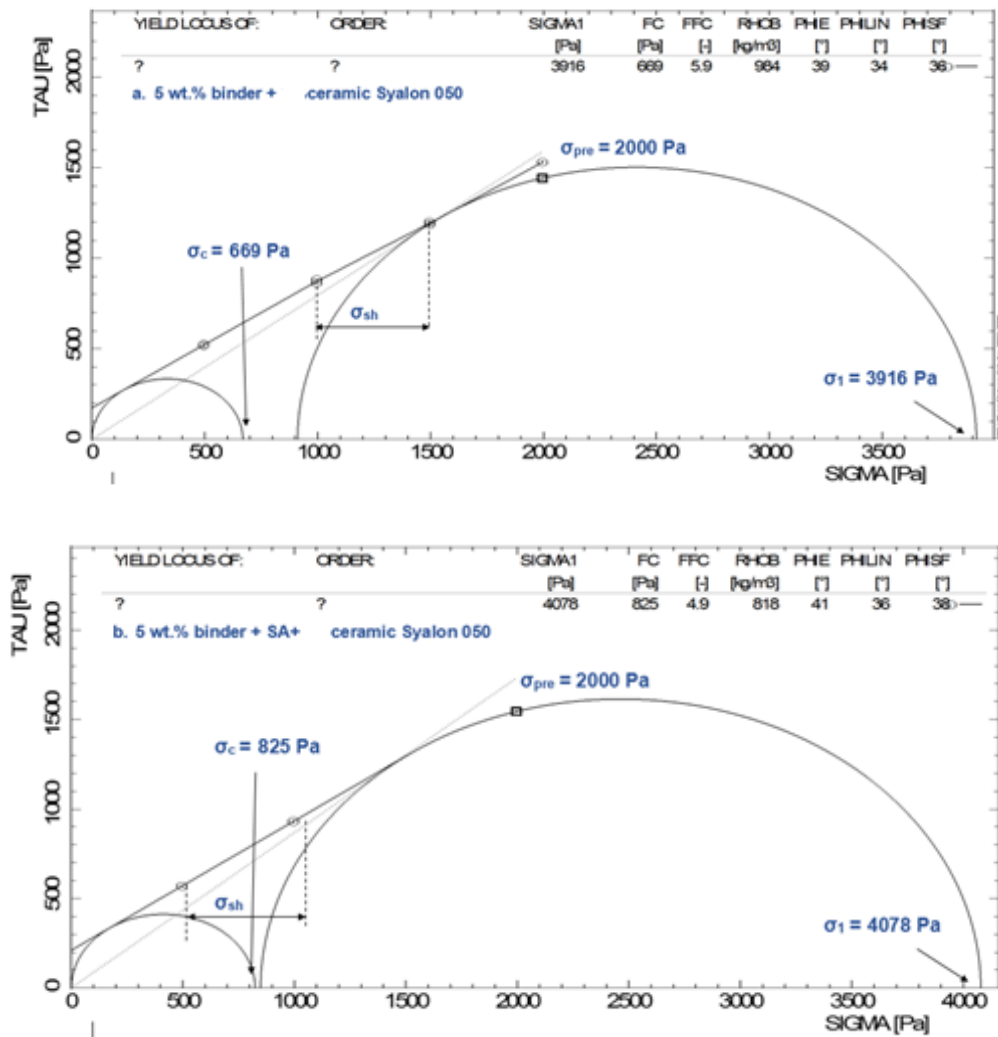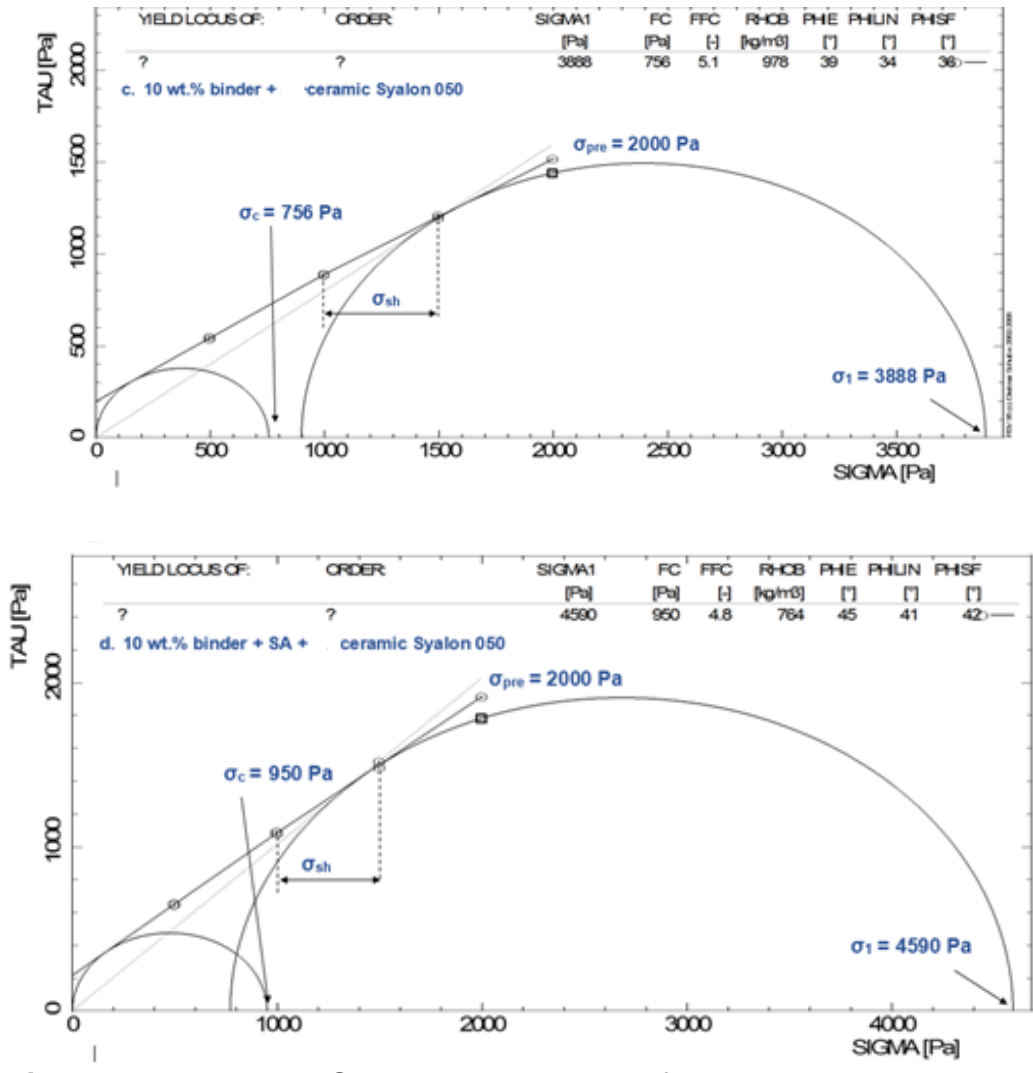
Fig 4.25: Yield locus - Stress representation of various powder compositions consisting of the binder, ceramic powders and lubricant, under a normal force of 2000 MPa, a. 5 wt.% binder; b. 5 wt.% binder with 1 wt.% stearic acid; c.10 wt.% binder; d.10 wt.% binder with 1 wt.% stearic acid
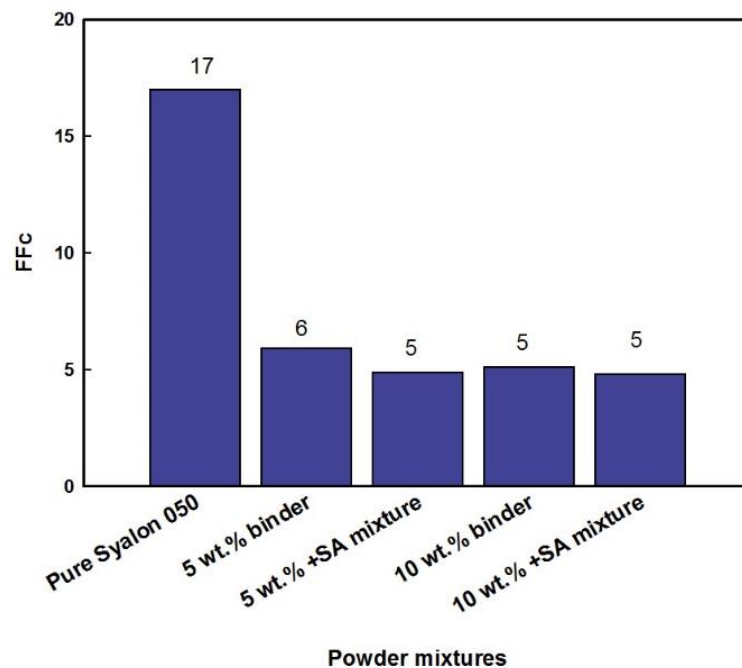
Fig. 4.26: Bar graph comparing the FF_c of the various powder mixtures [note: except for as-received Syalon 050 sample, the bar values indicate FF_c for powder mixtures that contain Syalon 050 along with binder and/or stearic acid

Fig. 4.24 shows the consolidation stress of as-received Syalon 050 powders to be 203 Pa, far less than the values measured for the other powder compositions. The flowability index corresponds well with the consolidation stress because of the powders' extremely free flowing nature. On the other hand, the addition of the binder and lubricants caused an increase in the σ_1 and σ_c, decreasing the FF_c substantially. Due to the varying contents of the sample mixture, the bulk density was observed to change in every case. This implies the possibility of varying pore volume and void volume as well.

Table 4.2: Overview of the samples with their corresponding powder flowability index, consolidation stress and the unconfined yield stress

Sample	Consolidation stress, σ_1 / MPa	Unconfined yield stress, σ_c / MPa	Powder flowability index / FF_c
As-received Syalon 050	3503	203	17
5 wt.% binder mixture	3916	669	6
5 wt.% binder + SA* mixture	4078	825	5
10 wt.% binder mixture	3888	756	5
10 wt.% binder + SA* mixture	4590	950	5
*SA = stearic acid			
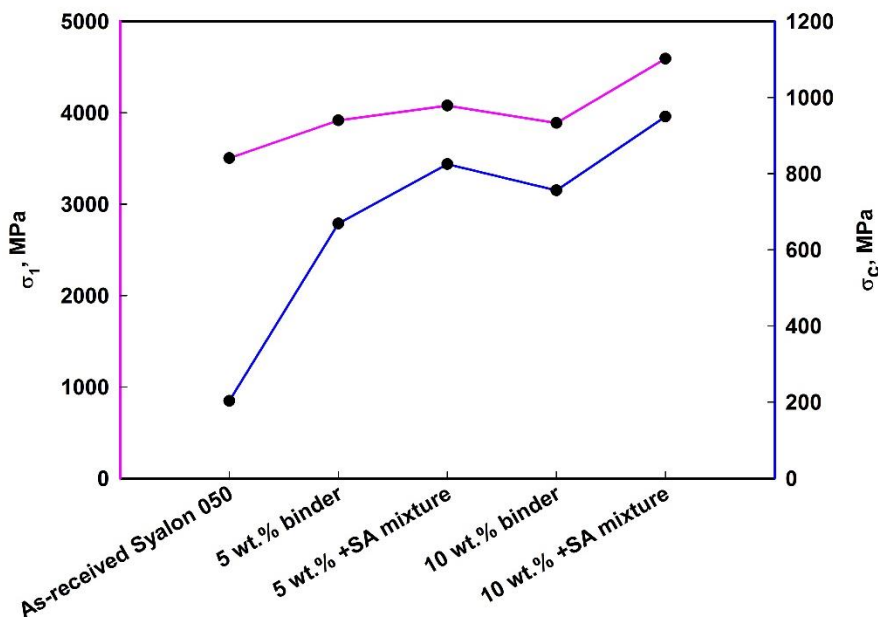
Fig. 4.27: Plot of the consolidation stress vs. unconfined yield stress of the various powder compositions

Fig. 4.27 is a comparison between σ_1 and σ_c for the different sample sets measured. Both

the plots exhibit a similar trend for the stresses. It also reveals that whilst the presence of

the binder and lubricant has a significant effect on the flowability of the powders, reducing it, the difference between have either just binder or both binder and lubricant and the different amounts of the two does not have much of an effect on flowability, though it does on the stresses, in general increasing them. Since no significant change was observed in the powder flow and consolidation stresses, stearic acid was therefore eliminated from the sample compositions to keep the number of additives to a minimum.

Mohrs' circle and the parameters involved

The stress state in a bulk solid cannot be completely described by a single numerical value. Depending on the actual load acting on a bulk solid element, the corresponding Mohr stress circle can have a smaller or a larger radius, a centre at a lesser or greater normal stress, and hence different principal stresses, σ_1 and σ_2 (the diametrically opposite end of σ_1). In principle, at a given major principal stress, σ_1, stress circles with different values for the lowest principal stress, σ_2, are imaginable. Therefore, a stress circle is defined clearly only if at least two numerical values are given, i.e., σ_1 and σ_2. This simplification or approximation is used here when the tie rods exert normal forces on the shear cell through weights of mass m. Thereby, as a rule, one characterizes the stress state by the major principal stress, σ_1, which in this case is equal to the force of gravity, m x g, of the weights divided by the area, A (area of the shear cell), and denotes this stress as the consolidation stress, σ_1.

4.2.5 Determination of the required compaction force for the powder mixture

The amount of compaction force required to produce a compact without any cracks or flaws was determined by the simple method of compacting the powder mixtures using a hydraulic uniaxial press over a range of normal stresses, calculating the density and visually inspecting for flaws. In this case, forces from 49 to 147 N were involved using a 35 mm

diameter steel die. Two powders were investigated, one was the as-received Syalon 050 powder whilst the other contained 5 wt.% binder. Owing to its very free flowing nature, consolidation of the as-received Syalon 050 was not possible, even at high stresses. On the other hand, the powder containing binder formed discs readily and fig. 4.28 shows the density of the compacts obtained.
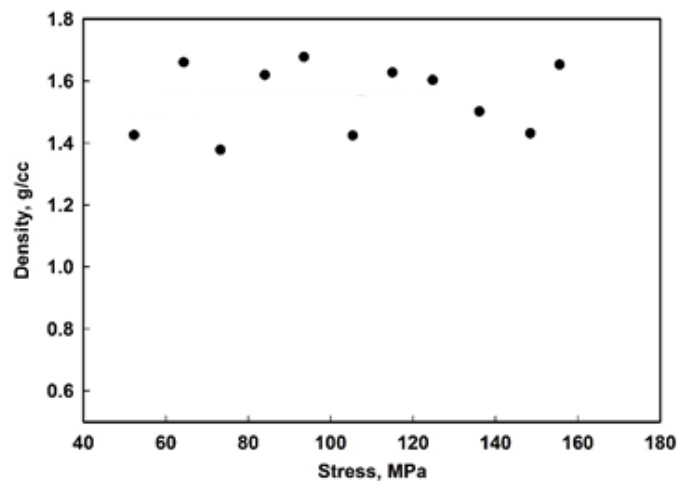
Fig. 4.28: Stress vs. density obtained on powder mixture containing 5 wt.% binder and 95 wt.% Syalon 050 powder

It can be seen that there was little variation in density; the linear fit showing a slight increase in density with stress applied as expected. The average density was measured to be ~1.6 g cm^{-3} (i.e. ~50% of the theoretical value), which is in general agreement with the uniaxial pressing of green ceramics[192]. Although the discs fabricated with stresses as low as 50 - 75 MPa were reasonably dense, some powdery residue was found on the discs after the ejection from the die. Discs that were fabricated with stresses >95 MPa had no residue and, hence, keeping in view the industrial practice of using low maintenance equipment and looking at the quality of the pressed discs, a value of 110 MPa (equating to a force of 98 N) was chosen for all the uniaxial compactions in this study.

Thermogravimetry analysis of the binder

After finalising the binder and its compatibility with the powder, thermal analysis of Aquazol®
500 was undertaken to help design the heat treatment process for the debinding stage, fig.
4.29.
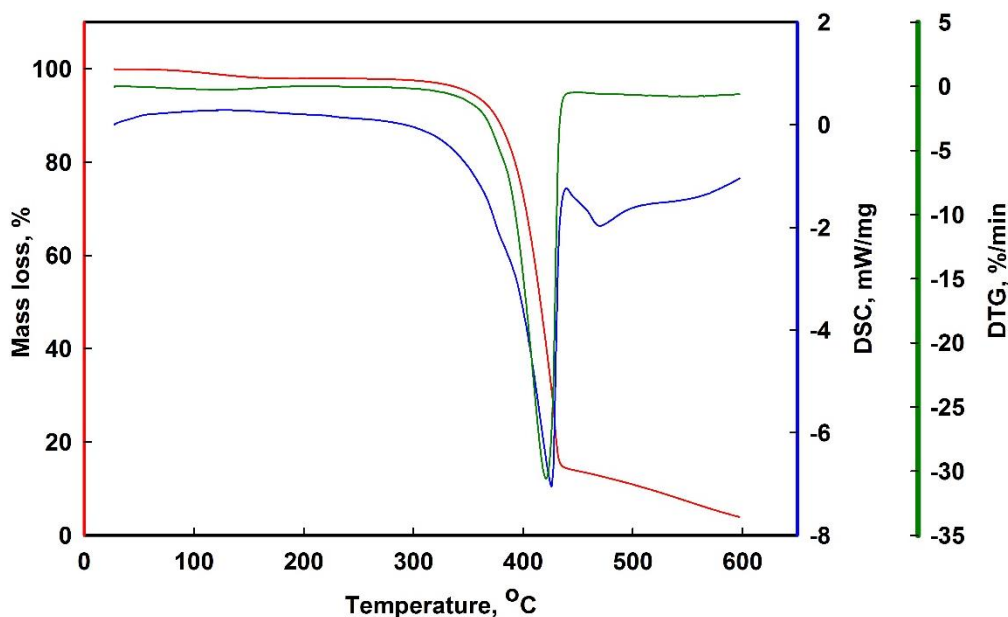
Fig. 4.29: Thermal analysis of Aquazol® 500, the binder

The onset of thermal degradation was observed from ~350°C; the major mass loss could be
attributed to the evolution of nitrogen oxides and carbon oxides[193,194]. This is shown as an
endothermic reaction, however, even by 600°C the binder is seen not to decompose
completely. A change in the gradient of the mass loss % curve at approximately 420°C can
be seen, indicating a slower mass loss. This behaviour continues just beyond 600°C. The
DSC curve exhibits an exothermic reaction for the second stage of mass loss, which occurs
at ~425°C. The manufacturer reports residual low levels of halogens, Al and Na[195], which
are probably from the degradation of the R group attached to the oxazoline monomer; the
chemical formula of the polymer as shown in fig. 3.11. The greatest rate of change on the

mass loss % curve, which occurs at ~420°C, can be seen as a peak in the DTG curve indicating a solid to gas phase transformation of the organics.

4.2.6 Extent of powder distribution inside the mould cavity

After the investigation of the powder flow behaviour and thermal analysis of the binder, the moulds (after the interfacial material had been sprayed on) were filled with the powder mixture and subjected to the uniaxial compaction. This result in compacts within the moulds that looked like those shown in the fig. 4.30 after gently grinding off the excessive compacted powder.

Fig. 4.30: Powder compacts within the moulds after ejection and gentle grinding

Though the surfaces always looked acceptable, non-destructive computer tomography was used to evaluate the internal structure of the compacts and hence investigate the powder behaviour after compaction. This yielded information on the extent by which the powders filled the mould and also allowed the presence of cracks and pores to be detected within the component, Finally, the test was concluded by quantifying the pore volume within the components.

The fig. 4.31 illustrates an X-ray microCT image of a green component within the mould for the engineering gear. Three locations were selected for pore volume measurements; these

are indicated in the figure. Due to the assumed presence of symmetrical radial stresses, data from these locations were expected to be similar to that in other parts of the component. The results are shown in fig. 4.32.
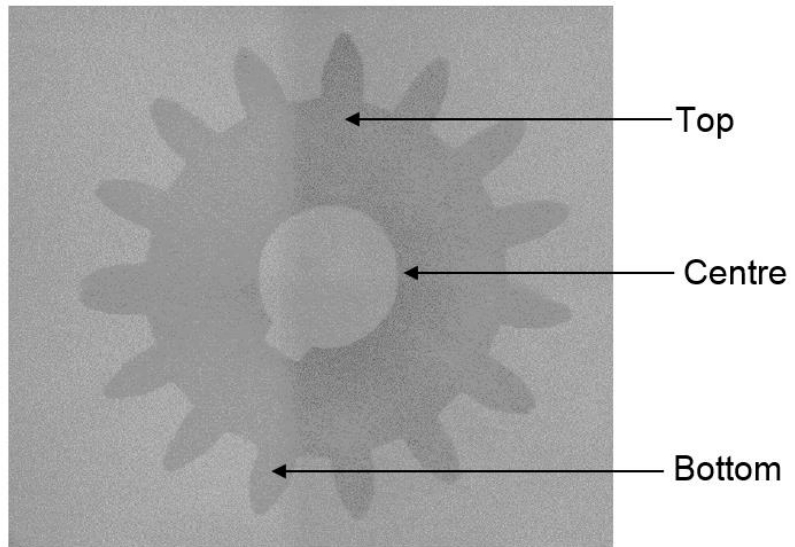
Fig. 4.31: An X rayed image of a compact within an engineering gear mould
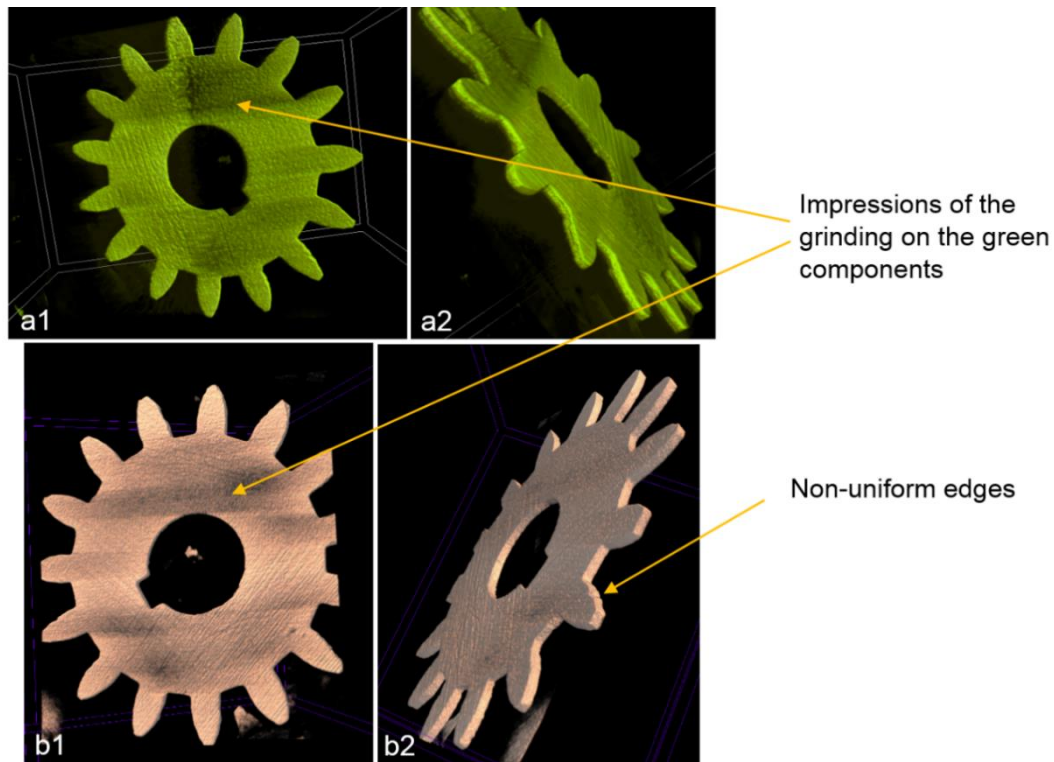
Fig.4.32: 3D illustrations of powder compacts of engineering gears of varying thickness, a1. front view of gear 1 (thickness ~2 mm); a2. angled view for the edges of gear 1; b1. front view of gear 2 (thickness ~3 mm); b2. angled view for the edges of gear 2

The 3D constructed images of the green bodies within the mould in fig. 4.32 show no presence of cracks, however, marks from the grinding operation performed to remove the excess powder after the compaction can be seen. Due to the non-uniform distribution of these manual grinding marks, erratic surface roughness values were sometimes measured on the sintered components. These irregularities could act as stress concentrators and result in the deterioration of mechanical properties of the component; this could have been avoided by employing a finer grade of machine grinding. Machine grinding would eliminate non-uniform pressure points leading to smoother surfaces. Wet grinding could not be used due to the fragile nature of the green bodies. The images also show some poorly formed edges of the gear teeth. The data from fig. 4.7 - 4.15 and table 4.1 clearly show that the surface of

the grooves within the cavity of the mould has a higher surface roughness value than the top surface; the influence of this level of finish is seen on the edges of the green body.

A pore volume analysis was conducted on these compacts within the moulds by stacking a series of x-y plane slices in the z-direction of the component to create the volume of interest. The same three locations, as shown in fig 4.31, were used. Table 4.3 provides information on the volume of closed and open porosity and the final porosity recorded individually at these three locations. A typical green body formed from uniaxial pressing is expected to have approximately 55-60% of theoretical density[192], i.e. 40 – 45% porosity.

The volume of the open porosity calculated by the NRecon software is significantly higher than the volume of the closed pores. One of the reasons for this could be due to the software algorithm used. When selecting a volume of interest (stacked z slices in the xy plane) it could have considered a part of the closed pore on the topmost slice to be open. If a slice just above the top slice was selected, this open porosity could be measured as closed porosity depending on its size. A similar thing happens with the bottom most slice within the stack. However, the central volume has significantly lower porosity recorded among the three locations indicating the presence of radial stresses acting during the compaction (stresses decreasing radially outwards).

Table 4.3: Results of the measured porosity of the green gear

Morphometrical parameter	Top	Centre	Bottom
Volume of interest / μm^3	2.03×10^9	2.01×10^9	2.59×10^9
Volume of closed pores / μm^3	2.14×10^6	2.49×10^5	1.45×10^6
Volume of open pores / μm^3	1.42×10^9	1.72×10^9	1.54×10^9

The compacts were then removed from the moulds by the melting of the latter; images of the resulting green bodies can be seen in fig. 4.18.

4.3 Sintered Syalon 050 components

Fig. 4.33: Sintered Syalon 050 components (note: the scale in all the pictures is represented in mm), a, b and c turbocharger rotors fabricated in three different trials; d. circular sprocket gears and tools parts (four-sided) for welding; e. engineering gears (thickness >0.5 mm); f. engineering gear (thickness ~0.1 mm); g. flawed sintered components with visible pores and cracks

Fig. 4.33 shows various sintered bodies obtained from different batches of fabrication operations. The quality of the surface finish was investigated in terms of surface roughness and surface profile heights, the results of which will be discussed next. Though the density of the sintered components was close to the theoretical value of 3.2 g/cc, a few irregularities

were observed on the surfaces. For example, in fig 4.33a, b, and c, though no cracks are observable, some bits have been broken on the blades and the base is improperly shaped due to insufficient powder within the mould during compaction. In fig 4.33d (particularly the 2 right hand most images), some surface anomalies can be observed on the sprocket gears that look like very fine layers on the surface. They were only observed on one side of the sprocket gears and can possibly be attributed to the non uniform thickness of the interfacial material and/or pressing defects. The layers may have been formed by the spalling off of the surface layer of powder during the sintering process and after the interfacial material decomposed completely (>800°C[‡‡‡‡]). Additionally, some of the parts of the sintered components bearing curved sections were observed to be deformed; the reason for this is discussed in section 4.1.4 and relates to the instability of thin structures under the stress of compaction. Fig. 4.34 illustrates both the layers and the curved distortion; the former was rarely observed among the samples whereas the distortion of the curved portions was a frequent occurrence.
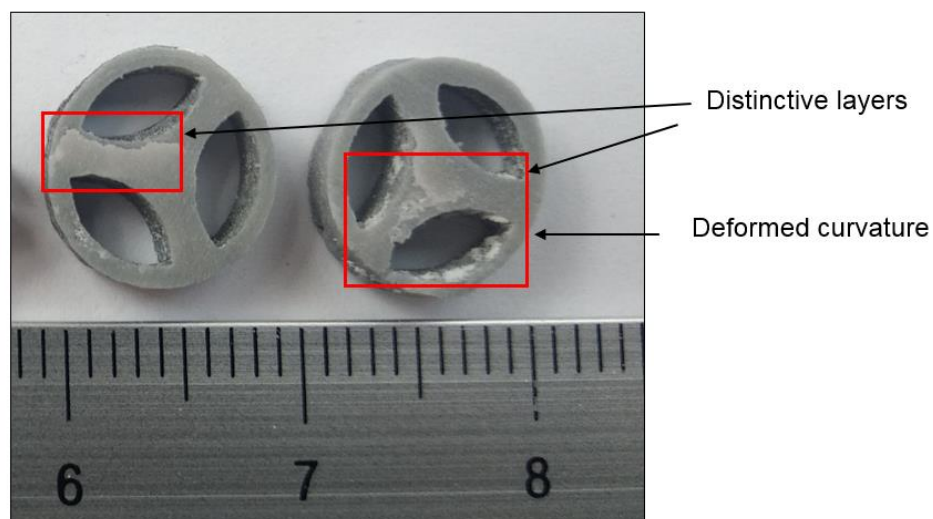
Fig.4.34: Enlarged area of the sprocket gears from the fig. 4.33d with defects highlighted

---

[‡‡‡‡] Information from the manufacturer

The density of the sintered ceramic components was calculated according to the Archimedes principle and they ranged from ~94 to >99% of the theoretical value. A mass loss of 22 to 25% was observed in all the cases irrespective of the shape and size of the components, which can be attributed to the loss of the binder, whilst the sintered samples exhibited a shrinkage ranging from 19 to 30% in terms of length, width and height dimensions.

Interior and exterior morphological analysis
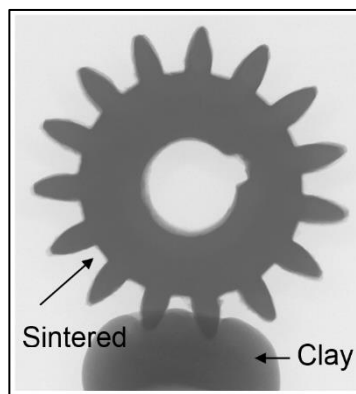
Fig. 4.35: An X-ray microCT image of a sintered Syalon 050 ceramic gear

A morphological qualitative analysis was made on a sintered Syalon 050 gear, held by a clay holder, to investigate its internal surfaces using X-ray microCT in fig. 4.35. This also included a pore volume analysis.
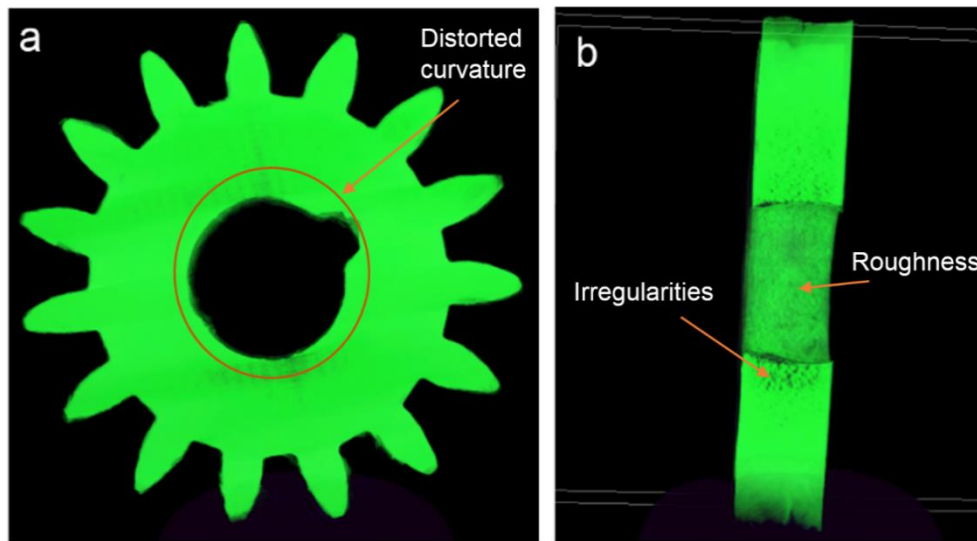
Fig. 4.36: 3D illustration of a sintered Syalon 050 ceramic gear, a. front view, b transverse side view

Fig. 4.36 shows a 3D construction of a sintered gear of approximate thickness of 2 mm. The first image, (a), shows a front view of the gear where the impressions of the grinding are still visible. Some of the defects invisible to the naked eye can also be observed here, such as the distortion of the inner circular part and the notch (highlighted). The second image, (b), shows the transverse section of the gear where some defects such as high roughness and irregularities can be seen. The roughness is assumed to originate from the mould whilst the irregularities dark spots that are located close to the inner circular part and they gradually fade away radially. A deeper investigation is required to examine these features and their origins. Additionally, some difference in the density that can be seen near the gear teeth (top and bottom of the gear).

Table 4.4: Results of the measured porosity of the sintered gear

Morphometrical parameter	Top	Central	Bottom
Volume of interest / μm^3	2.03×10^9	2.03×10^9	2.02×10^9
Volume of closed pores / μm^3	4.01×10^1	2.09×10^5	2.09×10^5
Volume of open pores / μm^3	4.33×10^3	1.63×10^4	1.48×10^3

The quantification of the pores was conducted in the same manner as for the compact within the mould. There was no porosity visible either on the surface or internally and this is supported by the data presented in table 4.4. On measuring the sample's density using Archimedes' principle, a value of >99 % of the theoretical density was obtained. The same computational algorithm was used for the pore volume analysis as in the case of the green bodies. The average total porosity of the sintered components was calculated almost close to zero, indicating a highly dense ceramic component.

Further to the qualitative analysis, the study was extended to quantifying the surface irregularities in terms of surface roughness and height profiles. Two completely sintered ceramic Syalon 050 components were subjected to a complete surface scan on both sides, with the roughness and height profiles being measured across a chosen length on the sample and then compared. Production of smooth and repeatable surface profiles across different samples is important to reduce the post-processing operations required, such as polishing.
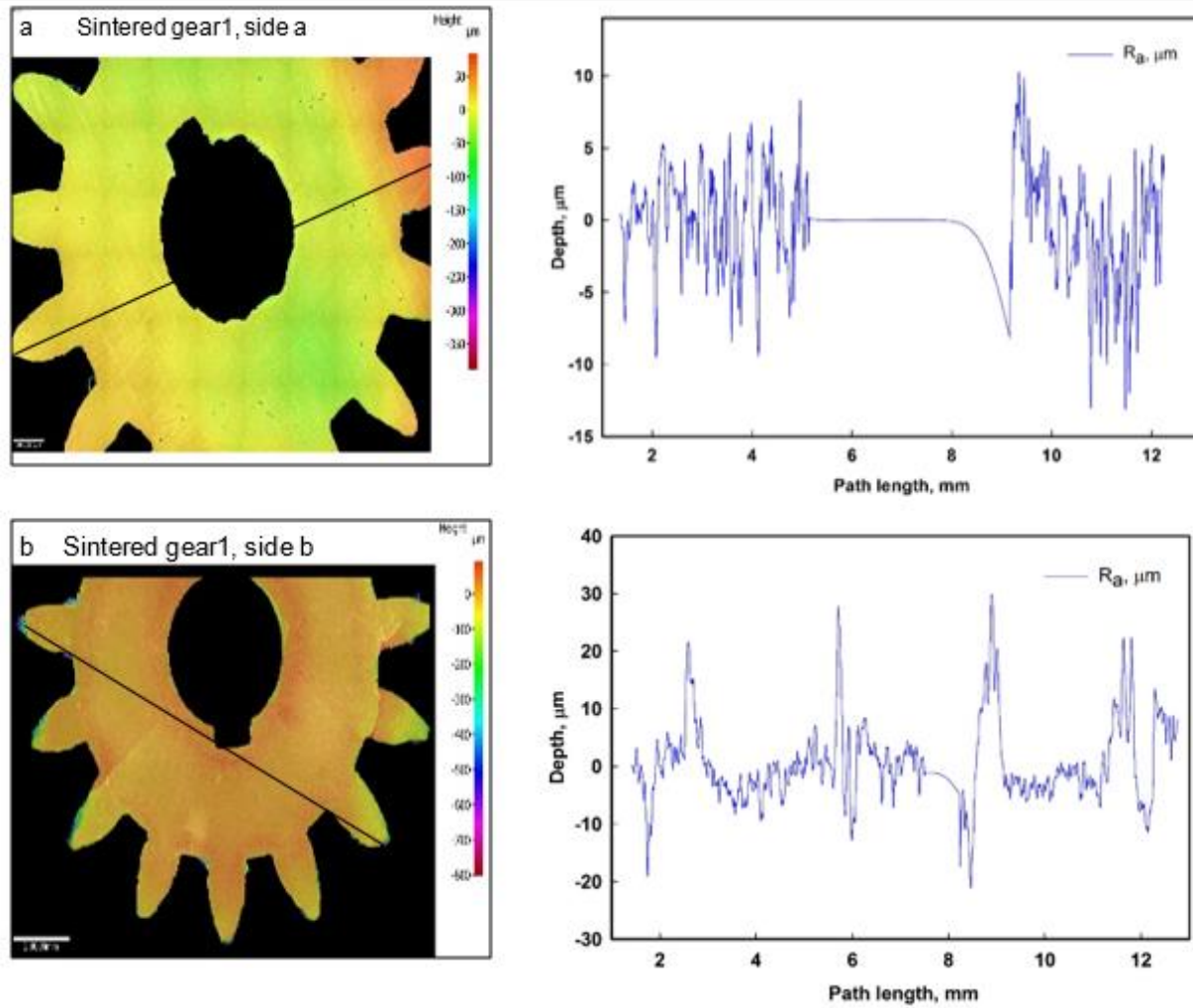
Fig. 4.37: Surface roughness of a sintered gear, a. side a and its roughness profile; side b and its roughness profile
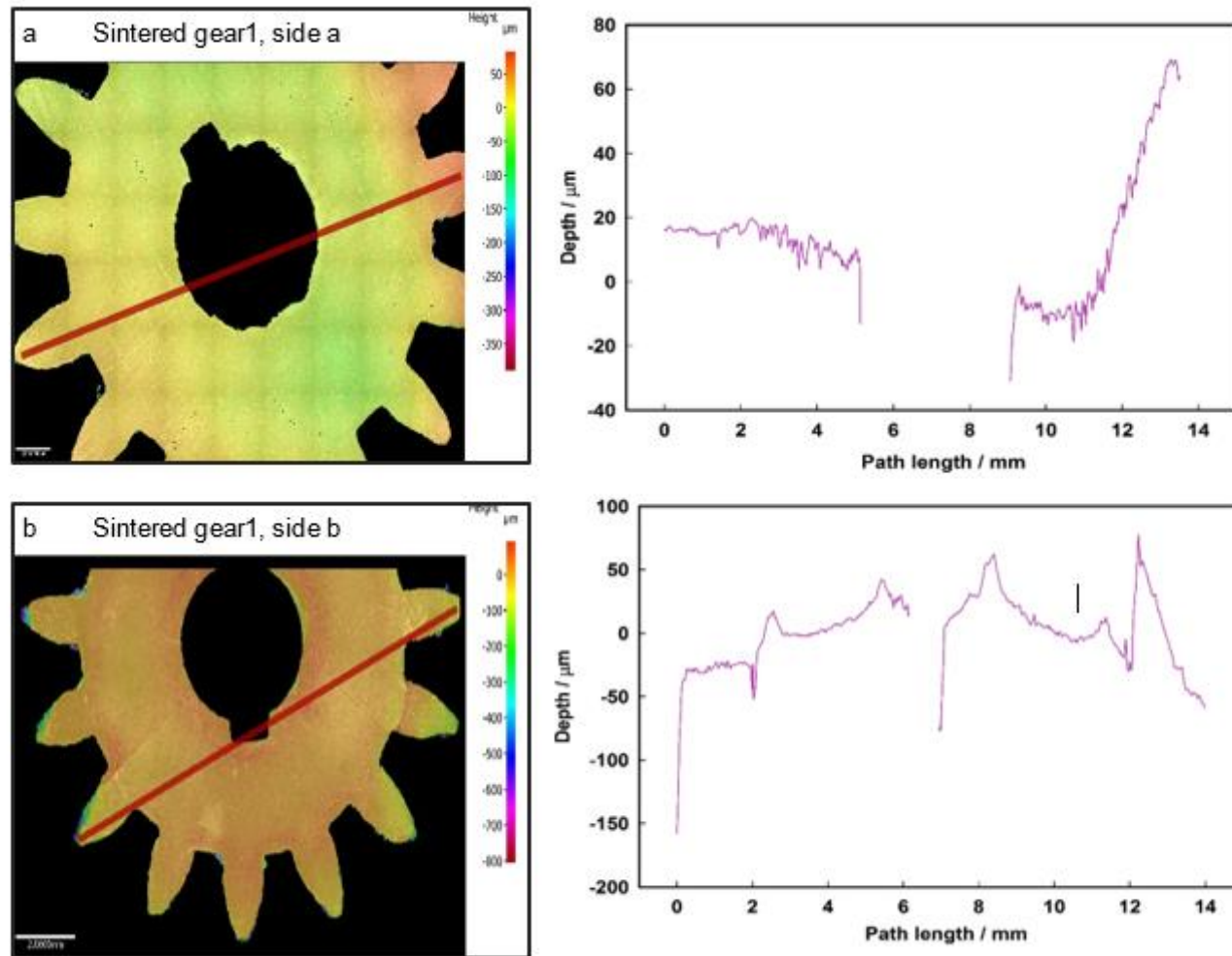
Fig. 4.38: Surface height profiles of the same sintered gear as for fig. 4.37, a. side a and its height profile; side b and its height
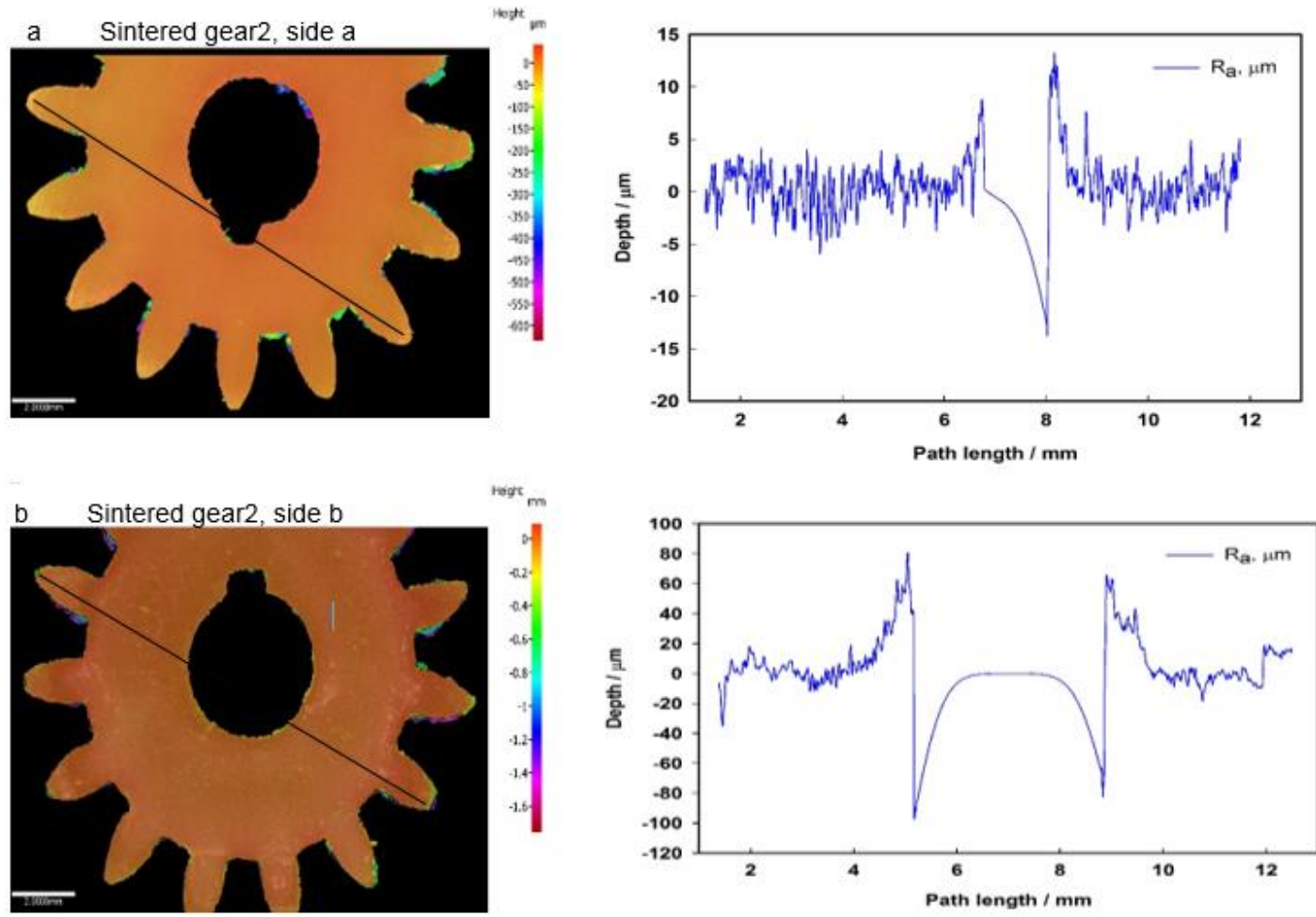
profile

Fig. 4.39: Surface roughness of a different sintered gear, a. side a and its roughness profile; side b and its roughness profile
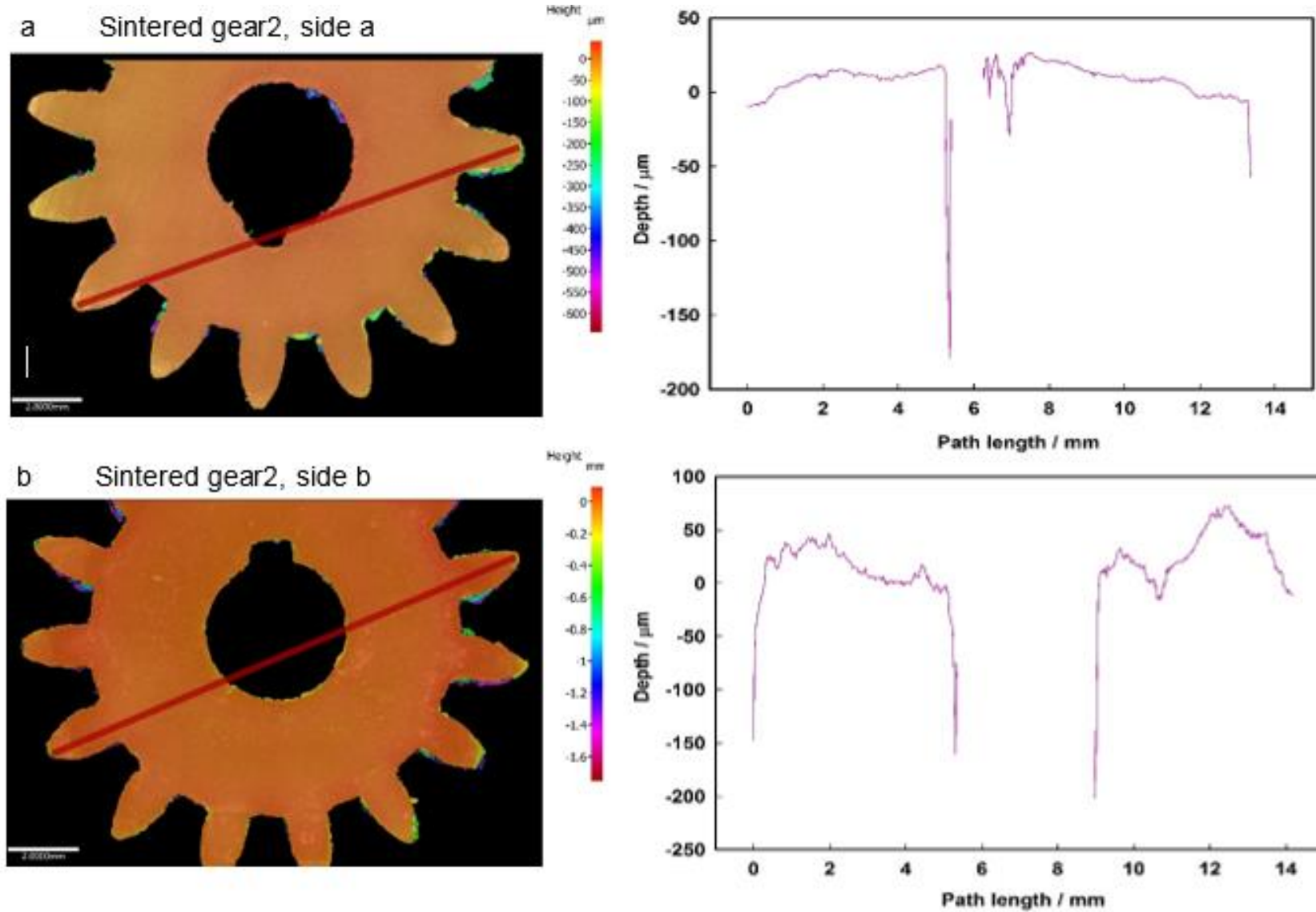
Fig. 4.40: Surface height profiles of the same sintered gear from fig 4.39, a. side a and its height profile; side b and its height profile

Table 4.5: Comparison of surface roughness measurements

Sample	R_a, μm
Gear1, side a	2.1
Gear1, side b	4.9
Gear2, side a	2.4
Gear2, side b	13.8

From the data presented in the fig. 4.37 and fig. 4.39, there is a significant difference in the measurements of the surface roughness of the samples. All the four surfaces were found to have irregularities on their surfaces. This is clearly shown in the colour map of the surfaces as well as the roughness graphs. Table 4.5 presents the quantified data of the same. Although the representative sides 'a' of both gear 1 and gear 2 exhibit similar roughness values, the other sides show a great variation. At this point, it must be noted that during the mould removal process, side b of the component was subjected to manual grinding whilst the other side was inaccessible for any kind of modifications. Therefore, the representative side 'b' of both the components have undergone the grinding operations while the other sides 'a' remain unmodified.

The fig. 4.38 and 4.40 illustrate the height profiles of the components along the drawn path. To avoid post-processing polishing, the surface profiles are required to be uniform. These irregularities are due to the surface roughness of the interfacial moulds and the manual grinding. Additionally, other surface irregularities can also be seen along the edges of the gear teeth due to the mould roughness.

Hardness and flexural strength
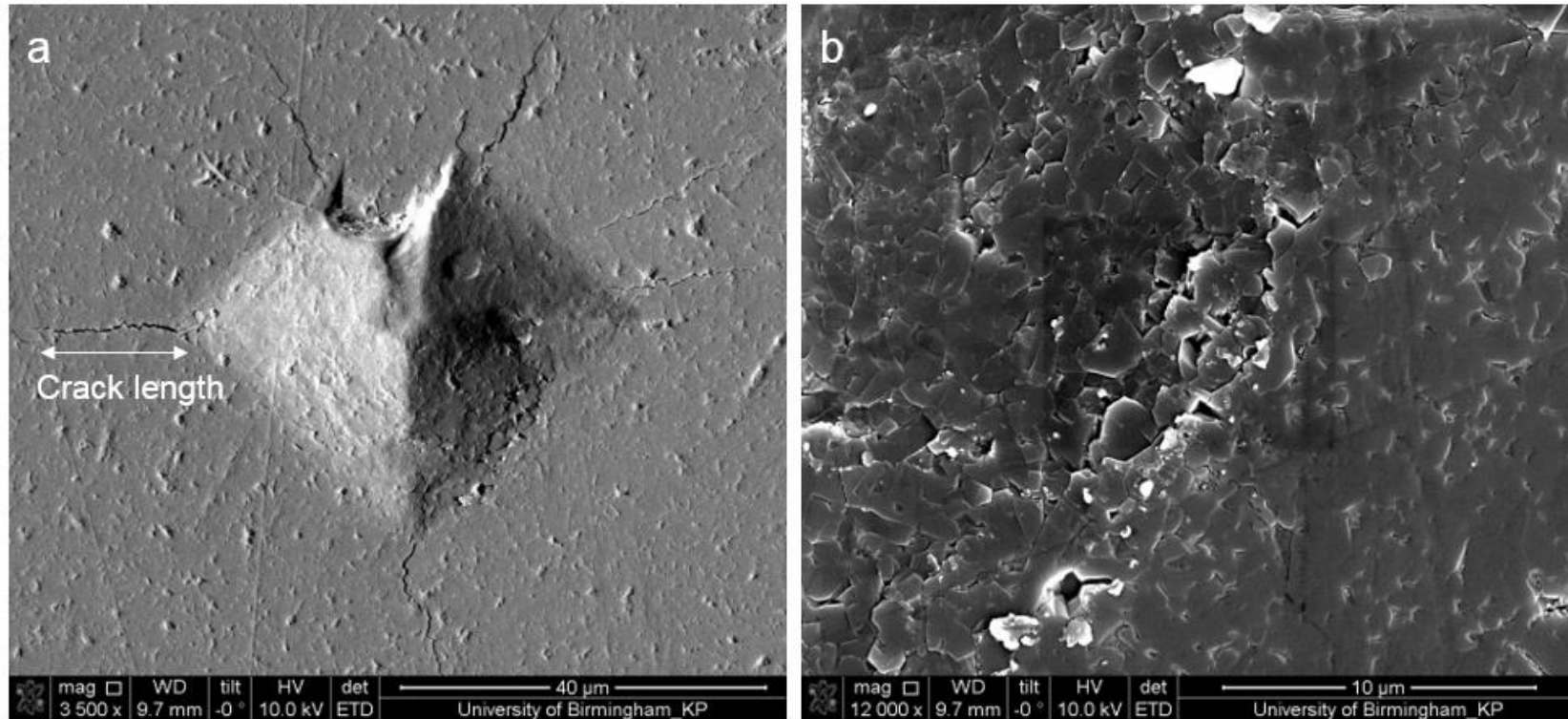
Fig. 4.41: Micrographs of a hardness test on a sintered Syalon 050 component, a. indentation and the cracks caused; b. the induced crack path due to the indentation

Figure 4.41 illustrates an indentation made by the diamond indenter. The diagonals of the indenter were measured using the in-situ callipers. From the first image, it can be seen that the indention is not complete due to the chipped indenter[§§§§]. The diagonal measurement on this indent was made by an extension of the indent geometry. Indentations were made on the surface and the internal transverse surface. This variation helped to understand the extent of sintering within the thickness of the sample. The second image illustrates the path of a crack that developed as a result of the indentation. The crack path is seen to be intergranular because of the presence of the interlocked elongated crystals of β-SiAlON phase. Similar behaviour can also be seen in fig. 4.42d. Taking an average of five readings, the hardness values using 98.1N (10 kgf) was calculated to be as the following

$$\text{Surface: } HV_{10} = 2545 \pm 351$$

$$\text{Transverse: } HV_{10} = 2462 \pm 246$$

From both the values, it can be seen that there is not much variation in the hardness levels, hence the sintering process has been achieved uniformly across and within the samples. These values are also comparable to those measured by other researchers (HV_{10}~2000 based on varying z value for β SiAlON)[1,2,4] who worked on different grades of SiAlON ceramics.

The flexural strength tests conducted on ten samples yielded an average value of 86 ± 12 MPa as the flexural strength. This is a much lower value than the ~850 MPa typically claimed by the manufacturer[*****]; this can be attributed to the warpage and cracks on the samples.

[§§§§] Note: Due to the Covid-19 crisis, it wasn't possible to repeat the measurements with a non-chipped indentor.
[*****] www.syalons.com
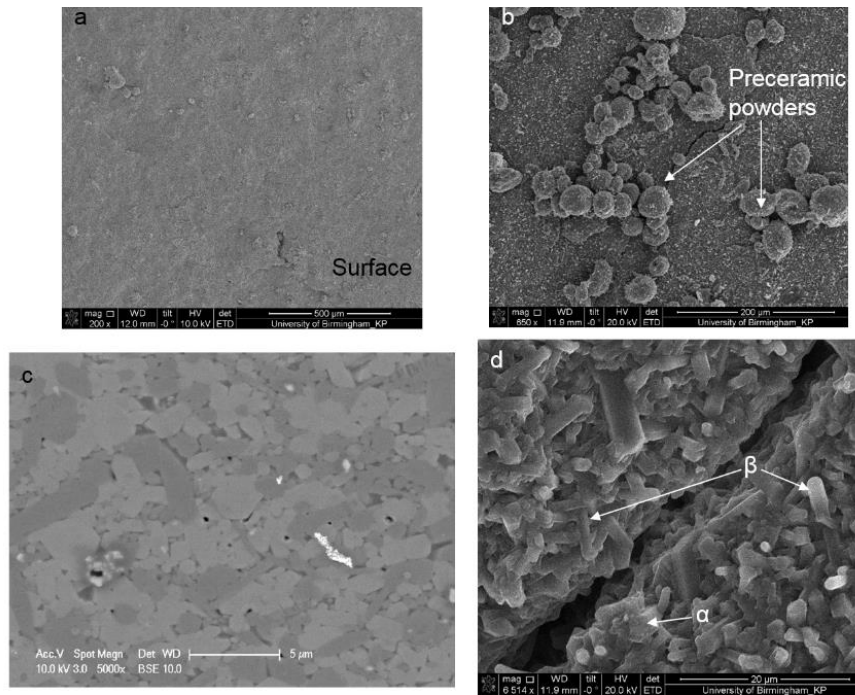
Fig. 4.42: Scanning electron microscopy images of sintered Syalon 050 components, a. surface; b. surface with the spray dried powders from the powder bed; c. image illustrating different grain orientations; d. equiaxial α-SiAlON and the elongated interlocking β-SiAlON (around a crack)

The scanning electron microscopy images are illustrated in fig.4.42. The first image shows the surface to be mostly devoid of porosity. During the sintering process, some powder particles were picked up by the components, which are shown in the second image. These are the spray dried ceramic powders, typically with a doughnut shape with a depression in the centre. The third image shows the different grain orientations via backscattered electrons whilst the final image illustrates the two main phases: the elongated interlocked crystals of β-SiAlON and the equiaxial particles of α-SiAlON. The reason for the better mechanical strength of SiAlON components compared to other ceramics is attributed to this microstructure. The interlocking mechanism is responsible for hindering the crack growth[3,131]. Hence, the mechanical strength properties are enhanced.

Phase analysis
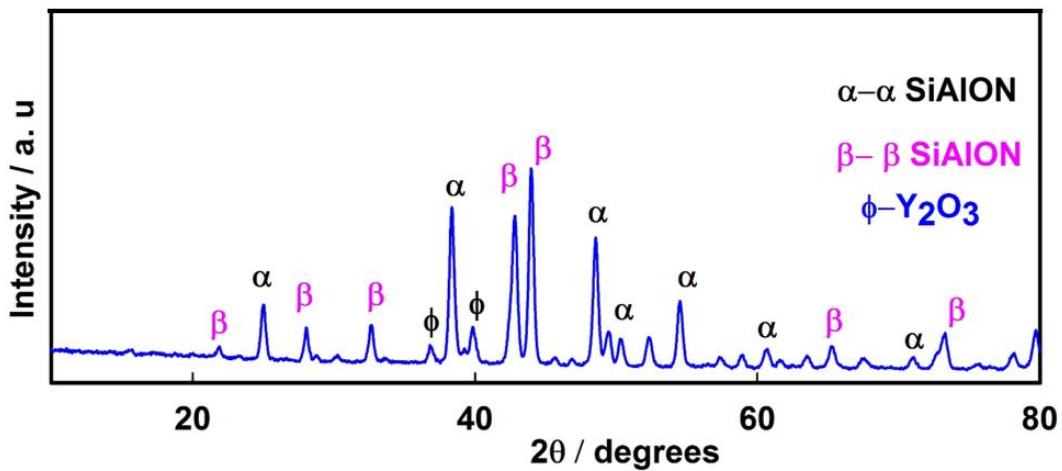
Fig. 4.43: X - ray diffraction pattern of sintered Syalon 050

Sintered Syalon 050 components were observed to contain a mixture of both α-SiAlON and β-SiAlON phases. In theory, a complete α→β transformation was expected. However, the presence of α phase shows either partial transformation or reciprecipitation by the end of sintering. Reverse transformation of β→α seems unlikely due to the lack of high reconstruction energy required[3,118]. Based on the diffraction pattern, as shown in fig. 4.43, the α phase detected has x=0.5, suggesting the composition of the α-SiAlON was **$Y_{0.5}Si_{9.3}Al_{2.7}N_{15.1}$**. Based on the β peaks detected, the z value could be concluded as 0.5 or 1[196,197]. However, further investigation using a transmission electron diffraction patterns is required to verify this statement. The sintered sample is observed to have almost equal phase fractions of α and β phases based on the relative intensity ratios (section 3.5.4). Some small peaks of Y_2O_3 were also detected. The unmarked peaks were found to be a mixture of α and β phases.
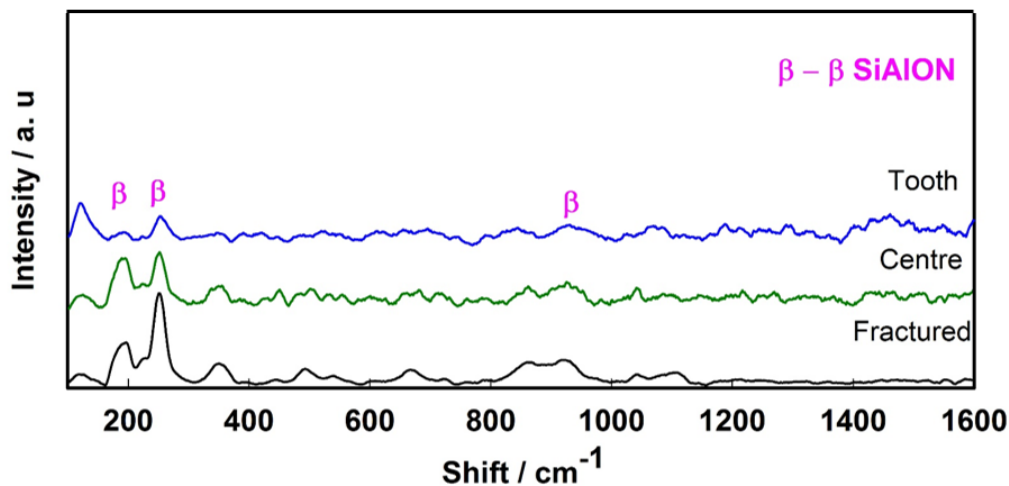
Fig. 4.44: Raman spectroscopy for different areas of a sintered Syalon 050 gear

Along with a phase analysis, an attempt was made to investigate the presence of residual stresses in the sintered Syalon 050 components. The first attempt included measuring microstrain using XRD, which yielded no difference in the signal from the crystal lattice before and after the application of a stress field. X rays usually penetrate up to 50 μm from the surface. Since no significant value of strain was recorded by this method, it was assumed that neutron diffraction would also not produce any different result due to a similar penetrative capacity. The second attempt was using the fracture contour method[†††††]. This method was also unsuccessful since newly cut flat plane surfaces of the sample were required. It was not possible to obtain such samples without introducing new stresses. Finally, the last attempt was made using Raman spectroscopy. Measurements were made on a sintered gear within the central area (around the circular hole) and one of the gear teeth. These measurements were compared to that of a fractured surface since the latter would be free of residual stresses. All three measurements' spectra are shown in fig. 4.44. The data obtained helped to verify the presence of the β SiAlON phase[197]. Changes were observed in the peak shifts and intensities around 200 cm^{-1} however, this did not necessarily

---

[†††††]https://www.stressmap.co.uk/contour-method/

indicate the presence of residual stresses. Several factors such as the laser power used, crystallite sizes, chemical bond length in the phases at the measurement locations all contribute to the peak shifts. Other residual analysis techniques could be explored to examine the SiAlON ceramics in the future, more details are outlined in section 5.2.

4.4 Oxidation studies

Oxidation studies were conducted at a temperature of 1450°C. This temperature was chosen to test the claims of the manufacturer that sintered Syalon 050 could operate up to a temperature of 1450°C. Mass changes were recorded over 24, 48 and 72 h, the microstructures and the phase composition were analysed at this temperature.
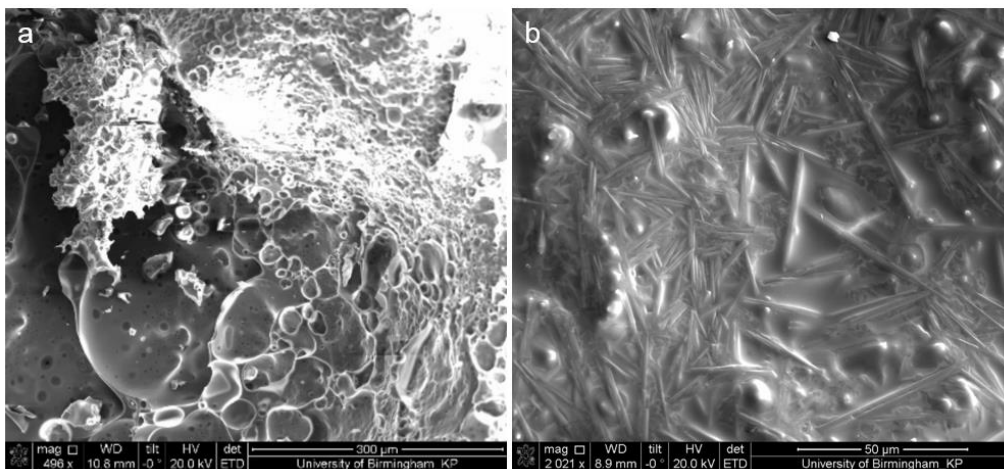
Fig. 4.45: Sintered Syalon 050 after oxidation for 24 h at 1450°C, a. surface on the oxidised area showing escaping nitrogen; b. surface on the ceramic showing β- SiAlON within a glassy matrix

Fig. 4.45 illustrates two of the areas on a sintered sample subjected to isothermal oxidation at 1450°C for 24 h. The first image illustrates an area close to the interface of the ceramic and oxidation scale. It clearly shows the formation of bubbles and it was concluded that this was the nitrogen gas escaping on the decomposition of the SiAlON ceramic[4]. The second

image shows the elongated rod-like crystals of β SiAlON in a glassy matrix; the latter is assumed to be the solid solution of the α phase resulting in yttriumalumino silicate[12,131]. Here, in this study, the sintered ceramic is a mixture of both α and β phases and both are expected to interact with the incoming oxygen. Researchers have proposed mechanisms of oxidation occurring in SiAlON ceramics. These mechanisms have been discussed in detail in section 2.6. These mechanisms include decomposition of either the α phase or the β phase.

The mechanism of oxidation[4] for the β phase is based on the fact of the cationic ions (Y^{+3}) diffusing outwards from the ceramic. The sintering additive Y_2O_3 tries to participate by forming many phases, however, ultimately precipitates. It is mainly responsible to form the refractory phase. In the meantime, the β SiAlON decomposes to form cristobalite (SiO_2), and silicon oxynitride. The protective layer formation of SiO_2 can be confirmed from the XRD pattern, fig. 4.50 concludes the occurrence of passive oxidation. The escaping nitrogen gas often forms craters, as shown in fig. 4.45a[4]. An EDX analysis was conducted on the locations shown in fig. 4.45 and the results are as follows:
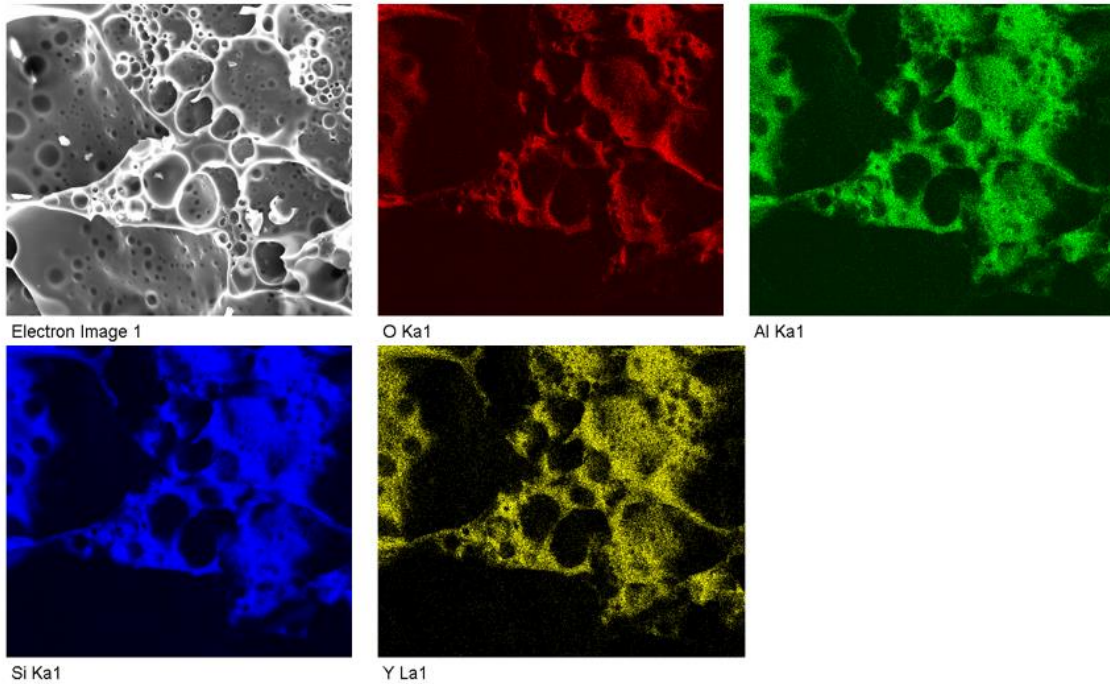
Fig. 4.46: EDX analysis of image a in fig. 4.45
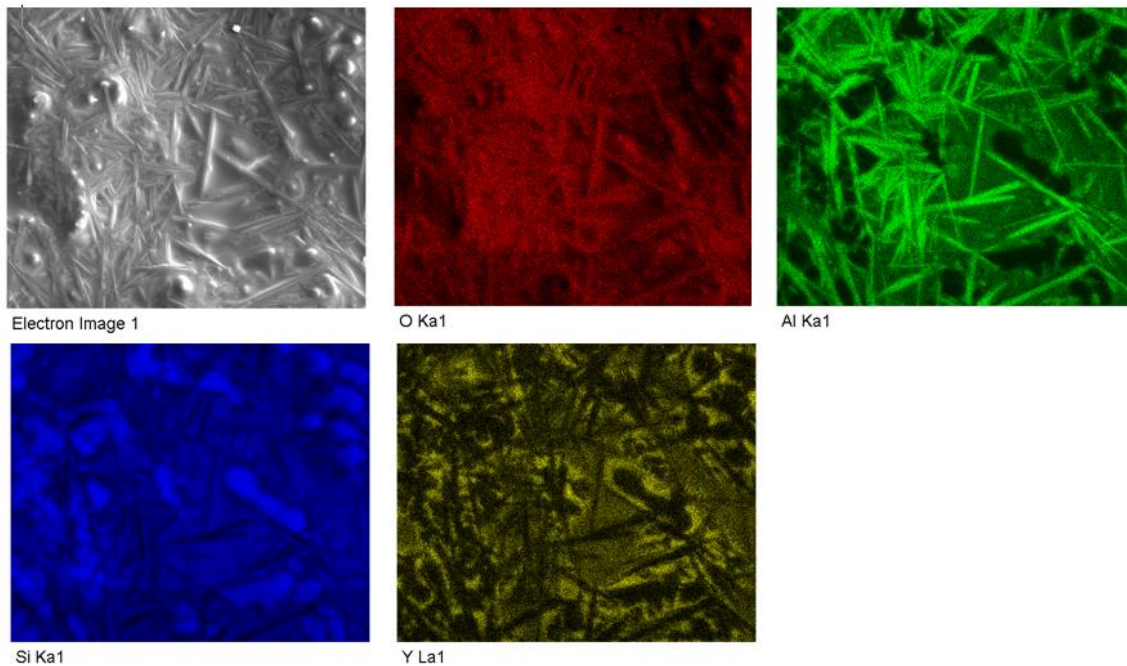
Fig. 4.47: EDX analysis of image b in fig. 4.45

From figs. 4.46 and 4.47, the EDX indeed confirms the claims for the formation of an yttrium-based glassy phase along with the nitrogen bubbles[4]. Oxygen is observed to be a part of the silicon oxynitride and the β phase. Though prominent cristobalite peaks were observed,

this did not lead to the complete decomposition of β SiAlON. Fig. 4.48 illustrates an area consisting of both the ceramic and the oxide scale. An area from this was also tested by EDX analysis, as shown in fig. 4.49.
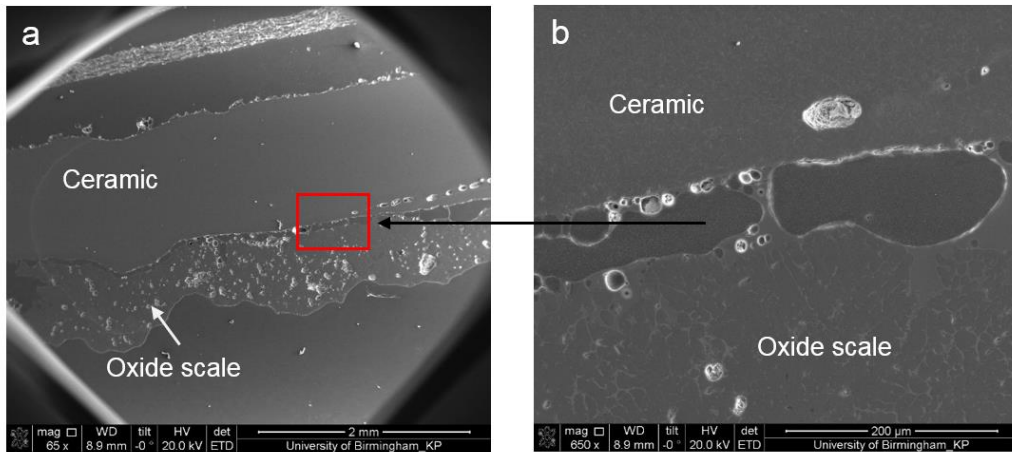
Fig. 4.48: SEM images of the oxidised ceramic, a. a cross-sectional view of the ceramic and the oxidation scale, b. close up of the highlighted area in image a
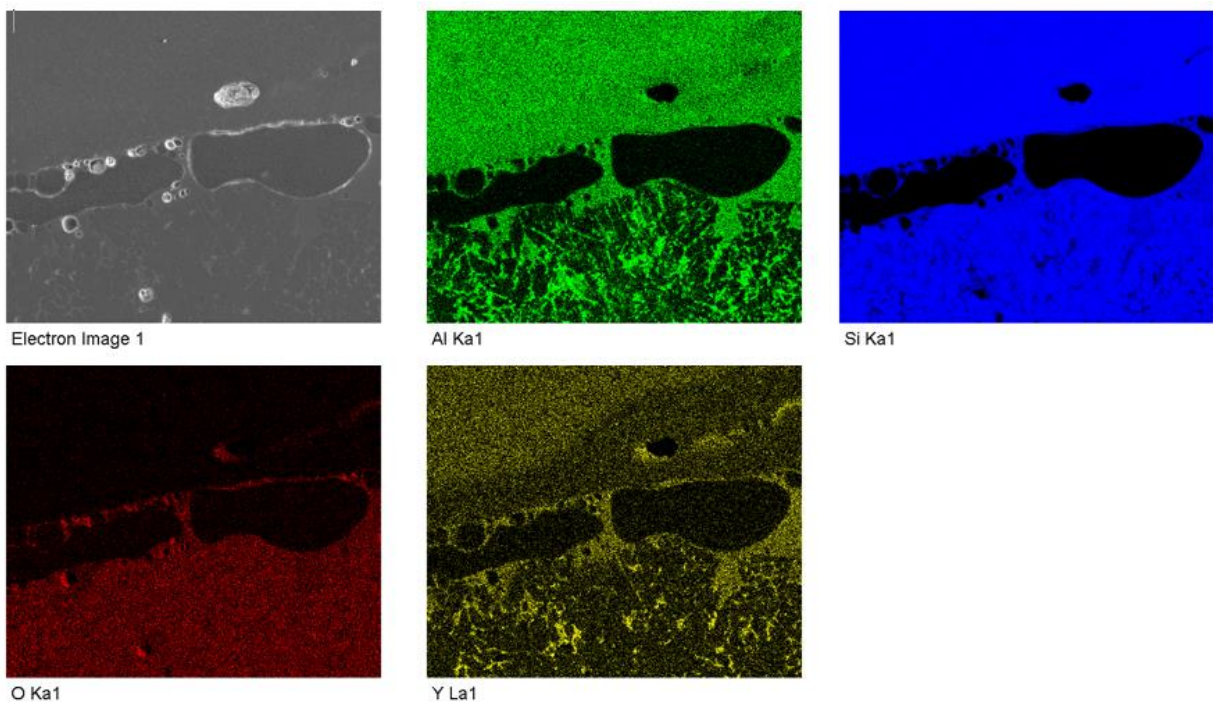
Fig. 4.49: EDX analysis of image b in fig. 4.48
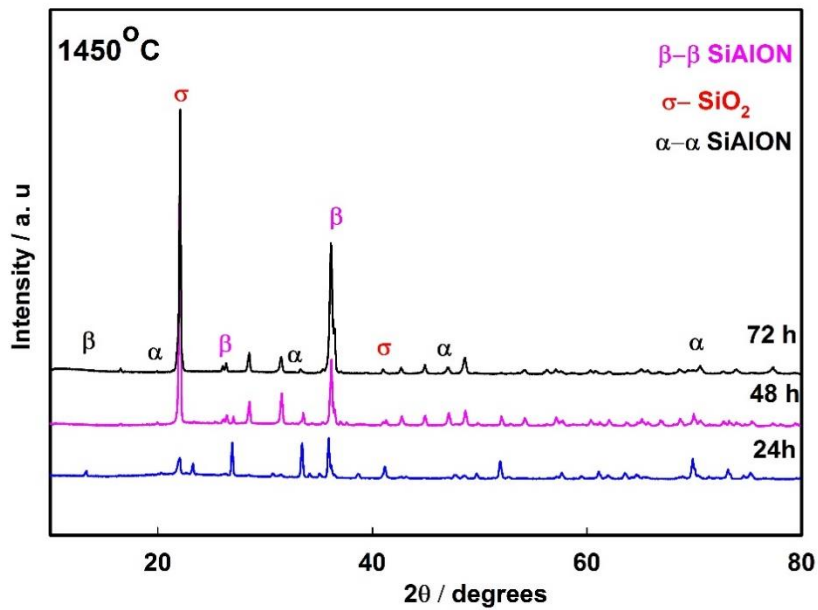
Fig. 4.50: XRD pattern of the oxidised samples at 1450°C

Fig. 4.49 clearly illustrates the abundance of oxygen in the oxide scale and the thicknesses of the oxide scale are shown in table 4.6. To verify these claims, these samples were subjected to X-ray diffraction. Comparisons were made among the samples oxidised for 24, 48 and 72 h, as shown in fig.4.53.

Table 4.6: Oxide scale thickness after oxidation at 1450°C[‡‡‡‡‡]

Temperature / °C	Oxidising time / h	Oxide scale thickness / mm
1450	24	0.7
	48	0.47
	72	0.56

It was observed that the thickness did not increase with time; this is assumed to mean that the oxidation occurred swiftly within the first 24 h after which the oxide layer protected the ceramic underneath. The slightly thinner layers that were measured after the longer time periods could have indicated that some of the oxide layer had spalled off. The XRD patterns

---

[‡‡‡‡‡]Note: Due to the Covid-19 crisis, it wasn't possible to perform the oxide scale thickness measurement for oxidised samples at 1250 and 1350°C

confirm the increasing prominence of cristobalite as the oxidation dwell period increased. The α SiAlON detected in fig. 4.50 was found to decompose to $Y_{0.34}Si_{9.91}Al_{2.09}O_{1.07}$. Additionally, some faint peaks of Si_5AlON_7 were also detected. Fig. 4.51 and 4.52 illustrate examples of the oxidised areas for the dwell times of 48 and 72 h respectively. The SEM images show the increasing grain growth of the oxide scale. The peaks of fig. 4.53 also show the loss of the prominence of the peaks indicating a gradual change from crystalline to an amorphous state.
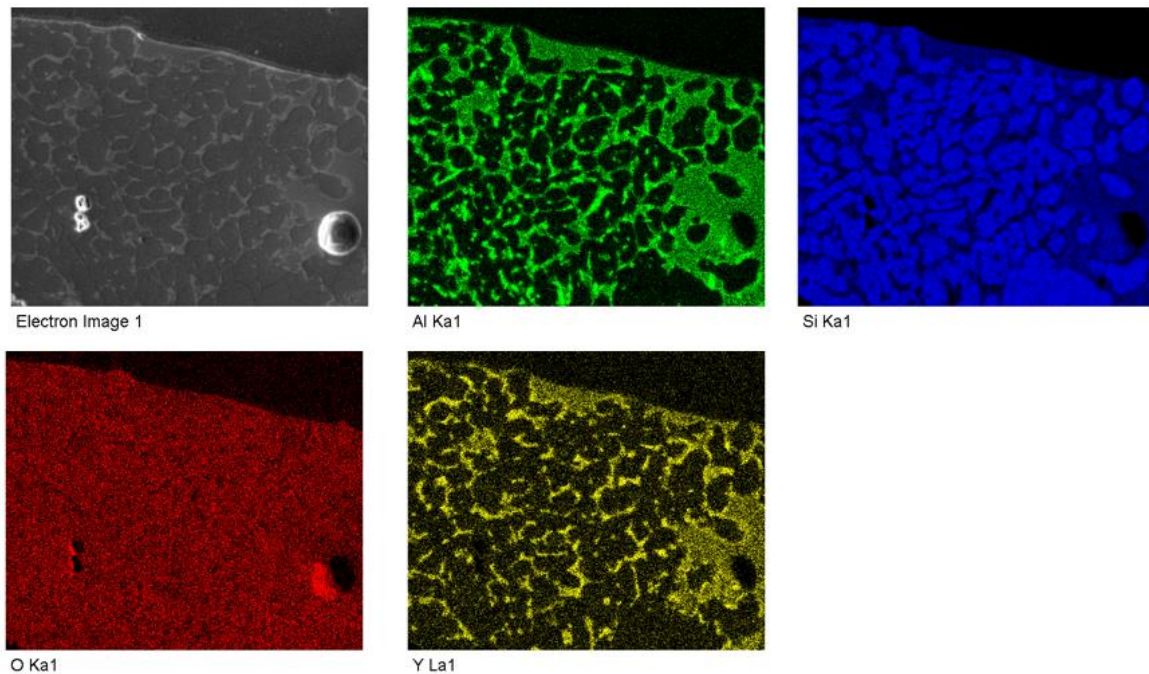
Fig. 4.51: EDX analysis of oxidised surface for 48 h at 1450°C
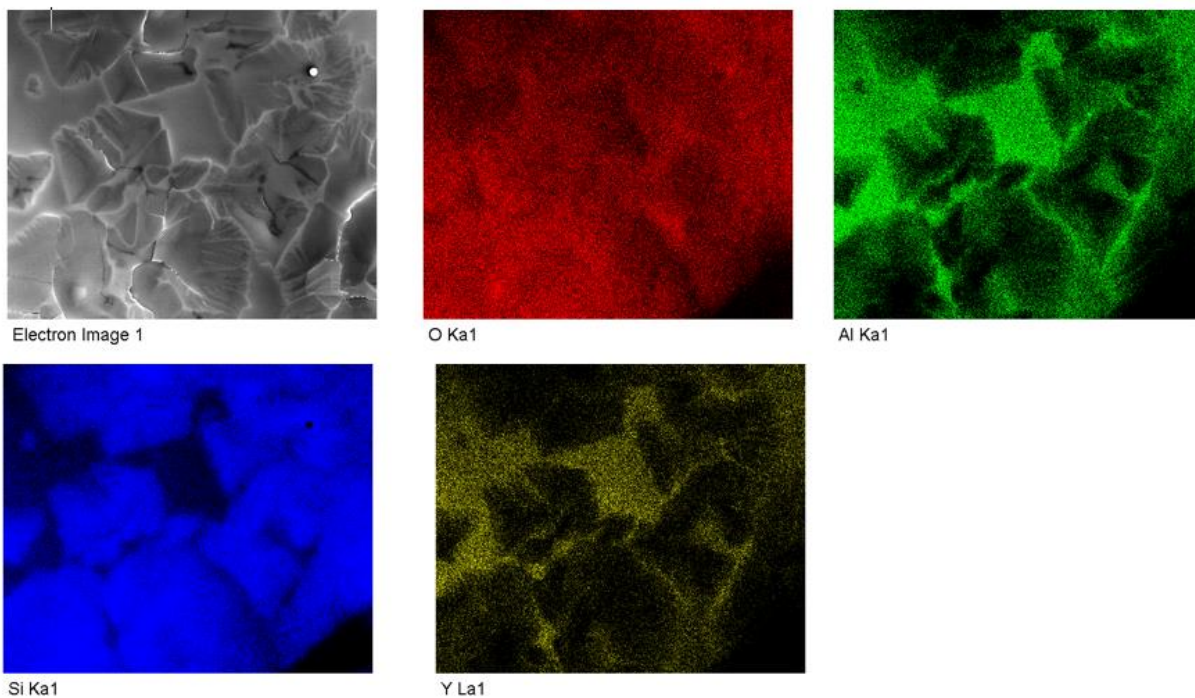
Fig. 4.52: EDX analysis of oxidised surface for 72 h at 1450°C

Fig. 4.51 and 4.52 exhibit clear phase separation. The elements Al and Y can be seen together where Si is the weakest and vice versa. Yttria is an additive especially added to increase the liquid phase in order to aid sintering and it appears that the SiAlON oxidises to form a silica-rich phase (the cristobalite observed by XRD) whilst the Al and Y coexist between the silica-rich grains.

Since oxidation had clearly reached a steady state within 24 h at 1450°C (though no data was obtained on the consequent properties of the ceramic), oxidation tests were also conducted for similar periods at 1350°C and 1250°C. Fig. 4.53 show the diffraction patterns obtained and the mass before and after the oxidation were also measured as shown in table 4.7. The XRD patterns verify the presence of SiO_2; a gradual decrease in the prominence of the peaks with an increase in temperature and dwell time is observed for all the phases except SiO_2. In terms of the mass increase, there is so little data that it is not surprising that it does not exactly fit the normal parabolic rate law of oxidation[1,3,4,65].
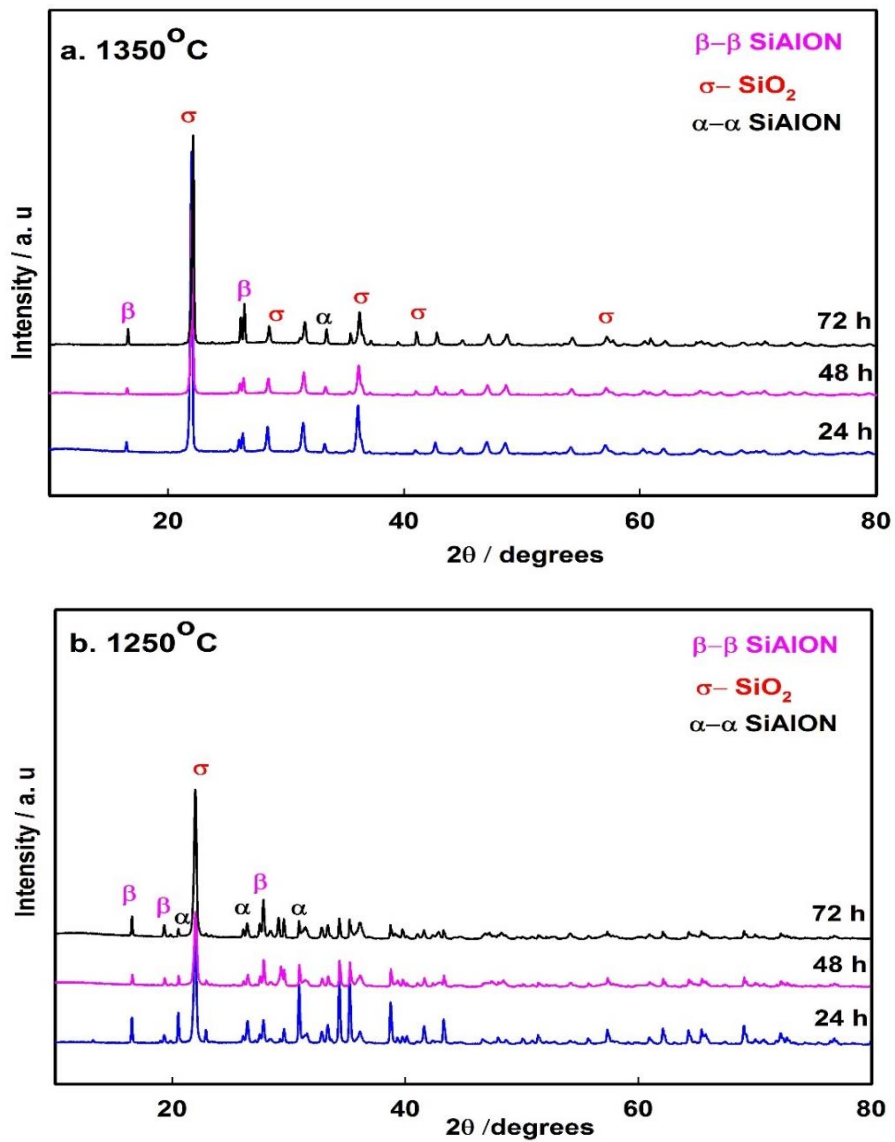
Fig. 4.53: XRD pattern of the oxidised samples at a. 1350ºC and b. 1250ºC

Table 4.7: Overview of the mass increments measured after the oxidation

Temperature / °C	Oxidising time / h	Increase in the mass / g
1250	24	0.002
	48	0.003
	72	0.003
1350	24	0.019
	48	0.034
	72	0.037
1450	24	0.038
	48	0.046
	72	0.052
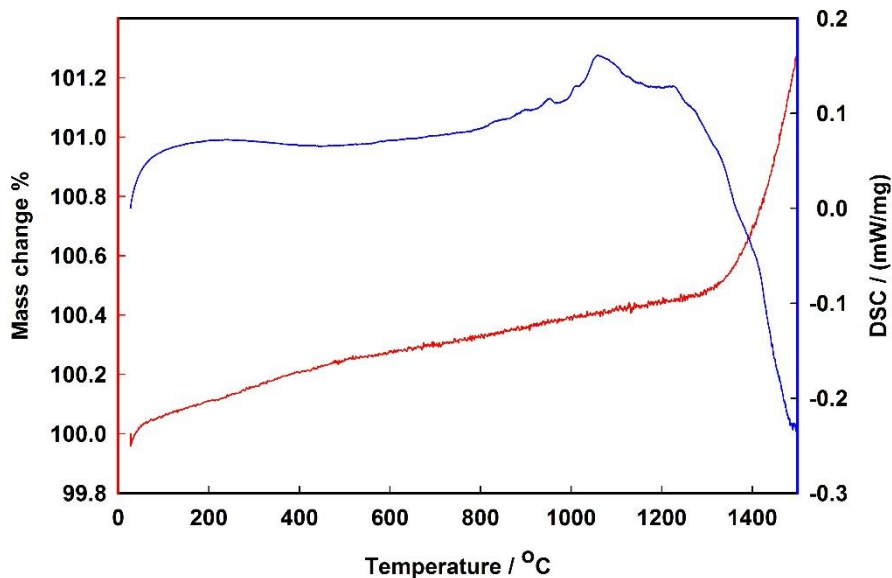
Fig. 4.54: Thermogravimetry analysis of sintered Syalon 050

The TGA-DSC analysis conducted for sintered Syalon 050 indicates a major peak for chemical reaction at ~1100°C, as shown in fig.4.54. This could indicate the onset of degradation of the ceramic with SiO_2 as one of the end products besides nitrogen gas. Also, SiO_2 is one of the earliest products of decomposition at high temperatures[4,11]. Additionally, the parts subjected to the oxidation were noticeably damaged due to the thick scale formation. In this case, the component working at high temperatures could also be expected to deform, which might well hamper its performance.

CHAPTER 5

CONCLUSIONS AND FUTURE WORK

The final chapter is divided into two main sections. The first focuses on the conclusions drawn from the entire research study and also discusses some of the limitations of the fabrication process. The second section discusses and makes some recommendations for future work.

The main aim of this research programme was to assess the potential of fabricating complex-shaped SiAlON components from additively manufactured moulds. The secondary aim was to reduce or eliminate the post processing operations such as polishing and joining. This would help to cut down the number of steps and save time. Following are the main steps that were designed to achieve the aims:

a. Designing and additive manufacturing of complex-shaped moulds

b. Finding a binder system compatible with the ceramic powders

c. Fabrication of green bodies by uniaxial compaction of powders within the moulds.

d. Sintering of the green components to obtain Syalon 050 parts

There was also a fifth activity in which the samples were characterised, both qualitatively and quantitatively, at each step of the process, but whilst this allowed a degree of optimisation of the above four steps it wasn't a process step in its own right. It did, however, allow the overall fabrication process's potential to manufacture complex-shaped structural ceramics to be assessed.

5.1 Conclusions

5.1.1 Additive manufacturing of the moulds and parts

The moulds for all the complex geometries in the current study were additively manufactured using a thermojet polymer material on Solidscape 3Z Pro (by Prodways, New Hampshire, USA).

- The slice thickness was one of the parameters that affected the build quality of the moulds in terms of mechanical strength, resolution. Smaller the slice thickness higher was the resolution of the design. This also implied longer printing time and a higher volume of material consumption compared to using relatively bigger slice thickness. The selection of slice thickness was examined by printing the same design using varying slice thicknesses followed by visual inspection. Moulds that lacked the resolution and broke were discarded. For intricate designs and features, the smallest slice thickness of 6 μm was suitable. On the other hand, no such significant changes were noticed on the relatively bigger moulds such as the engineering gears or turbocharger rotors, with changing slice thicknesses. Therefore, bigger slice thickness was selected for less printing time and low material consumption. However, it was measured that smaller slice thickness led to more surface roughness on edges and grooves in the bigger moulds.

- During mould removal, the powder compact was observed to exhibit capillary action leading to absorption of the mould material. The capillary action was reduced by introducing an interface between the compact and the mould. The interface was a silicone spray (heat resistant up to 300°C). This interface helped to create a better finishing on the green body by prohibiting the capillary action and also smoothing down the irregularities on the mould than the green bodies fabricated without the interface.

- The mould material was tested for its compressional strength to investigate its suitability for the fabrication process. It was found to be strong enough to undergo forces up to 98 N, enclosed in a die. This helped to withstand its pressures during the compaction of the powders However, thinner sections in mould were observed to undergo deformation under pressure. Based on its thermal degradation behaviour, an appropriate heating regime was set to meltdown a majority of the mould material to separate the green body.

5.1.2 The Syalon 050 powders

- The powders were initially characterised to examine the phase content and particle sizes. The majority of the as-received powder was measured to be around 1 μm in size. The powders contained majorly α-Si_3N_4 and Y_2O_3 as a sintering additive. A fine grained final ceramic made up of β SiAlON and yttrium containing refractory glass was expected after the sintering.

- Several binder systems were tried and tested with the ceramic powders for achieving reasonably good adhesion between the particles. The adhesion was critical for the green strength of the complex shapes. Of the different binder systems evaluated, Aquazol® 500 (poly(2-ethyl-2 oxazoline)) was chosen to be used. It was successful to retain the integrity of the complex green shape until the stage of debinding. Majority of the binder degraded by 600°C according to the TGA test. A debinding heat treatment was designed accordingly to prepare the components for sintering.

- The powder mixture containing 5 wt.% Aquazol® 500 and the ceramic powders of Syalon 050 were subjected to powder flowability tests. The resulting mixture was measured to easy flowing with an FF_c of 5 – 6. The flowability coupled with the adhesion was important to make sure that the mould cavity was filled with powder.

- Compacted powders within the moulds were examined using X-ray microCT to determine the extent of the filling. The resulting 3D images showed no voids (due to poor filling) and cracks, both externally and internally. The volume of porosity was also quantified. The green bodies had a density of approximately 55 – 60% of the theoretical value. However, non-uniform edges of the components were observed, which can be attributed to the surface irregularities within the mould.

5.1.3 Sintered Syalon 050 components

- The components were sintered at 1750°C under a constant stream of 5% H_2 + 95% N_2 gas to obtain highly dense ceramics. Nitrogen gas was provided to aid in the densification. Hydrogen gas helped to remove the oxygen away. This also helped to prohibit oxidation during the sintering.

- Dense, complex-shaped components such as engineering gears, sprocket gears, were fabricated with up to 99% of the theoretical density (3.2 g cm^{-3} by the end of the densification process. These components were characterised via visual, physical and chemical means for qualitative analysis. Other shapes such as turbocharger rotors were also manufactured.

- Exterior and interior morphological analysis were conducted on the sintered components which revealed non-uniform surface profiles and roughness over the two sides of the components, with the side that had been in contact with the mould to be much smoother as expected. Ideally, both the sides were expected to be equally smooth. This would facilitate post processing operations such as polishing.

- Components having curved features were found to distort due to the relevant mould features being weaker. This affected the green body negatively. The distortion remained

throughout the sintering. Additionally, some components exhibited the presence of extremely fine layers on one of the sides. This could be attributed to the non-uniform spraying of the interfacial material.

- The components were tested for their hardness and flexural strengths. An approximate value of $HV_{10} = 2545$ which is on par with the values researchers have obtained from their fabrication processes[198]. However, the flexural strength of just 87 MPa was measured. This is a low value was due to the low quality bar samples fabricated from a steel mould.

- Microscopic analysis revealed a mixture of α SiAlON and β SiAlON phases. The α phase was found to be short and equiaxial in shape, whilst the β phase was made up of long elongated, rod-like structures as normal for this ceramic. Ideally, a complete transformation into the β-SiAlON is expected.

- Phase analysis conducted via XRD confirmed the presence of the two phases in almost equal amounts. This indicates the possibility of α SiAlON reprecipitation by the end of sintering. The reason for this possible reprecipitation is unknown and needs to be investigated further. Additionally, some of the refractory glass material was also detected in the pattern as expected.

- An attempt was made to quantify the residual stresses in the components using different methods, however, Syalon 050 proved to be a difficult material to assess using non-destructive methods.

- Finally, oxidation studies were conducted by subjecting sintered Syalon 050 samples to isothermal temperatures of 1250, 1350 and 1450°C for periods of 24, 48 and 72 h. Microscopic analysis coupled with XRD and TGA-DSC studies revealed the onset of thermal degradation started as early as 1100°C in this particular ceramic. A prominent

presence of cristobalite was observed along with grain growth with increasing temperature and time.

5.1.4 Indirect Additive Manufacturing

The current study is been one of the first attempts to fabricate and qualitatively assess ceramic components made from additively manufactured moulds. During the study, some limitations were identified:

- The vacuum power of the AM system was found insufficient to remove the milled debris after printing. This resulted in an extra step of cleaning the moulds before using them.

- The moulds printed were found to lack uniform surface profile and roughness throughout. This fact defeated the aim of reducing post processing polishing.

- Only dimensionally compatible moulds and dies could be used; slightly smaller or larger dies would not fit the mould or would break the mould. So, to fabricate a variety of shapes and sizes of components, custom made dies are required and different capacity presses to supply the required forces to compact the powder.

- The size of the components could be a limitation due to the capacity of the AM unit and the hydraulic press used.

- Separation of the green bodies from larger moulds can be challenging during the mould removal process; the powder beds were often found to be saturated with a high volume of the mould material. Frequent changing of the powder bed during the mould removal process could potentially induce cracks in the green bodies due to the temperature gradients (temp. change between the oven and room). This operation could also increase the chances of damaging the green bodies.

- Thin sections with curved features on the mould were found to distort under the uniaxial forces. There is no alternative to fix this distortion.

- Although this process accommodates fine and intricate geometries, ceramic parts such as the foundry filters can not be fabricated.

- The sintered Syalon 050 component's residual stresses couldn't be calculated using techniques such as XRD or Raman spectroscopy. It requires further exploration of techniques to be used for examining this ceramic.

Based on the results of this study, although complex shaped designs and moulds were easily manufactured via additive manufacturing, the sintered SiAlON components fabricated via uniaxial compaction of powders were of poor quality. A lot of research and investigation has to be conducted to improve the process by modifying the fundamental approach of pressing ceramic powders. One approach could be by using a wet forming method such as gelcasting. There could be a possibility of improving the surface finish of the components. Some of the aspects to be modified to improve the quality of the components are discussed in the next section.

5.2 Further scope of the work

To fabricate good quality structural SiAlON ceramics using the additively manufactured moulds, future work could be conducted along the following lines:

- Studies have been reported which were successful in producing near net shapes via gelcasting using reusable silicone moulds[133]. However, these moulds were made for a part of the component and several parts would require assembly by joining to produce

the complete component. For example, to produce a turbocharge rotor (dia 35 mm), fabrication of individual blades, the base and the shaft is separately possibly. However, the assembly of these components would require additional processes. Instead of pressing dry powders, a gelcasting technique could be developed for the SiAlON ceramic. Gelcasting of SiAlON in the additively manufactured moulds (complete geometry of the component) could produce dense near net shape ceramic parts This would potentially avoid post-processing operations such as joining of the parts. However, extensive studies would be required to study the rheology of the slurries made including aspects such as the viscosity and the zeta potential. Additionally, methods to uniformly dry the gelcasts would have to be looked into. Complexity in the geometry of the mould could leave the surface dry (with/without cracks) with wet internal surfaces.

- An exploration into finding a better sacrificial interfacial material along with a better way of application could be conducted. A uniform layer of the interfacial material would be helpful to smooth the irregularities on the mould, hence avoiding the formation of layers and different height profiles on the surfaces of the ceramic components. An alternative could be the use of a better mould material using other AM units.

- The process of indirect additive manufacturing could be extended to other ceramics such as SiC, Al_2O_3, ZrO_2, etc.

- An attempt to simulate the fabrication process could be utilised to predict the behaviour of the material before the actual fabrication. Although single and multiple material fabrication simulations exist for uniaxial pressing, injection moulding, etc.[§§§§§], only few materials have been worked on and this includes simulations within the same class/state

---

[§§§§§]www.moldex3d.com

of materials. simulations that include the behaviour of multiple class of component materials do not exist. For example, simulating uniaxial pressing of only a few pure materials is possible (as of now). However, simulating uniaxial pressing of a powder mixture (ceramic powders + binder + lubricant) does not exist due to the different behaviours of the components under stresses. Development of such simulation could cut down the laboratory time and help in increasing the yield of successful fabrication techniques. Simulations could also help to predict the presence of residual stresses in the end component.

Finally, indirect additive manufacturing could be a viable industrial fabrication process for complex shaped structural ceramics if :

- A pressureless technique was employed within the moulds to fabricate the green bodies and/or the mould material was a stronger material accompanied by a compatible ceramic material (inert to the mould).

- The additive manufacturing produced uniformly surface finish on the moulds.

- An efficient mould removal process is employed.

- Size of the components is not a limitation.

Bibliography

1. Verma, S., Sahu, M. N. & Jain, P. K. Silicon nitride / SiAlON ceramics -A review. *Indian J. Eng. Mater. Sci.* **8**, 36–45 (2001).

2. Cao, G. Z. & Metselaar, R. α′-Sialon Ceramics: A Review. *Chem. Mater.* **3**, 242–252 (1991).

3. Hampshire, S. Silicon nitride ceramics - review of structure, processing and properties. *J. Achiev. Mater. Manuf. Eng.* **24**, 43–50 (2007).

4. Ekström, T. & Nygren, M. SiAlON Ceramics. *J. Am. Ceram. Soc.* **75**, 259–76 (1992).

5. Mitomo, M. & Tajima, Y. Sintering, properties and applications of silicon nitride and sialon ceramics. *J. Ceram. Soc. Japan. Int. ed.* **99**, 981–991 (1991).

6. Lange, F. F. Silicon nitride polyphase systems: fabrication, microstructure, and properties. *Int. Met. Rev.* **25**, 1–20 (1980).

7. Riley, F. L. Silicon Nitride and Related Materials. *J. Am. Ceram. Soc.* **83**, 245–265 (2004).

8. Sialons for ultraprecision equipment. *Nippon Steel Tech. Rep.* **73**, (1997).

9. Jack, K. H. Sialons and related nitrogen ceramics. *J. Mater. Sci.* **11**, 1135–1158 (1976).

10. Cao, G. Z. Preparation and characterization of alpha'-SiAlON ceramics. *PhD thesis, Tech. Univ. Eindhoven* 1–157 (2017) doi:10.6100/IR350592.

11. Yang, J. F., Ohji, T., Kanzaki, S., Díaz, A. & Hampshire, S. Microstructure and

mechanical properties of silicon nitride ceramics with controlled porosity. *J. Am. Ceram. Soc.* **85**, 1512–1516 (2002).

12. Hampshire, S. & Jack, K. H. Kinetics of Densification and Phase Transformation of Nitrogen Ceramics. *Proc. Br. Ceram. Soc.* 37–49 (1981).

13. Izhevskiy, V. A., Genova, L. A., Bressiani, J. C. & Aldinger, F. Progress in SiAlON ceramics. *J. Eur. Ceram. Soc.* **20**, 2275–2295 (2000).

14. Marchi, J., Guedes e Silva, C. C., Silva, B. B., Bressiani, J. C. & Bressiani, A. H. de A. Influence of additive system (Al2O3- RE2O3, RE = Y, La, Nd, Dy, Yb) on microstructure and mechanical properties of silicon nitride-based ceramics. *Mater. Res.* **12**, 145–150 (2009).

15. Van Krevel, J. W. H., Van Rutten, J. W. T., Mandal, H., Hintzen, H. T. & Metselaar, R. Luminescence properties of terbium-, cerium-, or europium-doped α-sialon materials. *J. Solid State Chem.* **165**, 19–24 (2002).

16. Guedes-Silva, C. C., De Souza Carvalho, F. M. H. & Bressiani, J. C. Effect of rare-earth oxides on properties of silicon nitride obtained by normal sintering and sinter-HIP. *J. Rare Earths* (2012) doi:10.1016/S1002-0721(12)60201-4.

17. Millán, A. J., Nieto, M. I. & Moreno, R. Aqueous injection moulding of silicon nitride. *J. Eur. Ceram. Soc.* (2000) doi:10.1016/S0955-2219(00)00118-7.

18. Nagel, A., Petzow, G. & Greil, P. Rheology of aqueous silicon nitride suspensions. *J. Eur. Ceram. Soc.* (1989) doi:10.1016/0955-2219(89)90041-1.

19. Albano, M. P. & Garrido, L. B. Processing of Concentrated Aqueous Silicon Nitride Slips by Slip Casting. *J. Am. Ceram. Soc.* **81**, 837–844 (1998).

20. Yu, J., Wang, H., Zhang, J., Zhang, D. & Yan, Y. Gelcasting preparation of porous silicon nitride ceramics by adjusting the content of monomers. *J. Sol-Gel Sci. Technol.* **53**, 515–523 (2010).

21. Wan, T. *et al.* The microstructure and mechanical properties of porous Silicon nitride ceramics prepared via novel aqueous gelcasting. *Int. J. Appl. Ceram. Technol.* **12**, 932–938 (2015).

22. Ganesh, I. & Sundararajan, G. Hydrolysis-induced aqueous gelcasting of beta-SiAlON-SiO2 ceramic composites: The effect of AlN additive. *J. Am. Ceram. Soc.* **93**, 3180–3189 (2010).

23. Wan, T. *et al.* Fabrication of porous Si 3 N 4 ceramics through a novel gelcasting method. *Mater. Lett.* **133**, 190–192 (2014).

24. Rabinovich, E. M., Leitner, S. & Golden Berg, A. Slip casting of silicon nitride for pressureless sintering. *J. Mater. Sci.* **17**, 323–328 (1982).

25. Omatete, O. O., Janney, M. a. & Nunn, S. D. Gelcasting: From laboratory development toward industrial production. *J. Eur. Ceram. Soc.* **17**, 407–413 (1997).

26. Su, B., Dhara, S. & Wang, L. Green ceramic machining: A top-down approach for the rapid fabrication of complex-shaped ceramics. *J. Eur. Ceram. Soc.* **28**, 2109–2115 (2008).

27. Hyuga, H., Kondo, N. & Ohji, T. Chapter 9 - Green Manufacturing of Silicon Nitride Ceramics. in (eds. Singh, M., Ohji, T. & Asthana, R. B. T.-G. and S. M. of A. M.) 223–243 (Elsevier, 2016). doi:https://doi.org/10.1016/B978-0-12-411497-5.00009-6.

28. Murr, L. E. A Metallographic Review of 3D Printing/Additive Manufacturing of Metal

and Alloy Products and Components. *Metallogr. Microstruct. Anal.* **7**, 103–132 (2018).

29. Babu, S. S. & Goodridge, R. Additive manufacturing. *Mater. Sci. Technol. (United Kingdom)* **31**, 881–883 (2015).

30. Ligon, S. C., Liska, R., Stampfl, J., Gurr, M. & Mülhaupt, R. Polymers for 3D Printing and Customized Additive Manufacturing. *Chem. Rev.* **117**, 10212–10290 (2017).

31. Gupta, M. 3D printing of metals. *Metals (Basel).* **7**, 3–4 (2017).

32. ProtoLabs. Materials Matter: Selecting the Right Material for 3D Printing. 14 (2017).

33. Vaezi, M., Chianrabutra, S., Mellor, B. & Yang, S. Multiple material additive manufacturing - Part 1: A review. *Virtual Phys. Prototyp.* **8**, 19–50 (2013).

34. Scheithauer, U., Bergner, A., Schwarzer, E., Richter, H. J. & Moritz, T. Studies on thermoplastic 3D printing of steel-zirconia composites. *J. Mater. Res.* **29**, 1931–1940 (2014).

35. Costa, E. C. E., Duarte, J. P. & Bártolo, P. A review of additive manufacturing for ceramic production. *Rapid Prototyp. J.* **23**, 954–963 (2017).

36. Shahzad, K., Deckers, J., Zhang, Z., Kruth, J. P. & Vleugels, J. Additive manufacturing of zirconia parts by indirect selective laser sintering. *J. Eur. Ceram. Soc.* **34**, 81–89 (2014).

37. Zhang, M. & Yang, L. Ceramic Product Forming Technologies Research Based on 3D Printing. *IEEE Access* **4**, 9345–9349 (2016).

38. Khan, S. F., German, M. J. & Dalgarno, K. W. Indirect Additive Manufacturing Processing of Poly-Lactide-co-Glycolide. *Appl. Mech. Mater.* **754**–**755**, 985–989

(2015).

39. Khan, S. F., W. Dalgarno, K. & Siregar, R. A. Indirect Additive Manufacturing (AM) of Apatite-Wollastonite (A-W) Glass-Ceramic for Medical Implants. *Appl. Mech. Mater.* **786**, 354–360 (2015).

40. Almonti, D. & Ucciardello, N. Design and thermal comparison of random structures realized by indirect additive manufacturing. *Materials (Basel).* **12**, (2019).

41. Kingery, W. D. Introduction. in *Ceramic Materials: Science and Engineering* 3–14 (Springer New York, 2007). doi:10.1007/978-0-387-46271-4_1.

42. Schoenung, J. M. Structural Ceramics. *Encycl. Mater. Sci. Technol.* 8921–8926 (2001) doi:10.1016/B0-08-043152-6/01605-3.

43. Okada, A. Automotive and industrial applications of structural ceramics in Japan. *J. Eur. Ceram. Soc.* **28**, 1097–1104 (2008).

44. Asanabe, S. Applications of ceramics for tribological components. *Tribol. Int.* **20**, 355–364 (1987).

45. Jahanmir, S. Tribological Applications for Advanced Ceramics. *MRS Proc.* **140**, 285 (1988).

46. Sukumaran, V. G. & Bharadwaj, N. Ceramics in dental applications. *Trends Biomater. Artif. Organs* **20**, 7–11 (2006).

47. Kingery, W. D., Bowen, H. K. & D, U. *Introduction to ceramics.* (Wiley, 1976).

48. Bergmann, C. P. & Stumpf, A. Microstructure of Ceramic Materials. *65th Annual Meeting of the American Ceramic Society* vol. 75 31–44 (1963).

49. Pask, J. A. Structural Ceramics. *J. Mater. Eng.* **11**, 267–2574 (1989).

50. Lange, F. F. Relation Between Strength, Fracture Energy, and Microstructure of Hot-Pressed Si3N4. *J. Am. Ceram. Soc.* **56**, 518–522 (1973).

51. Kim, M. S. *et al.* Microstructure and mechanical properties of β-SiAlON ceramics fabricated using self-propagating high-temperature synthesized β-SiAlON powder. *J. Korean Ceram. Soc.* **54**, 292–297 (2017).

52. Qingrui YinBinghe ZhuHuarong Zeng. *Microstructure and properties of functional ceramics.* (Springer, Berlin, Heidelberg, 2009). doi:https://doi.org/10.1007/978-3-642-01694-3_1.

53. Feng, L., Fahrenholtz, W. G., Hilmas, G. E., Watts, J. & Zhou, Y. Densification, microstructure, and mechanical properties of ZrC–SiC ceramics. *J. Am. Ceram. Soc.* **102**, 5786–5795 (2019).

54. Evans, J. R. G. Seventy ways to make ceramics. **28**, 1421–1432 (2008).

55. Ring, T. A. Ceramic Powder Synthesis. in *Fundamentals of Ceramic Powder Processing and Synthesis* 81–83 (1996). doi:10.1016/b978-012588930-8/50004-8.

56. Roy, R., Komarneni, S. & Roy, D. M. Multi-Phasic Ceramic Composites made by Sol-Gel Technique. *MRS Proc.* **32**, 347 (1984).

57. Cano, I. G., Borovinskaya, I. P., Rodriguez, M. A. & Grachev, V. V. Effect of dilution and porosity on self-propagating high-temperature synthesis of silicon nitride. *J. Am. Ceram. Soc.* **85**, 2209–2211 (2002).

58. Jiang, J. A new synthesis method of α-silicon nitride powder-reductive combustion synthesis from silicon and silicon dioxide. *J. Am. Ceram. Soc.* **92**, 3095–3097 (2009).

59. Won, H. I., Won, C. W., Nersisyan, H. H. & Yoon, K. S. Salt-assisted combustion synthesis of silicon nitride with high α-phase content. *J. Alloys Compd.* **496**, 656–659 (2010).

60. Zakorzhevskii, V. V & Borovinskaya, I. P. Combustion synthesis of silicon nitride using ultrafine silicon powders. *Powder Metall. Met. Ceram.* **48**, 375–380 (2009).

61. Laurie, J. *et al.* Colloidal suspensions for the preparation of ceramics by a freeze casting route. *J. Non. Cryst. Solids* (1992) doi:10.1016/S0022-3093(05)80637-4.

62. Sakka, S. *Sol-Gel Process and Applications. Handbook of Advanced Ceramics: Materials, Applications, Processing, and Properties: Second Edition* (Elsevier, 2013). doi:10.1016/B978-0-12-385469-8.00048-4.

63. Bitterlich, B. *et al.* Formation of silicon nitride bonded silicon carbide by aqueous gelcasting. *J. Eur. Ceram. Soc.* **349**, 20–28 (2017).

64. Hector, A. L. Synthesis and processing of silicon nitride and related materials using preceramic polymer and non-oxide sol-gel approaches. *Coord. Chem. Rev.* (2016) doi:10.1016/j.ccr.2016.05.009.

65. Shahien, M., Radwan, M., Kirihara, S., Miyamoto, Y. & Sakurai, T. Combustion synthesis and sintering of β-sialon ceramics (z = 2). *Zair. Soc. Mater. Sci. Japan* **57**, 1248–1252 (2008).

66. Agrafiotis, C. C., Lis, J., Puszynski, J. A. & Hlavacek, V. Combustion synthesis of Silicon nitride- Silicon carbide composites. **17**, 3514–3517 (1990).

67. Tanaka, I., Pezzotti, G., Okamoto, T., Miyamoto, Y. & Koizumi, M. Hot Isostatic Press Sintering and Properties of Silicon Nitride without Additive. *J. Am. Ceram. Soc.* **72**,

1656–1660 (1989).

68. Hirao, K., Miyamoto, Y. & Koizumi, M. Synthesis of Silicon Nitride by a Combustion Reaction under High Nitrogen Pressure. *J. Am. Ceram. Soc.* **69**, C-60-C-61 (1986).

69. Rahaman, M. N. Ceramic processing and sintering. *Int. Mater. Rev.* **41**, 36–37 (1996).

70. Yuping, Z., Dongliang, J. & Greil, P. Tape casting of aqueous Al2O3 slurries. *J. Eur. Ceram. Soc.* (2000) doi:10.1016/S0955-2219(00)00043-1.

71. Kristoffersson, A., Roncari, E. & Galassi, C. Comparison of different binders for water-based tape casting of alumina. *Doktorsavhandlingar vid Chalmers Tek. Hogsk.* (1999) doi:10.1016/S0955-2219(98)00165-4.

72. Gilissen, R., Erauw, J. P., Smolders, A., Vanswijgenhoven, E. & Luyten, J. Gelcasting, a near net shape technique. *Mater. Des.* **21**, 251–257 (2000).

73. Bresciani, A. Shaping in Ceramic Technology - An Overview. in *Extrusion in Ceramics* (ed. Händle, F.) 13–33 (Springer Berlin Heidelberg, 2007). doi:10.1007/978-3-540-27102-4_2.

74. Sepulveda, P. & Binner, J. G. P. Evaluation of the in situ polymerization kinetics for the gelcasting of ceramic foams. *Chem. Mater.* **13**, 3882–3887 (2001).

75. Davies, J. & Binner, J. G. P. The role of ammonium polyacrylate in dispersing concentrated alumina suspensions. *J. Eur. Ceram. Soc.* **20**, 1539–1553 (2000).

76. Binner, J. G. P., McDermott, A. M. & Yin, Y. In-situ coagulation moulding of ceramic suspensions. *Key Eng. Mater.* **264–268**, 293–296 (2004).

77. Binner, J. G. P. & McDermott, A. M. In-situ acidification of electrosterically dispersed

alumina suspensions: Effect of coagulant structure. *J. Mater. Sci.* **41**, 1893–1903 (2006).

78.   Binner, J. G. P. & McDermott, A. M. Rheological characterisation of ammonium polyacrylate dispersed, concentrated alumina suspensions. *Ceram. Int.* **32**, 803–810 (2006).

79.   Kaiser, A. Hydraulic pressing of advanced ceramics. *CFI Ceram. Forum Int.* (2007).

80.   Freedman, M. & Sanders, W. A. Slurry-pressing consolidation of silicon nitride Slurry-Pressing Consolidation of Silicon Nitride. (2016).

81.   Akimov, G. Y. Cold isostatic pressing as a method for fabricating ceramic products with high physicomechanical properties. *Refract. Ind. Ceram.* **39**, 283–287 (1998).

82.   Atkinson, H. V. & Davies, S. Fundamental aspects of hot isostatic pressing: An overview. *Metall. Mater. Trans. A Phys. Metall. Mater. Sci.* **31**, 2981–3000 (2000).

83.   Occhionero, M. A. & Halloran, J. W. The Influence of Green Density upon Sintering. in *Materials Science Research: Volume 16 Sintering and Heterogeneous Catalysis* (eds. Kuczynski, G. C., Miller, A. E. & Sargent, G. A.) 89–102 (Springer US, 1984). doi:10.1007/978-1-4613-2761-5_7.

84.   Robinson, S. K., Paul, M. R. & Industries, V. Debinding and sintering solutions for metals and ceramics Proper removal of organic binders and lubricants is critical if the required properties are to. *Www.Metal-Powder.Net* (2001).

85.   Piotter, V., Bauer, W., Benzler, T. & Emde, A. Injection molding of components for microsystems. *Microsyst. Technol.* **7**, 99–102 (2001).

86.   German, R. M. *Sintering Practice. Sintering: from Empirical Observations to Scientific*

Principles (2014). doi:10.1016/b978-0-12-401682-8.00015-x.

87.   German, R. M. History of Sintering. *Sinter. from Empir. Obs. to Sci. Princ.* 13–40 (2014) doi:10.1016/b978-0-12-401682-8.00002-1.

88.   Bernard, G. Processes involved in sintering. *Powder Metall.* **2**, 86–103 (1959).

89.   German, R. M. *Thermodynamic and Kinetic Treatments. Sintering: from Empirical Observations to Scientific Principles* (2014). doi:10.1016/b978-0-12-401682-8.00007-0.

90.   Blendell, J. E. Solid-state Sintering. *Encycl. Mater. Sci. Technol.* 8745–8750 (2001) doi:10.1016/B0-08-043152-6/01564-3.

91.   German, R. M. Green body homogeneity effects on sintered tolerances. *Powder Metall.* **47**, 157–160 (2004).

92.   Johnson, J. L. & German, R. M. Theoretical modeling of densification during activated solid-state sintering. *Metall. Mater. Trans. A Phys. Metall. Mater. Sci.* **27**, 441–450 (1996).

93.   German, R. M. Sintering. *Encycl. Mater. Sci. Technol.* 8641–8643 (2001) doi:10.1016/B0-08-043152-6/01542-4.

94.   Kuczynski G.C. Model Experiments and the Theory of Sintering. in *Sintering, key papers* 501–508 (Springer, Dordrecht, 1990). doi:https://doi.org/10.1007/978-94-009-0741-6_32.

95.   Coble, R. L. Sintering Alumina: Effect of Atmospheres. *J. Am. Ceram. Soc.* (1955) doi:10.1111/j.1151-2916.1962.tb11099.x.

96. Cob. Progress in Sintering Theory. In: Kuczynski G.C. (eds) Sintering and Related Phenomena. Materials Science Research, vol 6. Springer, Boston, MA. in (Springer, Boston, MA, 1973). doi:https://doi.org/10.1007/978-1-4615-8999-0_13.

97. Johnson, D. L. & Cutler, I. B. Diffusion Sintering: I, Initial Stage Sintering Models and Their Application to Shrinkage of Powder Compacts. *J. Am. Ceram. Soc.* **46**, 541–545 (1963).

98. Wong, B. & Pask, J. A. Models for Kinetics of Solid State Sintering. *J. Am. Ceram. Soc.* **62**, 138–141 (1979).

99. Kraft, T. & Riedel, H. Numerical simulation of solid state sintering; model and application. *J. Eur. Ceram. Soc.* (2004) doi:10.1016/S0955-2219(03)00222-X.

100. Wang, Y. U. Computer modeling and simulation of solid-state sintering: A phase field approach. *Acta Mater.* (2006) doi:10.1016/j.actamat.2005.10.032.

101. Braginsky, M., Tikare, V. & Olevsky, E. Numerical simulation of solid state sintering. in *International Journal of Solids and Structures* (2005). doi:10.1016/j.ijsolstr.2004.06.022.

102. German, R. M. *Sintering With a Liquid Phase. Sintering: from Empirical Observations to Scientific Principles* (2014). doi:10.1016/b978-0-12-401682-8.00009-4.

103. Kingery, W. D. & Narasimhan, M. D. Densification during sintering in the presence of a liquid phase. II. Experimental. *J. Appl. Phys.* **30**, 307–310 (1959).

104. Kwon, O. H. & Messing, G. L. A theoretical analysis of solution-precipitation controlled densification during liquid phase sintering. *Acta Metall. Mater.* **39**, 2059–2068 (1991).

105. German, R. M., Suri, P. & Park, S. J. Review: Liquid phase sintering. *J. Mater. Sci.*

44, 1–39 (2009).

106. Kingery, W. D., Woulbroun, J. M. & Charvat, F. R. Effects of Applied Pressure on Densification During Sintering in the Presence of a Liquid Phase. *J. Am. Ceram. Soc.* **46**, 391–395 (1963).

107. Kingery, W. D. & Narasimhan, M. D. Densification during sintering in the presence of a liquid phase. II. Experimental. *J. Appl. Phys.* **30**, 307–310 (1959).

108. German, R. M. *Sintering With External Pressure. Sintering: from Empirical Observations to Scientific Principles* (2014). doi:10.1016/b978-0-12-401682-8.00010-0.

109. Zhou, C. R., Yu, Z. B. & Krstic, V. D. Pressureless sintered self-reinforced Y-α-SiAlON ceramics. *J. Eur. Ceram. Soc.* **27**, 437–443 (2007).

110. Johnson, J. L. & German, R. M. Solid-state contributions to densification during liquid-phase sintering. *Metall. Mater. Trans. B Process Metall. Mater. Process. Sci.* **27**, 901–909 (1996).

111. Pollinger, J. P. Progress in fabrication of silicon nitride structural components for turbomachinery applications. *ASME 1996 Int. Gas Turbine Aeroengine Congr. Exhib.* V005T13A021-V005T13A021 (1996) doi:10.1115/96-GT-347.

112. Wang, C.-M., Pan, X., Rühle, M., Riley, F. L. & Mitomo, M. Silicon nitride crystal structure and observations of lattice defects. *J. Mater. Sci.* **31**, 5281–5298 (1996).

113. Professor Riedel, R. Handbook of Ceramic Hard Materials. in (ed. Professor Riedel, R.) (Wiley, 2000). doi:10.1002/9783527618217.

114. Jennings, H. M. & Richman, M. H. Structure, formation mechanisms and kinetics of

reaction-bonded silicon nitride. *J. Mater. Sci.* **11**, 2087–2098 (1976).

115. Chatfield, C., Ekström, T. & Mikus, M. Microstructural investigation of alpha-beta yttrium sialon materials. *J. Mater. Sci.* **21**, 2297–2307 (1986).

116. Hampshire, S., Park, H. K., Thompson, D. P. & Jack, K. H. α′-Sialon ceramics. *Nature* **274**, 880–882 (1978).

117. Deeley, G. G., Herbert, J. M. & Moore, N. C. Dense Silicon Nitride. *Powder Metall.* **5899**, 145–151 (1961).

118. Lee, D., Kang, S. L., Petzow, G. & Yoon, D. N. Effect of α to β (β') Phase Transformation on the Sintering of Silicon Nitride Ceramics. *J. Am. Ceram. Soc.* **73**, 767–769 (1990).

119. Ziegler, G., Heinrich, J. & Wotting, G. Relationships between processing, microstructure and properties of dense and reaction-bonded silicon nitride. *J. Mater. Sci.* **22**, 3041–3086 (1987).

120. Mitomo, M. Pressure sintering of Si3N4. *J. Mater. Sci.* **11**, 1103–1107 (1976).

121. German, R. M. Rapid Heating Approaches. *Sinter. from Empir. Obs. to Sci. Princ.* 387–412 (2014) doi:10.1016/b978-0-12-401682-8.00012-4.

122. German, R. M. Future Prospects for Sintering. *Sinter. from Empir. Obs. to Sci. Princ.* 513–526 (2014) doi:10.1016/b978-0-12-401682-8.00016-1.

123. Biswas, S. K. & Riley, F. L. Gas pressure sintering of silicon nitride - current status. *Mater. Chem. Phys.* **67**, 175–179 (2001).

124. Greskovich, C. Preparation of High-Density Si3N4 by a Gas-Pressure Sintering

Process. *J. Am. Ceram. Soc.* **64**, 725–730 (1981).

125. Stuijits, A. L. Syntheis of Materials From Powders By Sintering. *Annu. Rev.* (1973).

126. Terwilliger, G. R. & Lange, F. F. Pressureless sintering of Si3N4. *J. Mater. Sci.* **10**, 1169–1174 (1975).

127. Watanabe, K., Masuda, M., Ozawa, T., Matsui, M. & Matsuhiro, K. Research and Development of Ceramic Turbine Wheels.

128. Kovziridze, Z. *et al.* Obtaining of SiAlON Composite via Metal-Thermal and Nitrogen Processes in the SiC-Si-Al-Geopolymer System. *J. Electron. Cool. Therm. Control* **7**, 103–122 (2017).

129. Thompson D.P., Korgul P., H. A. The Structural Characterisation of Sialon Polytypoids. in *Progress in nitrogen ceramics* (ed. Riley, F. L.) 61–74 (Springer, Dordrecht, 1983). doi:https://doi.org/10.1007/978-94-009-6851-6_4.

130. Wang, P. L., Jia, Y. X. & Sun, W. Y. Fabrication of 15R AlN-polytypoid ceramics. *Mater. Lett.* **41**, 78–82 (1999).

131. Mandal, H., Thompson, D. P. & Ekström, T. Reversible α⇌ sialon transformation in heat-treated sialon ceramics. *J. Eur. Ceram. Soc.* **12**, 421–429 (1993).

132. Arias, A. Pressureless sintered SiAlON with low amounts of sintering aid. *J. Mater. Sci.* **14**, 1353–1360 (1979).

133. Liu, G. *et al.* Gel casting of sialon ceramics based on water soluble epoxy resin. *Ceram. Int.* **41**, 11534–11538 (2015).

134. Amin, M., Ehsani, N. & Mozafarinia, R. Synthesis Ca-α-SiAlON powder by

carbothermal reduction nitridation of colloidal sol-gel derived powder precursor. *Ceram. Int.* **45**, 17567–17573 (2019).

135. Konegger, T., Potzmann, R., Puchberger, M. & Liersch, A. Matrix–filler interactions in polysilazane-derived ceramics with Al 2 O 3 and ZrO 2 fillers. *J. Eur. Ceram. Soc.* **31**, 3021–3031 (2011).

136. Lan, Y. L. *et al.* Mechanical properties and thermal conductivity of dense β-SiAlON ceramics fabricated by two-stage spark plasma sintering with Al2O3-AlN-Y2O3 additives. *J. Eur. Ceram. Soc.* **40**, 12–18 (2019).

137. MacKenzie, K. J. D. *et al.* Kinetics and mechanism of thermal oxidation of sialon ceramic powders. *Thermochim. Acta* **318**, 91–100 (1998).

138. Corapcioglu, G. & Kurama, S. Oxidation behaviour and kinetics of α-SiAlON ceramics. *Mater. High Temp.* **26**, 145–151 (2009).

139. Baskut, S. & Turan, S. Microstructure and Oxidation Behavior Of SiAlON Ceramics. in *16th International Materials Symposium IMSP'2016* (2016).

140. Yu, J., Du, H., Shuba, R. & Chen, I.-W. Dopant-dependent oxidation behavior of - SiAlON ceramics. *J. Mater. Sci.* **39**, 4855–4860 (2004).

141. Gunchenko, V. A., Pavlikov, V. N. & Trunov G.V. Kinetics and mechanism of oxidation of beta SiAlONs. *Poroshkovaya Metall.* **6**, 69–73 (1988).

142. Vaezi, M., Chianrabutra, S., Mellor, B. & Yang, S. Multiple material additive manufacturing - Part 1: A review: This review paper covers a decade of research on multiple material additive manufacturing technologies which can produce complex geometry parts with different materials. *Virtual Phys. Prototyp.* **8**, 19–50 (2013).

143. Gardan, J. Additive manufacturing technologies: State of the art and trends. *Int. J. Prod. Res.* **54**, 3118–3132 (2016).

144. Stucker, B. Additive Manufacturing Technologies: Technology Introduction and Business Implications. *Front. Eng. 2011 Reports Leading-Edge Eng. from 2011 Symp.* **0**, pages 1-9 (2012).

145. ASTM, Committee, F. 9. A. M. T. (Sponsoring & Committee), F. 9. A. M. T. (Sponsoring. Standard Terminology for Additive Manufacturing Technologies - F2792 − 12a. *Stand. Terminol. Addit. Manuf. Technol.* **10**, (2013).

146. Guessasma, S., Zhang, W., Zhu, J., Belhabib, S. & Nouri, H. Challenges of additive manufacturing technologies from an optimisation perspective. *Int. J. Simul. Multidiscip. Des. Optim.* **6**, A9 (2015).

147. Kumbhar, N. N. & Mulay, A. V. Post Processing Methods used to Improve Surface Finish of Products which are Manufactured by Additive Manufacturing Technologies: A Review. *J. Inst. Eng. Ser. C* **99**, 481–487 (2018).

148. Sikder, S., Barari, A. & Kishawy, H. A. Effect of Adaptive Slicing on Surface Integrity in Additive Manufacturing. (2014) doi:10.1115/detc2014-35559.

149. Leirmo, T. S. & Martinsen, K. Evolutionary algorithms in additive manufacturing systems: Discussion of future prospects. *Procedia CIRP* **81**, 671–676 (2019).

150. Busachi, A. *et al.* Defining Next-Generation Additive Manufacturing Applications for the Ministry of Defence (MoD). *Procedia CIRP* **55**, 302–307 (2016).

151. Guo, N. & Leu, M. C. Additive manufacturing: Technology, applications and research needs. *Front. Mech. Eng.* **8**, 215–243 (2013).

152. Rajak, N. K. & Kaimkuriya, P. A. Design and Development of Honeycomb Structure for Additive Manufacturing. *Int. J. Trend Sci. Res. Dev.* **Volume-2**, 1198–1203 (2018).

153. Naidu, B. V. V. & Kumar, G. D. Additive Manufacturing of Honeycomb Structure and Analysis of Infill and Material Characteristics. *Int. J. Sci. Res. Rev.* **7**, 226–234 (2018).

154. Deckers, J., Vleugels, J. & Kruth, J. P. Additive manufacturing of ceramics: A review. *J. Ceram. Sci. Technol.* **5**, 245–260 (2014).

155. Sahasrabudhe, H., Bose, S. & Bandyopadhyay, A. Chapter 17 - Laser-Based Additive Manufacturing Processes. in *Woodhead Publishing Series in Welding and Other Joining Technologies* (ed. Lawrence, J. B. T.-A. in L. M. P. (Second E.) 507–539 (Woodhead Publishing, 2018). doi:https://doi.org/10.1016/B978-0-08-101252-9.00017-0.

156. Schmidt, M. *et al.* Laser based additive manufacturing in industry and academia. *CIRP Ann.* **66**, 561–583 (2017).

157. Balla, V. K., Bose, S. & Bandyopadhyay, A. Processing of bulk alumina ceramics using laser engineered net shaping. *Int. J. Appl. Ceram. Technol.* **5**, 234–242 (2008).

158. Kumar, N., Jain, P. K., Tandon, P. & Pandey, P. M. Extrusion-based additive manufacturing process for producing flexible parts. *J. Brazilian Soc. Mech. Sci. Eng.* **40**, 1–12 (2018).

159. Calignano, F. *et al.* Overview on additive manufacturing technologies. *Proc. IEEE* **105**, 593–612 (2017).

160. Cheng, L. *et al.* Structure design, fabrication, properties of laminated ceramics: A review. *Int. J. Light. Mater. Manuf.* **1**, 126–141 (2018).

161. Chartier, T. *et al.* Additive manufacturing to produce complex 3D ceramic parts. *J. Ceram. Sci. Technol.* **6**, 95–104 (2015).

162. Gu, D. D., Meiners, W., Wissenbach, K. & Poprawe, R. Laser additive manufacturing of metallic components: Materials, processes and mechanisms. *Int. Mater. Rev.* **57**, 133–164 (2012).

163. Yang, L. & Miyanaji, H. Ceramic Additive Manufacturing : a Review of Current. *Solid Free. Fabr. 2017* 652–679 (2017).

164. Wang, J. C., Dommati, H. & Hsieh, S. J. Review of additive manufacturing methods for high-performance ceramic materials. *Int. J. Adv. Manuf. Technol.* 2627–2647 (2019) doi:10.1007/s00170-019-03669-3.

165. Adam, G. A. O. & Zimmer, D. On design for additive manufacturing: Evaluating geometrical limitations. *Rapid Prototyp. J.* **21**, 662–670 (2015).

166. Kruth, J. P., Leu, M. C. & Nakagawa, T. Progress in additive manufacturing and rapid prototyping. *CIRP Ann. - Manuf. Technol.* **47**, 525–540 (1998).

167. Travitzky, N. *et al.* Additive manufacturing of ceramic-based materials. *Adv. Eng. Mater.* **16**, 729–754 (2014).

168. Hagen, D., Kovar, D., Beaman, J. & Gammage, M. *Laser Flash Sintering for Additive Manufacturing of Ceramics*. *Devcom Army Research Laboratory* https://apps.dtic.mil/dtic/tr/fulltext/u2/1068687.pdf (2019).

169. Cheng, P. Y. & Khan, S. F. Dimensional accuracy and surface finish of investment casting parts by indirect additive manufacturing from fused filament fabrication. *IOP Conf. Ser. Mater. Sci. Eng.* **429**, (2018).

170. Mun, J., Yun, B. G., Ju, J. & Chang, B. M. Indirect additive manufacturing based casting of a periodic 3D cellular metal - Flow simulation of molten aluminum alloy. *J. Manuf. Process.* **17**, 28–40 (2015).

171. Van Hoorick, J. *et al.* Indirect additive manufacturing as an elegant tool for the production of self-supporting low density gelatin scaffolds. *J. Mater. Sci. Mater. Med.* **26**, (2015).

172. Meisel, N. A., Williams, C. B. & Druschitz, A. Lightweight metal cellular structures via indirect 3D printing and casting. *23rd Annu. Int. Solid Free. Fabr. Symp. - An Addit. Manuf. Conf. SFF 2012* 162–176 (2012).

173. Lithoz. https://www.lithoz.com/en.

174. Xie, H. *et al.* SiAlON–Al2O3 ceramics as potential biomaterials. *Ceram. Int.* **45**, 16809–16813 (2019).

175. Julien, B., Jean-Claude, G., Carine, A., Pierre, M. & Méryl, B. Euro PM2011 – Powder Injection Moulding: Feedstock Development Behaviours of Feedstock Including Not-Tailored Powder for Powder Injection Moulding.

176. Ewing, H. C. & Yang, S. The effect of precursor composition and sintering additives on the formation of β-sialon from Al, Si and Al2O3 powders. *Ceram. Int.* **37**, 1667–1673 (2011).

177. González-gutiérrez, J., Stringari, G. B. & Emri, I. Powder Injection Molding of Metal and Ceramic Parts. *Some C* (2012).

178. Edirisinghe, M. J. & Evans, J. R. G. Review: Fabrication of Engineering Ceramics by Injection Moulding. II techniques. *Int. J. High Technol. Ceram.* **2**, 249–278 (1986).

179. Huber, D. L. Controlling anisotropy in stereolithographically printed polymers. *J. Mater. Sci.* **54**, 2763–2765 (2019).

180. Shaffer, S., Yang, K., Vargas, J., Di Prima, M. A. & Voit, W. On reducing anisotropy in 3D printed polymers via ionizing radiation. *Polymer (Guildf).* **55**, 5969–5979 (2014).

181. Gadelmawla, E. S., Koura, M. M., Maksoud, T. M. A., Elewa, I. M. & Soliman, H. H. Roughness parameters. *J. Mater. Process. Technol.* **123**, 133–145 (2002).

182. Syalons, I. Syalon 21R Polytype Powders. vol. 44 2951010.

183. Oxazoline, E. Aquazol. **3**, 5–6.

184. Chao, R. Compensation for small losses to lacquer and inlaid decoration using paper fills painted and glazed in situ. *Stud. Conserv.* **61**, 149–154 (2016).

185. Ebert, B., Singer, B. & Grimaldi, N. Aquazol as a consolidant for matte paint on Vietnamese paintings. *J. Inst. Conserv.* **35**, 62–76 (2012).

186. France, I. Aquazol ® 5/50/200/500 Safety Data Sheet. 1–5 (2017).

187. Spillmann, A. L. B.-S.-R. Ring Shear Tester (RST-XS, Dietmar Schulze, Schüttgutmesstechnik). **16**, 2–3 (2011).

188. Schulze, D. Shear Testing of Powders for Process Optimization. *Annu. Trans. Nord. Rheol. Soc. Vol. 21, 2013* **21**, 99–106 (2013).

189. Donkova, B. & Petkova, V. Comparison of thermal behaviour of γ-MnC2 O4 .2H2 O in oxidative and inert media. *Bulg. Chem. Commun.* **47**, 185–189 (2015).

190. Ryszkowska, J. *et al.* Preparation and characterization of poly(urea-urethane) elastomers synthetized from rapeseed oil-based polyols. Part II. Thermal properties.

Polimery/Polymers **62**, 136–143 (2017).

191. Vinayan, B. P. *et al.* Performance study of magnesium-sulfur battery using a graphene based sulfur composite cathode electrode and a non-nucleophilic Mg electrolyte. *Nanoscale* **8**, 3296–3306 (2016).

192. Ozkan, N. Compaction and Sintering of Ceramic Powders. (1994).

193. Oleszko-Torbus, N. *et al.* Thermal and crystalline properties of poly(2-oxazoline)s. *Polym. Chem.* **11**, 15–33 (2019).

194. Bouten, P. J. M., Lava, K., Van Hest, J. C. M. & Hoogenboom, R. Thermal properties of methyl ester-containing poly(2-oxazoline)s. *Polymers (Basel).* **7**, 1998–2008 (2015).

195. Polymerchemistry innovations inc. Burnout residue analysis of Aquazol ceramic binder. 85714.

196. Li, Y. *et al.* Effect of Z values on the microstructure and mechanical properties of post-sintered reaction bonded β-SiAlON. *High Temp. Mater. Process.* **36**, 453–458 (2017).

197. Zerr, A. *et al.* Synthesis of cubic silicon nitride. *Nature* **400**, 340–342 (1999).

198. da Silva, C. R. M., de Melo, F. C. L. & de Macedo Silva, O. M. Mechanical properties of Sialon. *Mater. Sci. Eng. A* **209**, 175–179 (2002).

Appendix A: List of Figures

[******] https://www.syalons.com/
[†††††††] www.lithoz.com/en

---

‡‡‡‡‡‡ www.chemtube3d.com

[§§§§§§] https://www.syalons.com/

[*******] www.3dhubs.com

Appendix B: List of Tables

Appendix C: List of Symbols

L   Change in the length, m

L_o Original length, m

k_1 Constant

t   time, s

k_3 Constant

$\dfrac{dm}{dt}$ Rate of change of mass per time, gs^{-1}

D   Diffusion constant

$\dfrac{dc}{dx}$ Rate of change in concentration per distance, $molcc^{-3}m^{-1}$

A_o Area of cross section, m^2

Δw Change in weight, g

K_p Parabolic rate constant, m^2s^{-1}

R_a Average surface roughness, μm

ρ Relative density, gcc^{-1}

W_s Submerged weight in water, g

W_a Weight in air, g

D_g Green density, gcc^{-1}

D_s Sintered density, gcc^{-1}

M_g Green mass, g

M_s Sintered mass, g

FF_c Powder flowability index

σ_1 Consolidation stress, MPa

σ_2 Unconfined yield stress, MPa

i   Intensity, a.u.

σ_f Flexural strength, N

F   Force, N

b   width of the sample, m